DNA Mutation Detection via Fluorescence Imaging in a Spatial Thermal Gradient, Capillary Electrophoresis System

by

Bryan Lee Crane

B.S., Mechanical and Aerospace Engineering
University of Missouri-Columbia, 1999

Submitted to the Department of Mechanical Engineering
in Partial Fulfillment of the Requirements for the Degree of
Master of Science in Mechanical Engineering

at the

Massachusetts Institute of Technology

February 2001

Signature of Author.....
Department of Mechanical Engineering
January 30, 2001

Certified by.....
Ian W. Hunter
Hatsopoulos Professor of Mechanical Engineering
Thesis Supervisor

Accepted by.....
Ain A. Sonin
Chairman, Department Committee on Graduate Students

DNA Mutation Detection via Fluorescence Imaging in a Spatial Thermal Gradient, Capillary Electrophoresis System

by

Bryan Lee Crane

Submitted to the Department of Mechanical Engineering
on January 30, 2001 in Partial Fulfillment of the Requirements for the
Degree of Master of Science in Mechanical Engineering

Abstract

To improve the speed and efficiency of genetic screening, we are developing an instrument to detect mutations via a high throughput, automated system. Detection is based on changes in the melting temperature induced by single point mutations as in Denaturing Gradient Gel Electrophoresis (DGGE). This instrument measures the migrating position of test and wild type molecules in a spatial thermal gradient during capillary electrophoresis. In this thesis, the concept is described. A thorough design process is conducted focusing on controlling thermal expansion, creating a stable, predictable temperature gradient, and optimizing software and hardware. Finally, the concept is proved in a series of experiments successfully identifying the presence of a mutation in the test sample.

Thesis Supervisor: Ian W. Hunter

Title: Hatsopoulos Professor of Mechanical Engineering

Acknowledgements

When I was a junior in college, I told a friend of mine I didn't know why anyone would want to go to graduate school. A few years later, I moved to Boston to do just that. I had apprehensions about whether I'd like it or if I'd consider it a good experience in retrospect. Now at the end of my first graduate degree, I find that I have thoroughly enjoyed the experience. My time at MIT has been made rich by friends and colleagues that have inspired me, taught me, listened to my thoughts, and laughed with me.

Thanks to everyone in the Bio-Instrumentation Lab. Professor Ian Hunter, Dr. John Madden, Peter Madden, Patrick Anquetil, Dr. Tanya Kanigan, Dr. Colin Brenan, Keng Hui Lim, Dr. Sylvain Martel, Robert David, James Tangora, and Matt Graham, all helped me rapidly develop my understanding of biology, physics, engineering, electronics, and hockey. I look up to all of you and my aspirations to emulate your wisdom and insight have convinced me to pursue a Ph.D.

Thanks also to Dr. Xiao-Cheng Li-Sucholeiki and Dr. William Thilly of MIT, Dr. Zoran Sosic and Dr. Barry Karger from Northeastern University, and especially Dr. Leonard Lerman and Dr. Cathy Hogan of MIT for the hours they spent explaining to me the details of human genetics and its analysis.

I would also like to thank the many good friends I have made here. In addition to my friends in the Bio-Instrumentation Lab, Steve Buerger, Max Berniker, Matt Spenko, and Tom Scharfeld have all made my time here a lot of fun. Steve and I have faced many classes and beers together, and its been a pleasure to work along side him in these tasks. Max adds color to every occasion. I believe he's also responsible for my- now widely accepted- nickname, Beaner. Thanks to Tom and Matt for always being up for a good time.

Finally, thank you to my family who has always supported me even when it meant my moving far away. Among all my aspirations, my highest is the hope that someday I'll be as good a parent and grandparent as the ones I have.

Contents

Chapter 1 Introduction

In June of 2000, the public Human Genome Project and the private corporation, Celera Genomics jointly announced the completion of a rough draft of the sequence of bases which make up the human genome. This event was a major milestone, marking the beginning of what some expect to be tremendous advances in our understanding of human physiology, disease, and disease treatment. In this chapter, the promise of genetic analysis is reviewed in two broad categories: understanding disease and pharmacogenetics. A brief discussion will follow describing linkage disequilibrium (LD) studies, one of the strategies currently being employed to understand the information contained within the human genome. This will lead to the definition of instrumentation needs for this undertaking. In this thesis, a new instrument concept called spatial Thermal Gradient Capillary Electrophoresis (TGCE), intended to meet these needs, is described. The instrument's design and experimental proof of concept are presented demonstrating this method as a viable instrument for genetic research .

1.1 Understanding and Diagnosing Disease

During most of medical history, physicians and scientists have been restricted to the "top down" approach of understanding and diagnosing disease. Symptoms of a disease are observed. The symptoms are traced to a particular organ or region of tissue. Enzymatic or proteiomic deficiencies or other factors are determined to be causal to the disease. In some cases, these

deficiencies are then traced down to the genetic level and associated with mutations in the genetic code.

The Human Genome project, the expansion of our knowledge of molecular biology in general, and new instrument technologies, are enabling the "bottom up" approach to become more feasible. In this method, disease is correlated directly or semi-directly with genetic variations. Then the path back up the hierarchy can continue to understand how proteins and enzymes are affected by these variations and their affect on their expression as phenotypical characteristics of the disease.

The association of disease with genetic variation is an extremely powerful medical tool, even apart from any ability to cure the disease. Recognizing that a certain genetic pattern in an individual's genome signifies a predisposed high risk factor for a specific disease can allow physicians to advise individuals to take preventative lifestyle changes or medications. One potential example is lung cancer. If the results of a genetic screening showed an individual had weak resistance to lung cancer, he/she could be advised on the true risk of their smoking habit. The specific screening test given in this example does not yet exist but tests for several diseases are already available. These include tests for Cystic fibrosis, Huntington disease, Phenylketonuria, and others [39]. In the coming years, physicians and scientists hope to discover many more associations between genes and disease. The means by which these associations are discovered is discussed in Section 1.3.2.

In addition to its potential for early identification of high risk for a disease, the "bottom up" approach also holds potential for allowing us to better understand the mechanisms and progression of the disease. It will enrich our understanding of complex physiological interactions which induce the malfunction or reduce one's ability to resist the sickness. Such an

understanding is critical to eliminating or controlling the disease through surgical or drug treatment techniques.

This leads to one of the potentially most significant benefits of genetic association with disease. Developing causal relationships between disease, gene variants, and their functional expression can lead to targets that can be used by the pharmaceutical industry for drug development. Selection of target molecules that lead to the discovery of well-tolerated and effective medicine is a major problem for the pharmaceutical industry. To date, only a limited number of molecular target families have been identified, including receptors and enzymes, for which high-throughput drug screening is currently possible [39]. A good target is one against which many compounds can be screened rapidly to identify active molecules (hits). These hits can be developed into optimized molecules (leads), which are high efficacy, well-tolerated medicines.

1.2 Pharmacogenetics

Pharmacogenetics is the study of how genetic differences influence the variability in patients response to drugs and represents another major category of promise for the future of human medicine.

Through this study, we will be able to profile variations between individuals' DNA to predict responses to particular medications. Individual genetic profiling will provide information on the likelihood of efficacy and safety of a drug for a patient. A physician today has few methods of knowing how a patient will respond to a prescribed drug treatment. Many drugs work for only a small percentage of the afflicted population, as is reflected in Table 1-1 [8]. A physician has little choice but to prescribe possible drug treatments and evaluate their effectiveness. Not only is this trial and error method expensive, it exposes the patient to side

effects which come along with the drug. These could include discomfort or more adverse reactions. In fact, adverse drug reactions are in the top six leading causes of death in the US each year [8]. Classifying patients into subgroups based on their genetic profile will allow physicians and pharmaceutical companies to deliver the right drug to the right patient at the right time.

Table 1-1. Many drugs are ineffective for large numbers of people [8].

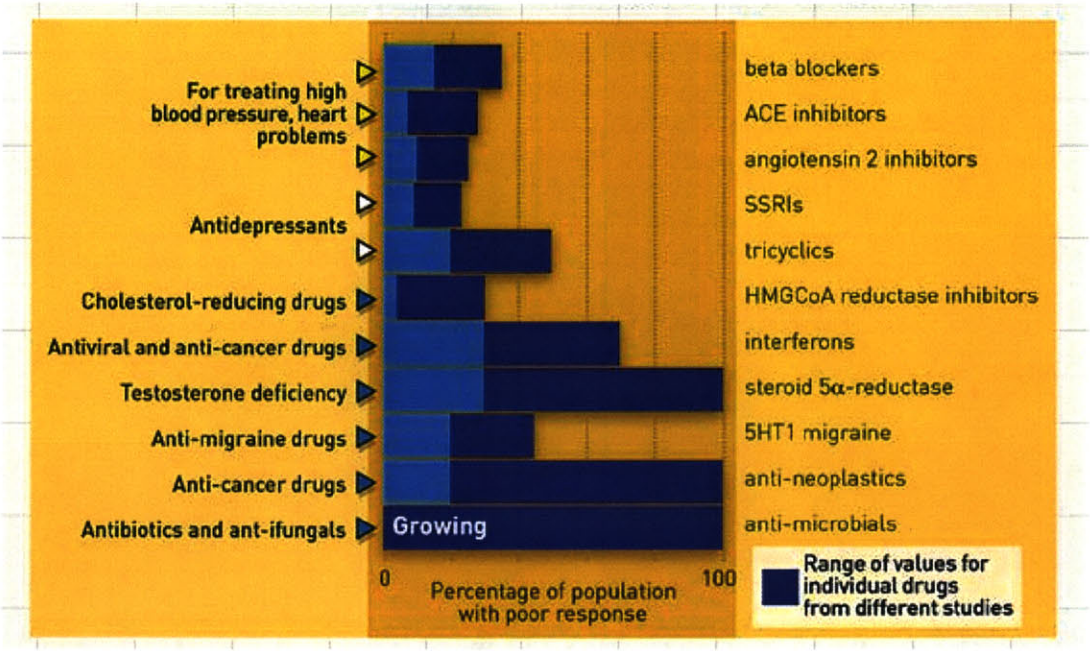

The ability to rapidly profile patients who are likely to benefit from a particular medicine will also streamline drug development and provide discrete medicines concurrently for different patients who have been segmented from the total disease population by their genetic profile. The drug approval process required by the Food and Drug Administration (FDA) commonly takes more than a decade and many millions of dollars. Leaders in the pharmaceutical industry hope that using genetic profiling will lead to the identification of subgroups that have high efficacy toward a drug in phase II clinical trials. Such classification could then be used in the selection of patient groups enriched for efficacy in phase III studies. This would likely make the approval process smaller, faster, and more efficient [39].

1.3 Association/Discovery Process

In the previous two sections, the terms genetic variations and profile have been used to described unique differences in individuals' DNA that would be indicative of a disease or drug response. In this section, more detail is given about how this variation is manifested and how the association of this variation with disease or drug response will be elucidated.

1.3.1 Single Nucleotide Polymorphisms and Point Mutations

The genetic code of any two individuals, though spanning more than 3.3×10^9 base pairs, is very similar. 99.9% of one person's DNA sequence is thought to be identical to any other human's. Only 0.1%, or 3 million bases, differentiate us from one another. It is believed that these 3 million base pairs describe our many phenotypical differences including things like height, hair color, and athletic ability, but also disease susceptibility and drug responsiveness.

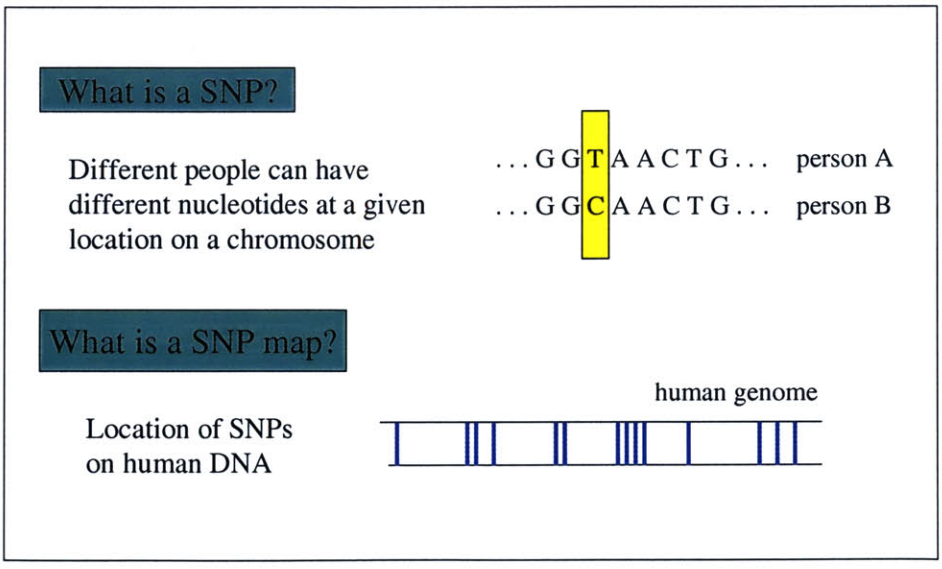

Figure 1-1. Understanding SNPs.

These unique base pairs are called point mutations and single nucleotide polymorphisms (SNPs). Specifically, a SNP is defined as single base pair positions in genomic DNA at which different sequence alternatives (alleles) exist wherein the least frequent allele has an abundance

of 1% or greater [5]. A single base pair mutation has a broader definition as it can occur at much lower frequencies in a population. For most diseases, it is believed that point mutations within a gene or set of genes are causal to the illness. However, because these mutations are at such a low frequency in the population, they are difficult to discover. Because a pattern of SNPs is often inherited with a single point mutation, and SNPs (see Section 1.3.2), because they occur at higher frequency, are easier to find, SNPs are often the items of interest in genetic profiling. A map which locates the position of SNPs on the human genome is currently being developed by multiple groups. On average, these SNPs occur once every 1000 base pairs. Among these groups are an extensive number of academic groups and such commercial entities as Celera Genomics and the SNP consortium, a group of 10 pharmaceutical companies, five academic institutes, and the Wellcome Trust. A list of the specific nucleotides (A, T, C, or G) present at these SNP locations (or at a subset of these locations) represents a genetic profile.

1.3.2 Linkage Disequilibrium Analysis

During meiosis, when the chromosomes of one parent are being recombined with the chromosomes of the other, there is a tendency, called linkage, for genes and surrounding DNA to be inherited together. The probability of linkage is measured by a percent recombination between loci.

Linkage disequilibrium describes a situation in which some combination of SNP alleles occur more frequently in a population than would otherwise be expected from random association. It implies that a group of markers has been inherited together. It can result from reduced recombination in the region or from a case in which there has been insufficient time to reach equilibrium since one of the markers was introduced into the population.

Therefore, variations of several ordered SNP markers that are close to, or within, a particular gene variant on a chromosome are likely to be inherited together with that gene variant when they are in linkage disequilibrium. In this way, a consecutive set of SNP variations that are in linkage disequilibrium with a disease phenotype can 'mark' the position on the chromosome where a susceptibility gene is located. These genes are known as susceptibility genes because they are good candidates to investigate for relevance to the disease since they have been implicated by an inherited pattern of SNPs. The same sort of pattern detection in linkage regions is being a applied to pharmacogenetic studies hoping to associate SNPs with drug responsiveness.

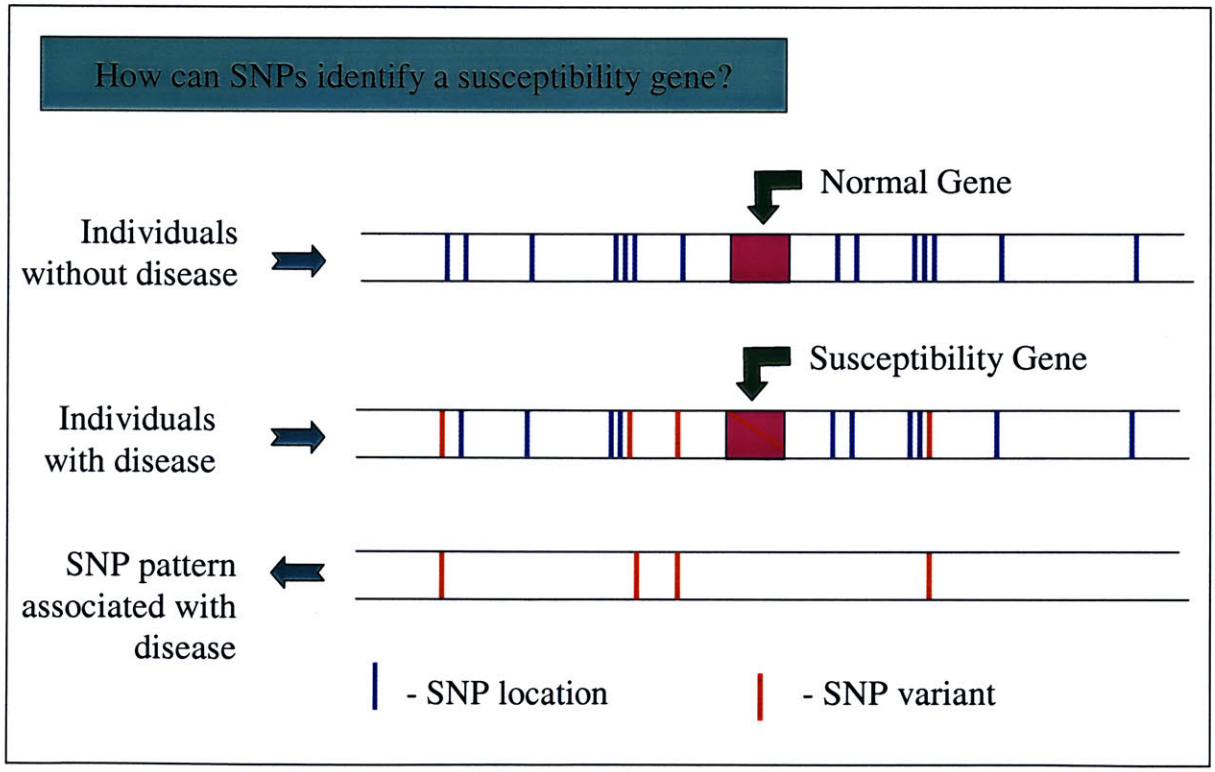

Figure 1-2. Identification of susceptibility genes by SNP disequilibrium analysis.

A simplified diagram of how SNPs can be associated with disease is given in Figure 1-2. As an example, suppose a scientist determined that an enzyme deficiency was responsible for a specific disease. From this knowledge, let us assume he was able to predict that the problem

must lie in any of twenty genes because of known relationships of the enzyme and proteins expressed by those genes. Further, suppose a map of SNP locations in linkage disequilibrium regions around each of the twenty genes was available or experimentally determined. Armed with such a map, the scientist could test each SNP location in each linkage region to determine if a variation from the most common allele was present for both the diseased group and the non-diseased group. After compiling a list of these, filtering the data of the diseased group against the control would show if a high correlation of a set of SNPs with the disease phenotype existed. If such a correlation existed, the scientist could conclude that a susceptibility gene lie in that linkage region. Such an analysis would be conducted for each of the linkage regions containing each of the genes in question. Note that further analysis would be required to certify which gene in that linkage region was correlated and how its expression contributed to the disease.

Preliminary success has been reported using this sort of analysis for Huntington's Disease and type 2 Diabetes mellitus [2,18]. However, for many common diseases with complex inheritance, identifying a target gene is a tremendous challenge. New instrument technologies are needed to increase the speed and decrease the cost of this process. In addition, new methods for association of disease with causal genes are also needed to improve the efficiency and effectiveness of genetic investigations.

1.4 Instrumentation Needs

Improved instrumentation is needed to increase the speed and reduce the cost of genetic analysis. To increase the speed, analysis times must be short and the segment length analyzed in each experiment should be long. To keep costs low, minimizing skilled labor requirements is of primary importance. In addition, it is also desirable to minimize the quantity of DNA and reagents needed. The technology should be amenable to parallel configuration and be

automatable for sensitive computer analysis. Finally, the technology should be able to detect any type of mutation, including insertions deletions, or substitutions reliably and reproducably.

1.5 Overview

Chapter 2 describes concepts involved in current, popular mutation screening methods. Chapter 3 describes the concept for the instrument and how the instrument meets the needs given above. Chapters, 4 and 5, discuss the design and development of the instrument including thermal expansion control and minimization, the design of the system used to establish the temperature gradient, and issues relevant to the design and integration of the optical, electrical, software, and mechanical systems. Chapter 6 describes the biochemical and electrophoresis aspects of the projecting including gels, sample injection, capillary coating, and fluorescent probes. Experimental results are presented in Chapter 7. Finally, Chapter 8 concludes the thesis and addresses areas of future work.

Chapter 2

Methods of Mutational Analysis

There are a plethora of methods available to detect mutated base pairs in a segment of DNA. In this chapter, four main categories of current techniques are briefly reviewed. These include those based on differences in electrophoretic mobility, hybridization techniques, cleavage methods, and sequencing. Whole books and many review articles have been written on these techniques so that an in-depth discussion is neither feasible nor worthwhile to include. Instead, the focus will be placed on describing the physical principle by which mutations are identified for each category. The most detail will be given to detection techniques based on electrophoretic mobility since this is the physical principle upon which Thermal Gradient Capillary Electrophoresis (TGCE) is based.

2.1 Differences in Electrophoretic Mobility

There are several methods which make use of the physical properties of DNA to identify mutations. These include Denaturing Gradient Gel Electrophoresis (DGGE), Single-Strand Conformational Polymorphism analysis (SSCP), Heteroduplex Analysis (HA), Constant Denaturing Capillary Electrophoresis (CDCE), and Thermal Gradient Gel Electrophoresis (TGGE).

Each of these analyses involves electrophoresing a wild type allele (control sample) and a potential mutant allele (test sample) through a polymerizing gel. DGGE and TGGE are generally done in slab gel format while CDCE is obviously intended to be carried out in capillary electrophoresis. The other methods are amenable to either format.

For any of these methods, the underlying principle is the same: mutations in the sequence can be exploited to cause a difference in the electrophoretic mobility as compared to the wild type sequence.

2.1.1 Identification via Melting Temperature Measurement

DGGE, TGGE, and CDCE utilize the difference in the characteristic melting temperature between wild type and mutant molecules to detect the presence of mutations. In these methods, double-stranded DNA is electrophoresed through a gradient of increasing concentration of denaturing agent (urea and/or formamide) or of increasing temperature. With increasing concentration of denaturant or temperature, the two strands of the duplex DNA begin to come apart. The section which melts first consists of a base sequence that gives it a lower melting point.[1] The melting temperature is mainly determined by the attraction of neighboring bases to each other by Van der Waals forces called 'stacking.' In this way, the melting characteristics of any DNA strand are sequence dependent.

In a long segment of DNA, several domains[1] with different melting temperatures may exist. To simplify melting dynamics to only two domains, most analyses based on T_m measurement are done using a so-called GC clamp. This is an oligonucleotide of 30 to 50 bases added onto one end of a duplex to create an artificial high-temperature melting domain. The remainder of the fragment becomes a low-temperature melting domain. Since the high melting

[1] a domain is a region of DNA over which base pair melting is strongly cooperative

domain is never melted, it is critical that any mutations of interest lie in the low melting domain. It is also desirable to observe a flat melting temperature profile for the low melting domain, such that all base pairs melt in a very narrow temperature range. Such a transition makes melting easier to resolve in the data analysis.

When analyzing point mutations, theoretical melting simulation can be used to determine the optimal stretch of DNA to isolate from the genome as well as optimal fragment end on which to place the GC clamp to create a flat melting profile across the entire region local to the mutation of interest.

As the DNA migrates into the region of characteristic temperature or denaturant concentration, the dissociation of the low melting domain creates increased drag (resistance against electrophoretic motion), dramatically reducing its migration velocity. This change in velocity occurs at different locations along the gradient for strands of the same length but differing by a single base pair. After the wild type and mutant alleles have been electrophoresed for a duration of time, they become spatially separated in the gel because of their unique velocity profiles [1,10].

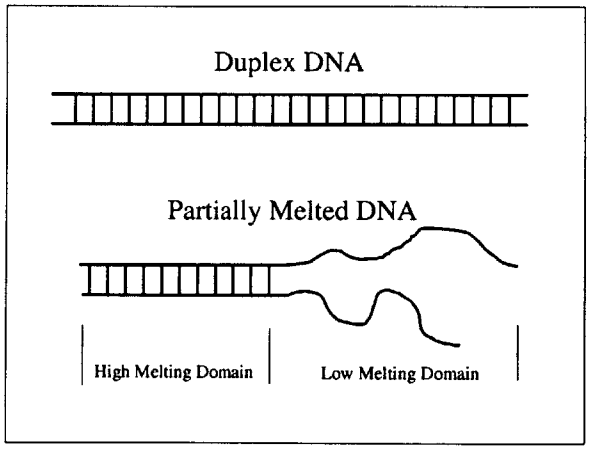

Figure 2-1. Illustration of melting of DNA.

The concept of heteroduplexes and homoduplexes is important in understanding these methods. The term homoduplex refers to a DNA strand in which all base pairs in that strand are paired according to the rules of complimentarity, i.e. T is paired with A, G is paired with C. This could represent a wild type sequence or a mutated sequence. These homoduplexes are represented in Figure 2-2.

Heteroduplexes can be formed when both homoduplex wild type and homoduplex mutant molecules are completely denatured and are then allowed to re-anneal. This process simply requires these quantities to be heated together to approximately 95 °C to separate the strands and then brought to 50 °C to re-anneal. During the re-annealing, a 5'-3' single stranded DNA molecule from one sequence will pair with a 3'-5' single stranded molecule from either original sequence. The end result now includes four different molecules. These will include the homoduplexes shown in Figure 2-2 and the heteroduplexes shown in Figure 2-3.

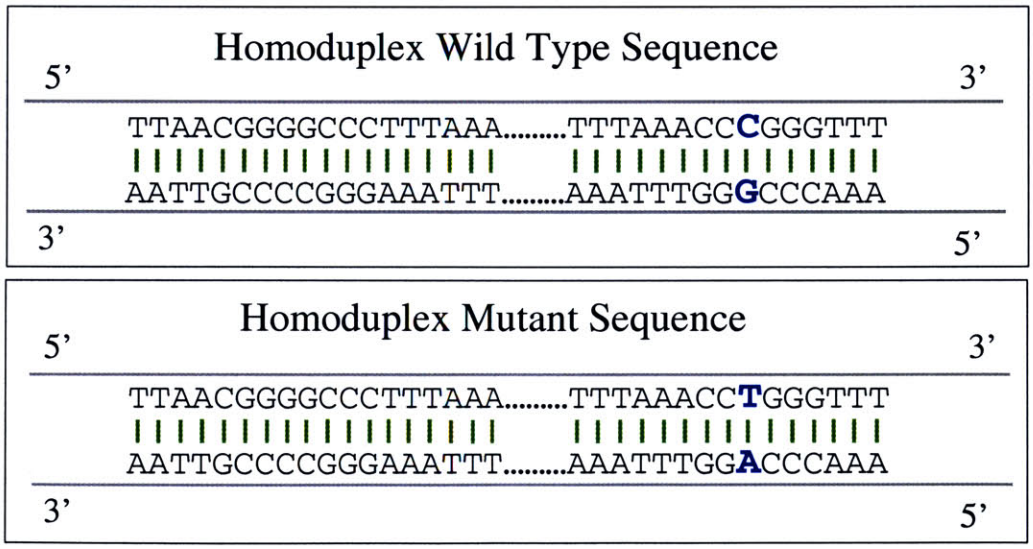

Figure 2-2. The two types of homoduplexes.

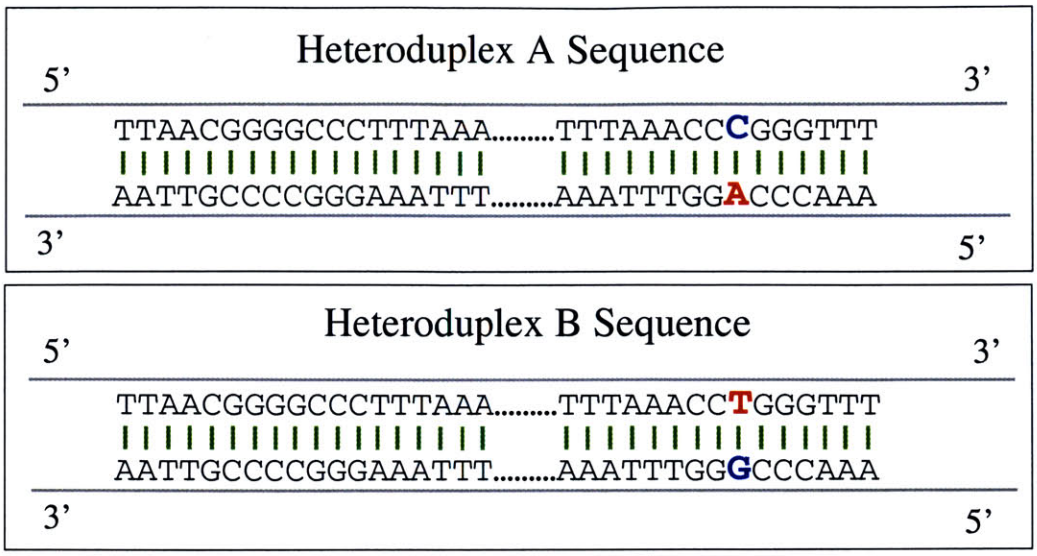

Figure 2-3. Heteroduplexes formed by combination of homoduplex strands.

The heteroduplex formed from the recombination of a wild type and a mutant strand contains a base pair which does not obey the rules of complimentarity. This results in a bulge in the molecular structure as these mismatched molecules exhibit a different structural bonding than other complimentary pairs. The creation of a heteroduplex allele for an analysis based on electrophoretic mobility is important because the change in melting temperature associated with this mismatch is much larger than the original difference between the wild type and mutant homoduplexes.

A typical mutation in which an A-T is replaced by a C-G in a strand approximately 400 base pairs in length, would yield an decrease in the T_m on the order of 0.1 °C from wild type to mutant homoduplex strands. However, the ΔT_m between either heteroduplex and the wild type would be greater than 1 °C thus making the measurement 10x more sensitive. The values given in the above example are based on theoretical and (unpublished) experimental results generated in the Lerman Lab at MIT [26,27].

Theoretical estimations of the melting temperature are very useful to circumvent the time consuming empirical analysis needed to tune the gradient to the appropriate beginning and ending denaturant concentrations (DGGE) or temperatures (TGGE). The melting theory of Poland-Fixman and Fixman-Freire defines the T_m as the temperature at which duplex and random coil states have equal probability. Its uses this statistical-mechanical description to model the effects of base pair stacking and ionic bond strength across base pairs to predict the T_m for a given sequence of DNA [26].

2.1.2 Identification via Molecular Structure Deformation

HA and SSCP make use of the distorted structure that is created in a DNA molecule which contains a base pair mismatch. In HA, the bulge in the molecular structure around the mismatch causes the mutated molecules to experience a larger drag than the pure structure of the wild type during electrophoretic migration. Thus after electrophoresing the wild type and mutated molecules for a duration, two distinct bands are formed as the alleles become spatially separated.

As the name implies, SSCP is based on analysis of single stranded DNA. When single stranded DNA is placed in a non-denaturing solution, it will fold on to itself in a sequence specific manner. If one of the bases is changed, the molecule is likely to fold into a different shape. The different shapes create unique drag forces resisting electrophoretic migration providing the means to spatially separated mutant from wild type in the gel.

2.2 Hybridization Techniques

Hybridization techniques are best suited to diagnostic testing for frequently occurring mutations since they require an oligonucleotide spanning the presumptive site of the mutation. To screen for those specific, known mutations rapidly, techniques in this category are often used.

Hybridization techniques attempt to detect complimentary base pairing of a known oligonucleotide sequence with a test fragment. Many variations of this approach exist. Two of these variations include DNA microarrays and molecular beacon analysis.

DNA microarrays consist of sequence defined oligonucleotide (15-20 mer) probes immobilized on a chip in a grid pattern. The probe sequences can describe an entire gene or several genes including wild type and common point mutation variants. Grids can have as many as 10^7 probes/m^2 [15]. Fluorescent tagged, PCR amplified products (test fragments) are washed across the chips. When hybridization to the complimentary sequence occurs, the fluorophore "lights up." The resulting signal is then compared to the wild type profile to determine if mutations are present.

Analysis using molecular beacons differs from DNA arrays in a number of ways. Molecular beacons do not need to be immobilized on a solid surface. Additionally, only the probes need fluorescent tags as opposed to tagging all the PCR product. In this method, probes are single-stranded nucleic acid molecules that possess a stem-and-loop structure as shown in Figure 2-4. The loop portion of the molecule is a sequence that is complementary to a predetermined sequence in a target DNA fragment. Attached to one arm portion of the probe is a fluorescent molecule. Attached to the other arm is a quenching molecule. The stem keeps the two molecules close to each other, causing fluorescence of the fluorophore to be quenched by fluorescence resonance energy transfer. As a result, the fluorophore is unable to fluoresce. When the test fragment encounters the probe, it forms a structure that is longer and more stable

than the loop stem structure. In this way, the probe undergoes a spontaneous conformational change that forces the arms apart, causing the fluorophore and quencher to move away from each other signaling the success of hybridization. Test fragments which do not hybridize cause no background fluorescence since the probe fluorophore remains quenched [47].

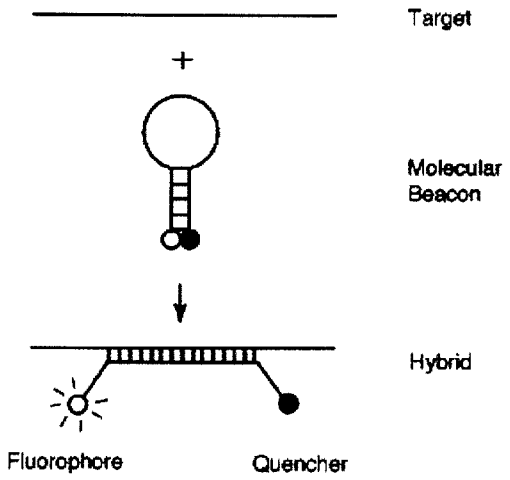

Figure 2-4. Molecular beacon diagram [47].

2.3 Cleavage of Heteroduplexes

Two notable methods in this category include chemical cleavage of mismatch (CCM) and enzyme mismatch cleavage (EMC).

In CCM, hydroxylamine (H) and osmium tetroxide (OT) are mixed with the heteroduplex test fragments. H reacts with mismatched C bases. OT reacts with mismatched T bases. Peperdine cleaves the modified base, and the resultant products electrophoretically are separated by size to determine the location of mismatched bases [38].

EMC uses bacteriophage resolvases to cleave the site of mismatch instead of the chemical method used in CCM. These enzymes specifically bind and cleave the mismatched

region however the method detects deletions more efficiently than point mutations. The location of mismatches are then resolved via electrophoresis as in CCM [15].

2.4 DNA Sequencing

Detecting mutations by sequencing alone can be difficult. Automated sequencing instruments have difficulty recognizing point mutations, especially mutations at low frequency, since they are easily masked by unmutated fragments in the sample. Future improvement in the base calling software may aid in the usefulness of sequencing for effective mutational scanning.

The importance of sequencing to mutation detection is not to be underestimated, however. Many of the methods discussed above are only able to indicate that a point mutation exists in a fragment. Identifying the type and location of a mutation is conducted via sequencing in additional steps.

Chapter 3 Instrument Concept

DGGE is the method of choice for mutation detection for many labs because it has been shown to have high sensitivity (~99-100%), i.e. done correctly, the results will include no false positives or false negatives. [10] It is also amenable to computer simulation for optimization of experimental parameters and allows easy isolation of the mutant allele for its subsequent sequence determination. Further, it is capable of analyzing segments several hundred base pairs in length. However, this technique is difficult, requires skilled labor, long preparation and experiment times (in some cases, more than 16 hours), and large reagent and DNA quantities. [29]

3.1 The New Approach

In this work, a new approach is developed which utilizes the same basic principle as DGGE and has the same advantages but is resolved in a spatial thermal gradient in capillary electrophoresis. The new approach is much faster, requires less skilled labor, and uses very small quantities of DNA and reagents. The capillary format also allows computer automation and scale up through parallel analysis using multiple capillaries. The concept is abbreviated TGCE (Thermal Gradient Capillary Electrophoresis).

In TGCE, a spatial thermal gradient is established along the length of the capillary. This takes the place of the linear gradient of chemical denaturant used in DGGE. The temperature gradient is created by mounting the capillary in a thermally conductive plate. The thermal gradient is easily established in the plate by controlling the end temperatures and allowing heat transfer along the plate to create the temperature distribution. In this work, a copper gradient plate is developed, the end temperatures of which are controlled by Peltier-effect thermoelectric devices. Thermal conduction along the plate creates a highly linear temperature distribution along the imbedded capillary. This system is discussed in detail in Chapter 4.

A temperature at a specific position along the capillary can be inferred by interpolation across data points measured at intervals along the plate. In this work, a heat transfer model of the system aids interpolation between thermocouple measurements.

3.2 Detecting the Onset of Melting

As in DGGE, differences in the melting temperature are measured to test for the presence of mutations. Since position is correlated with temperature in TGCE, this technique essentially measures the position at which melting occurs. Two methods of recognizing the onset of melting are possible. The first method is to measure velocity to detect the distinct change in mobility that occurs upon melting. The second possible method is to measure the fluorescent intensity of an intercalating dye which undergoes a significant fluorescence reduction upon the transition from binding to the double stranded structure to the single stranded, partially melted structure. These techniques are described in Figure 3-1.

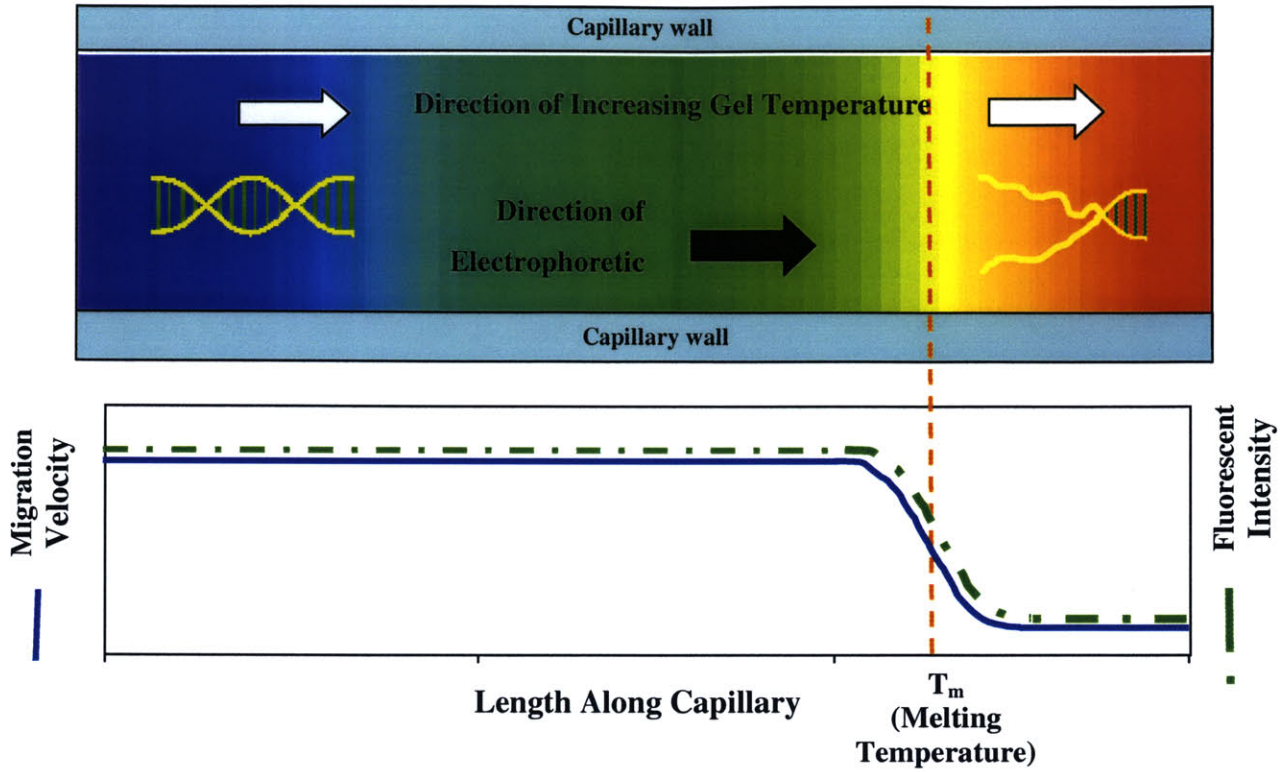

Figure 3-1. Measuring melting in TGCE.

The first method detects the onset of melting by the distinct change in migration velocity that occurs when the DNA undergoes the change from duplex to single-stranded structure. The technique can be implemented by continuously measuring the position of the migrating DNA. In this application, the position of the DNA is imaged via laser induced fluorescence (LIF) of a 5-carboxyfluorescein (FAM) end-labeling probe. The capillary is scanned back and forth in front of an optical detector to record the position of the DNA along the capillary length. The rate of change of DNA position versus time (migration velocity) is constant until melting occurs. Upon melting at their characteristic T_m (which correspond to characteristic positions along the capillary), wild type and mutant alleles exhibit a lower migration velocity. By monitoring position and time continuously, a correlation between velocity and position of each allele is possible. A test sequence whose migration velocity profile differs from the simultaneously

determined wild type velocity profile is known to contain a mutation. The means by which these measurements are made is described in Chapter 5.

The first method scans the capillary in front of the detector to measure position as a function of time. Keeping all systems stationary and simply monitoring a point near the end of the capillary could also be used. In this case, a mutation would be detected by the spatial separation that develops from the increment of time over which the mutant and wild type strands were traveling at different velocities. For this work, the former method was chosen for two reasons. First, a measurement of the velocity profile is more information rich. Besides knowing that a mutation exists in a given test strand, a velocity profile difference can be used to infer the difference in T_m between the mutant and wild type sequences. The other reason to scan the capillary was because it was required for the second method of detecting the onset of melting.

The second method of detecting the onset of melting is to measure the fluorescent intensity of an intercalating dye. In this work, the intercalator, YO-PRO-1, was selected. This probe has a large fluorescent enhancement upon binding to double stranded DNA. Therefore, when the DNA undergoes the transition from the double stranded to random coil structure, a sharp drop in the fluorescent intensity of the intercalator could be measured.

The use of the dual measurement method was eventually discarded for reasons that are discussed in detail in Chapter 6. In the final implementation, only the change in mobility was used to indicated the position at which melting occurred.

3.3 Variable Sensitivity to Achieve Desired Resolution

For any instrument, the resolution and sensitivity are critical performance factors. This instrument seeks to resolve single point mutations of any form including insertions, deletions, or substitutions. As discussed in Chapter 2, the minimum expected temperature differential

between mutant and wild type homoduplexes is 0.1 °C. While heteroduplex analysis can amplify this difference, this ΔT_m serves as a lower boundary on required resolution. This criteria dictates that the TGCE instrument must be able to spatially resolve distinct peaks which have melted at positions with temperatures differing by 0.1 °C.

The instruments ability to do this is highly dependent on its sensitivity. Here we defined sensitivity to be the change in temperature per unit distance along the capillary. By tuning the end point temperatures that control the thermal gradient, the ability to spatial resolve peaks with a small ΔT_m can be adjusted and optimized.

The instrument's ability to resolve distinct peaks is also a function of the peak sharpness. Many factors contribute to properly conducting electrophoresis such that all like DNA molecules migrate together in a tight band. These are discussed in detail in Chapters 5 and 6.

Chapter 4
Design of Thermal Gradient System

The gradient plate and associated fixturing hold the capillary in the optical path while establishing a thermal gradient along the length of the tube. In addition, the thermal gradient system must provide the means to interface the electrophoresis buffer solutions and injections solutions with the capillary.

This section includes an analysis of the first gradient plate design to identify areas for improvement. From this analysis, goals for a new design are defined. Conceptual solutions are then discussed. A final design for the gradient system is presented with relative theoretical analysis to select materials, define geometries, and show that it meets design criteria.

4.1 Analysis of Initial Gradient Plate Design

Figure 4-1, below, shows the original gradient plate used in TGCE experiments. Full details of its design can be found elsewhere [3]. Briefly, the gradient plate was a 250 mm × 50 mm × 3.2 mm 6061-T6 aluminum plate. It contained two 393 μm grooves. The groove at the center of the plate retained the capillary. Thermocouples were imbedded in the upper groove. These thermocouples were mounted in an acrylic fixture which bolted to the front face of the gradient plate (not shown). Nylon screws extended through the gradient plate and nylon spacers were used to mount the plate to a vertical linear stage. A 550 mm long capillary was housed in

the plate, the ends of which were directed into buffer vials. On each end of the plate, an 80 W joule heater was mounted. These heaters could be used to elevate the two ends to specified temperatures. Conduction, convection, and radiative heat transfer along the plate created the thermal gradient down the capillary.

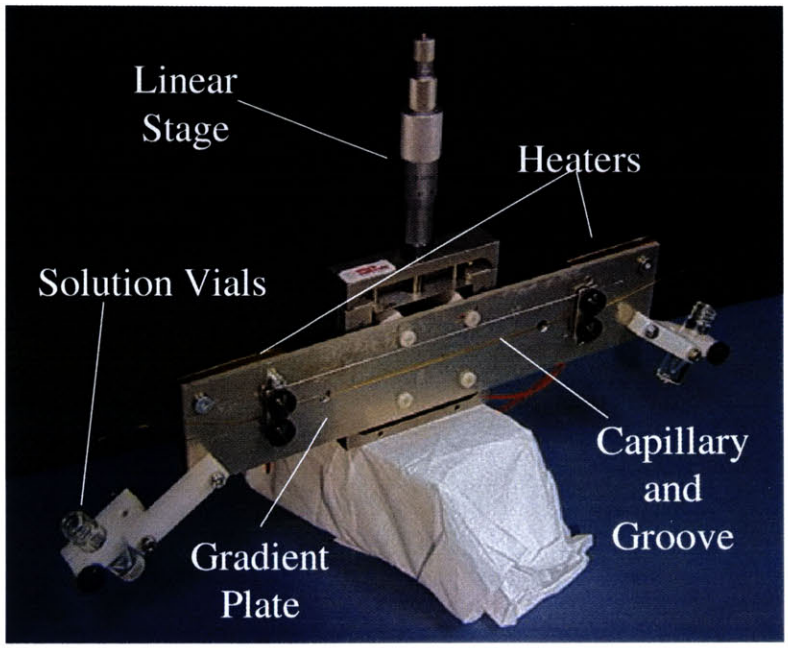

Figure 4-1. First gradient plate design [14].

Several problems became evident when this design was implemented. The first was the negative impact of non-uniform thermal expansion on optical alignment. When the thermal gradient was activated, the various materials coupled to the gradient plate expanded different amounts due to their unique thermal expansion coefficients. The thermal expansion coefficient of acrylic used in mounting the thermocouples (72.9 μm/m/K) is more than three times that of the aluminum (23.6 μm/m/K) [4]. In addition, since the linear stage was thermally isolated from the aluminum plate, its expansion relative to the gradient plate expansion was very small. The result was an arcing deformation of the gradient plate viewed from the top (Figure 4-2).

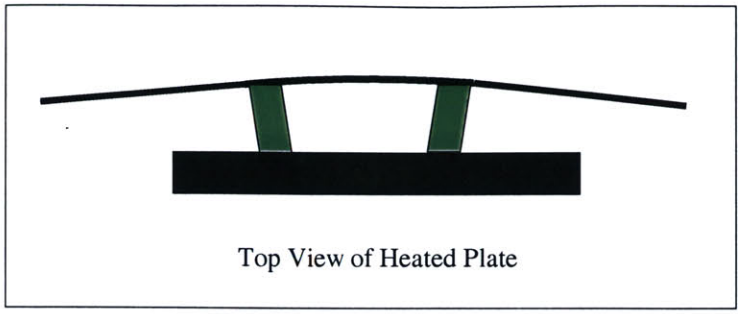

Figure 4-2. Deformation due to thermal expansion.

While the deformation is not detectable via visual inspection, its affects are observable in data collected by Graham [14]. The TGCE results in his thesis show an increased background signal at the center of the plate (in plane of optical focus) with diminishing background toward the ends of the plates (deformed out of optical focus). Based on the pinhole size used in the optical system and the resulting confocal volume, it can be estimated that the regions near the ends of the scannable region were distorted out of plane ~100 μm.

There were other optical alignment problems in addition to those related to thermal expansion. Optical alignment was originally done in a two step process. The first step included adjustments based on laser reflection from the capillary/gradient plate surfaces on to a piece of paper in the light path. This was a difficult process which required patience and practice. Later, a linear indicator was added (10 μm resolution) to aid in this step. While this improved the process, it did not eliminate the second step. Fine adjustment was conducted by maximizing the reflected intensity measured at the photosensor module. It was difficult to know for sure that the confocal volume was truly centered in the capillary when reflected intensity was maximized. This was one of the possible causes of the many TGCE experiments that showed no signal [13].

A third optical alignment problem arose based on the imaging window in the capillary. When the capillary was being prepared for an experiment, the polyamide coating was burned off a ~100 mm long region to create a window over which the DNA could be imaged. The

polyamide coating on the rest of capillary remained. This coating was needed in order for the capillary to bend into the vials at the ends of the gradient plate without breaking. A consequence of leaving the coating on the non-imaged part of the capillary was that the groove that housed the capillary had to be wider. The capillary itself had an outer diameter of 321 ±4 μm. The polyamide coating on the capillary enlarged the outer diameter to 363 ±12 μm. The width of the groove in the gradient plate was measured to be 395 μm. Therefore, in the region of the groove that held the capillary with coating removed, there was room for deviation of ±37 μm from the center of the groove. This groove and capillary are shown in Figure 4-3. Chapter 5 discusses pin hole radius optimization and shows that tolerances of this magnitude were problematic.

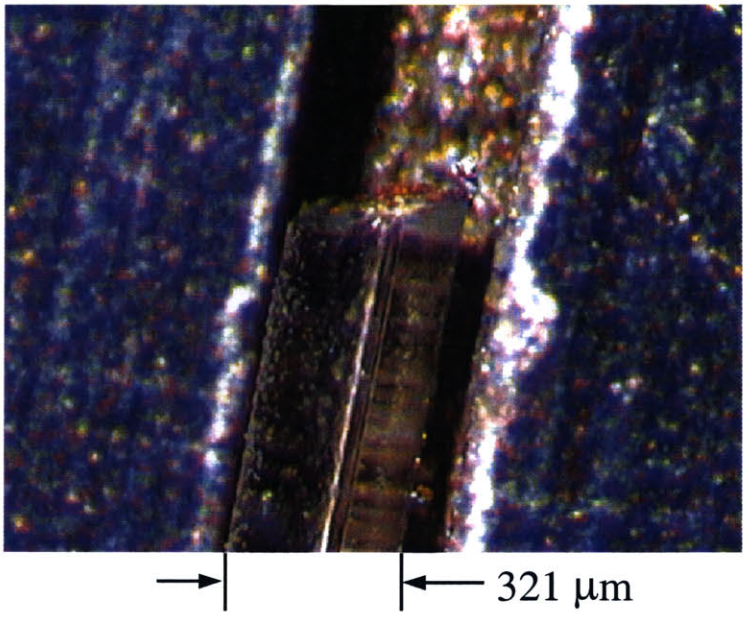

Figure 4-3. Close up of capillary with coating removed in initial gradient plate groove.

Another issue with this design was temperature measurement along the length of the gradient. As stated briefly before, the thermal gradient was established via two heaters. In experiments by Graham, the "high side" heater was typically at a temperature of 92 °C while the "low side" heater was typically at 65 °C [14]. Thermal energy traveled from the "high side" to

the "low side" along the plate via conduction. As the temperature was increased above ambient, thermal energy was dissipated along the plate via convection and radiation. The design intent was to measure the temperature only at two end points, and then use an accurate model to interpolate temperatures between the two measured values.

This approach was problematic for a two reasons. First, convective and radiative heat losses are highly dependent on variable environmental conditions. The room temperature and internal air currents were not tightly controlled. This inhibited the effectiveness of the system model. It also meant that during the experiment the temperature distribution could vary with time. Second, the geometry of the gradient plate included several parallel heat paths ignored in the model, further complicating the difference between the idealized and actual systems. These parallel heat paths included the thermocouple mounting block, the capillary mounting tabs, and to a lesser extent, the fixture mount.

A fifth problem with the gradient plate design involved the fluidic system including the capillary and the solution vials. In the initial version, the capillary was bent after exiting the gradient plate and then inserted into the buffer vials. To ensure that the capillary was not damaged, a generous bend radius was allotted in the design. The end result required a capillary tube 550 mm in length to extend from one buffer vial to the other. As discussed previously, only 100 mm of this distance was actually imaged during the experiments. The large dead space, the distance from the open end to the imaging window, resulted in wasted time during the experiment since the DNA must migrate through the dead space before any useful data can be collected.

4.2 Resultant Criteria for New Design

Based on the analysis of the first gradient plate design, a series of criteria were developed to guide the new design. These criteria are shown in item numbers 1 to 5. Items 6 to 8 include additional general requirements the new design must also meet. Additional comments about items 1 to 4 are included below.

Table 4-1. Criteria for new design.

1.	Minimize distortion effects of thermal expansion
2.	Create stable thermal gradient by minimizing radiative and convective heat loss along plate
3.	Minimize tolerances associated with vertical positioning of capillary
4.	Integrate improved optical alignment method
5.	Minimize capillary length
6.	Integration of all system components
7.	Allow for easy change of solution vials
8.	Be robust and stiff to vibrational disturbances and or accidental impact by instrument operator

The first criteria is to create a design which has predictable, controlled thermal expansion which will have minimal impact on optical alignment. Expansion of the gradient plate is generally permissible as long as it does not result in the plate deflecting out of plane.

Design criteria two was to create a stable temperature distribution in the gradient plate. To make the interpolated temperature measurement more robust and accurate, convection and radiative heat losses along the capillary length should be minimized. The new design should create a linear thermal gradient by limiting heat transfer to conduction from the "high side" to the "low side" temperatures.

Minimizing tolerances associated with vertical positioning of the capillary is another important design goal. The oversized groove width is one example of such tolerances. The build-up of these tolerances from all sources in the system defines the size of the confocal volume that must be used in the design. In order to achieve good spatial resolution it is desirable to have a minimal confocal volume.

4.3 Conceptual Solutions

Design criteria 1 and 2 basically require a fundamental change in the initial design concept. New design concepts were developed to meet these criteria.

In the case of design criteria 2, the obvious solution is to insulate the gradient plate as shown in Figure 4-4. By proper selection of the cross-sectional area, thermal conductivity of both the plate and the insulation layer, a more linear thermal gradient can be established which is minimally effected by the convection and conduction.

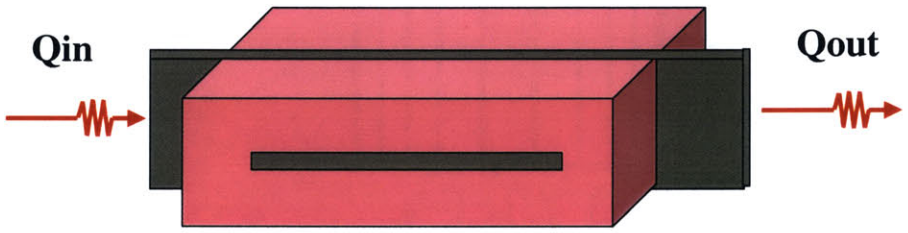

Figure 4-4. Insulation to reduce effect of convection and radiation.

Methods of achieving design criteria 1 were more challenging. The real problem was how to mount a plate that was non-symmetrically thermally expanding in such a way that it did not deform out of a flat plane. In addition, avoiding parallel heat transfer paths was important. Finally, thermal distortion of the fixture itself also had to be minimized. Many alternatives were considered.

One option was to mount the gradient plate to a very high-stiffness fixture which prohibited any thermal expansion. Instead, internal stresses would be developed in the plate. This option would require a bulky fixture which likely would also make design restrictions on the gradient plate itself.

Another option was to design a fixture which acted as a flexure. One of these concepts is shown in Figure 4-5. It features a fixture whose arms deflect symmetrically thus keeping the capillary in optical alignment. This design was eventually discarded in favor of the cantilever design. Concerns existed regarding the flexure's manufacturability to tight tolerances and to complications related to optimizing the fixture geometry to ensure symmetric distortion under the non-symmetric heating.

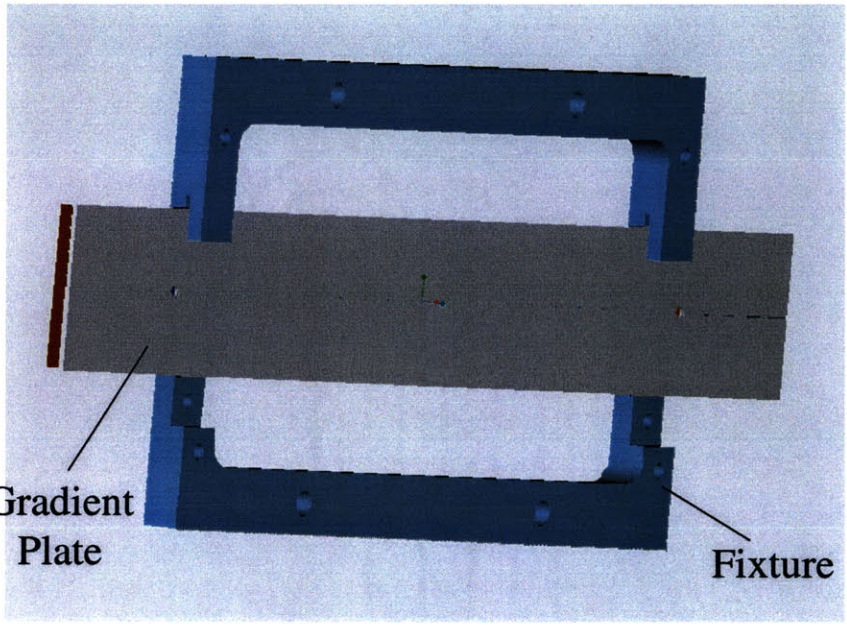

Figure 4-5. Flexure design concept.

The cantilever design is shown in Figure 4-6. In this concept, the gradient plate is mounted at the cold side end by four bolts into the fixture. Thermal expansion in the cantilevered portion should occur uniformly such that it will not affect optical alignment. This

solution seemed simple to engineer and easily analyzed to insure that it produced the predicted results.

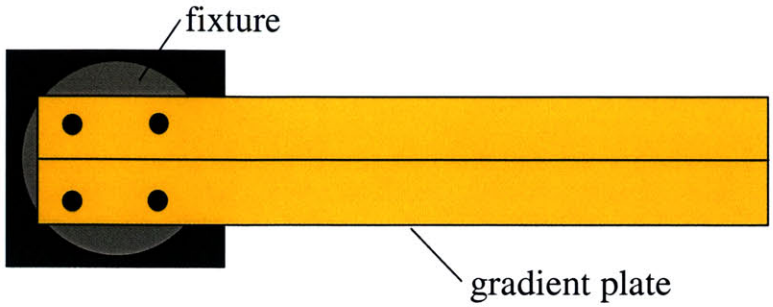

Figure 4-6. Cantilever design concept.

4.4 Final Design for New Gradient Plate

A more detailed representation of the final gradient plate concept is shown in Figure 4-7. There are several key features of this design. Each of these features is now reviewed with a brief discussion regarding the design criteria each satisfies.

First, as just discussed, this design makes use of a cantilevered gradient plate. The cantilever support makes thermal expansion simpler to predict than in other mounting methods. Thermal expansion in the constrained end is minimized by selecting that end as the "low side" temperature, i.e. the location of the heat sink. This satisfies design criteria 1.

Another important feature in this concept is the greatly reduced capillary length which was design criteria 5. In the final implementation, capillaries were 275 mm in length, half the length required by the original gradient plate design. This was achieved by the use of 0.5 mL PCR tubes to retain the buffer solutions. Capillary forces in these small vials are high enough that they can be oriented horizontally without worry of spilling fluid. In fact, these tubes can be oriented upside down and no fluid will be spilled. With the PCR tubes in a horizontal

orientation, the capillary no longer needs to bend through any radius, thus the capillary can be shortened significantly. Plastic clothes clips were integrated into the design to retain the solution vials. This simple but effective solution meets the requirements of design criteria 7.

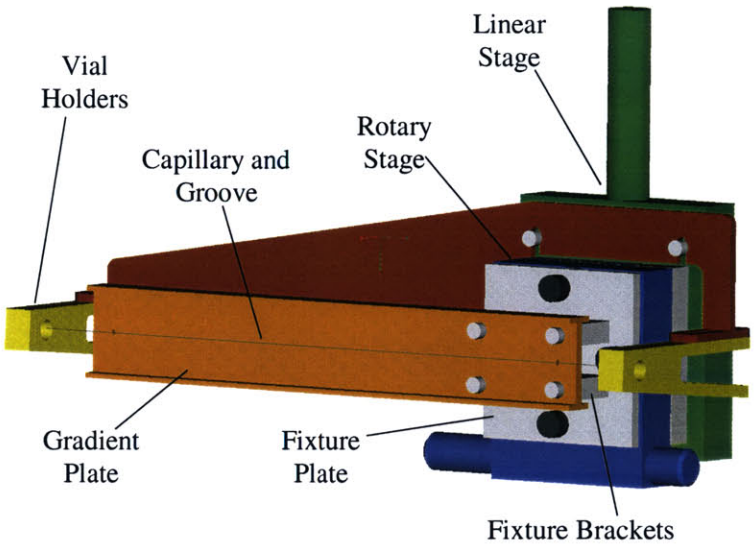

Figure 4-7. Final design concept for new gradient plate.

The insulating material, not shown in Figure 4-7, is another important feature of this design. The concept calls for an insulating layer to cover the heat source end of the gradient plate all the way down to the fixture. This feature provides a solution for criteria 2.

Optical alignment holes were integrated into the gradient plate to attempt to meet the requirements of design criteria 4. In the final application, however, it was found that these alignment holes could not provide information precise enough to tightly align the system. To get very good alignment, a second capillary replaced the gel-filled capillary. The replacement capillary contained a 100 mM concentration of fluorescein fluorescent dye. The alignment procedure then involved adjusting the capillary's rotational and linear orientation until a maximum, constant signal was read over the length of the capillary.

The gradient plate's length was defined by a number of factors. First, the linear stage used to scan the gradient plate in front of the optical detector has a travel range of 150 mm. In this width, both the imaged portion of the capillary and the optical alignment holes (discussed previously in Section 4.2) had to be placed. In the final concept, the optical alignment holes were located at the extremes of this span. This minimized the impact on the heat transfer pattern across the imaged capillary width. Heat source and sink sizes and fixture size requirements defined additional requirements on gradient plate length. Implementing the design in a way that considers how each component must interface with the others is the requirement of design criteria 6.

The gradient plate design features an I-shaped cross section. This geometry is depicted in Figure 4-8. The cantilever design makes the gradient plate particularly susceptible to vibrations induced during scanning. To reduce this potential, extra stiffness was included in the design by introducing the I-beam cross section meeting the requirements of design criteria 8. It will be shown that this geometry also gives large margins of safety in avoiding buckling of the constrained region of the gradient plate. This is required in design criteria 1.

Finally, design criteria 3, controlling vertical tolerances, was addressed during selection and manufacturing of the new components for the design. In addition, optical system design, shown in Chapter 5, ensures that the tolerances that do exist do not place the capillary outside the confocal volume.

4.5 Analysis to Refine Design

With concepts firmly established, the next phase of the design was to define materials and geometries and show that their combination achieved the desired results. This requires discussion of suitable materials for the gradient plate and insulation layer, heat transfer analysis

to establish appropriate geometries such that conduction dominates heat transfer, and analysis of the mechanics of materials to show that permanent deformation and yielding do not occur.

4.5.1 Material Selection

Of primary importance in the selection of the gradient plate material were high thermal conductivity and low thermal expansion. In order to establish a highly linear gradient, it was critical that the magnitude of heat transferred from any volume along the plate be dominated by conduction as opposed to convection or radiation. To accomplish this, high thermal conductivity was needed. Minimizing thermal expansion would ease problems of creating predictability and controllability.

Diamond, with a thermal conductivity of 990 W/m/K and a thermal expansion coefficient of 1.18 μm/m/K [4], had an excellent combination of these properties, but its high cost and low manufacturability made it unattractive.

6061-T6 aluminum, used in the first design, has a thermal conductivity of 167 W/m/K and a thermal expansion coefficient of 26.6 μm/m/K [4]. While the thermal conductivity is better than steel alloys, there were several materials with higher conductivities and lower expansion coefficients.

One notable option was mono-crystalline silicon. Wafers up to 200 mm in diameter and 2-3 mm thick are readily available. Machining the wafers could have been accomplished with in-house Electrical Discharge Machining (EDM) technology, and the primary material properties of interest were among the best found. The thermal conductivity of mono-crystalline silicon is 163 W/m/K, comparable to that of aluminum, but the thermal expansion coefficient is only 2.5 μm/m/K. In the end, this material was not chosen because theoretical heat transfer analysis of the gradient plate showed that a larger cross sectional area, specifically, a greater wafer

thickness, was needed to attain a highly linear gradient. Such a thickness was not readily available. The brittleness of the material caused additional concerns. Coupling and constraining a silicon gradient plate to the mounting fixture would have been difficult given the high brittleness.

The material that was finally selected was high conductivity C10100 Copper. This material was inexpensive and easily machinable. Its thermal conductivity is 391 W/m/K, more than twice that of the aluminum and silicon. While its thermal expansion coefficient, 17 μm/m/K, was slightly lower than that of the aluminum, it was a sacrifice when compared to the silicon. However, the selected design concept presented in the next section was able to allow this magnitude of expansion to occur in a predictable way and therefore this material property was acceptable.

Table 4-2. Summary of Gradient Plate Material Properties [4].

Material	Thermal Expansion Coefficient @ 293 K (μm/m/K)	Thermal Conductivity @ 293 K (W/m/K)
Diamond	1.2	990
6061-T6 Aluminum	26.6	167
Mono-crystalline Silicon	2.5	163
C10100 Copper	17.0	391

To ensure heat transferred from any volume along the plate was dominated by conduction, it was necessary not only to maximize the thermal conductivity of the gradient plate but also to have a high enough thermal resistance in the insulating layer. Since very thick insulations were undesirable for optical and other practical purposes, it was of interest to select an insulating material of minimal thermal conductivity. Several materials were considered.

Material selection was a trade off between cost, thermal conductivity, necessary material thickness, manufacturability, and optical considerations.

Three materials, silica glass, clear polycarbonate, and silica aero-gel, were of special interest for use as insulators because they are optically clear such that no slit would be required to image the capillary beneath the insulation.

The insulating value of Silica glass was not particularly good as it has a thermal conductivity of 1.38 W/m/K [4]. Clear polycarbonate is better since it has a thermal conductivity of 0.19 W/m/K [4]. While these are not extremely low conductivities, the optical benefits made these materials worth considering further. The thermal resistance could be raised to the necessary level simply by increasing the thickness. Silica aero-gel has a very low thermal conductivity, 0.02 W/m/K [4], an order of magnitude lower than standard clear polycarbonate. However, this material is very expensive and is not available in sheets or forms that could be used in this application.

Table 4-3. Summary of insulation thermal conductivities [4].

Material	Thermal Conductivity @ 293 K (W/m/K)
Silica Glass	1.38
Clear Polycarbonate	0.19
Silica Aero-gel	0.02
Polystyrene Foam	0.027
Mineral Wool	0.033
RF Aero-gel	0.06

Three other materials which are not optically clear were also considered good candidates. Polystyrene rigid foam insulation is inexpensive, easy to work with, readily available, and has a thermal conductivity of 0.027 W/m/K. However, its rated maximum service air temperature is specified as 75 °C [4]. Since temperatures of up to 99 °C might be utilized in the gradient plate, this was cause for concern. A simple experiment was conducted in which a piece of polystyrene was placed on a hot pad heated to various temperatures and left for multi-hour periods. The polystyrene was observed to warp in the presence of 110 °C temperatures and melt completely at 120 °C. If steady state temperatures were reached without overshoot, polystyrene could be considered an option.

A second material, mineral wool insulation, rated for temperatures up to 650 °C was also considered. It has a thermal conductivity of 0.033 W/m/K [36]. It can be obtained in a dense mat form, though not as easily workable as polystyrene, would allow it to be modified to fit the gradient plate.

The final non-optically clear insulating material considered was Resorcinol-formaldehyde (RF) Aero-gel paper. This material comes in sheets of 305 μm thicknesses and has a conductivity coefficient of 0.06 W/m/K [4]. This material was appealing because it was quite workable. It could be trimmed with a sharp knife. It is also able to withstand high temperatures.

Definition of the plate and insulation geometries, along with final insulation material selection will be discussed in the Section 4.5.2 and 4.5.4. Once the geometry is established, the heat sink and source sizing will also be described.

4.5.2 Heat Transfer Analysis to Assess Geometry Needs

The geometry of the gradient plate is affected by many requirements. There are limitations on the cross sectional area, requirements on gradient plate and insulation geometry to

produce a stable thermal gradient, and requirements to prevent buckling of the plate during thermal expansion. These requirements are all interrelated.

As discussed previously, in order to attain a stable thermal gradient, the heat transfer through any volume along the gradient plate must be dominated by conduction. This was first addressed by proper selection of the plate material in order to maximize the thermal conductivity coefficient. The other parameter to be optimized to achieve high thermal conductivity was cross sectional area. While conduction is a direct function of cross sectional area, and therefore maximizing cross sectional area may seem the answer, additional constraints and considerations exist.

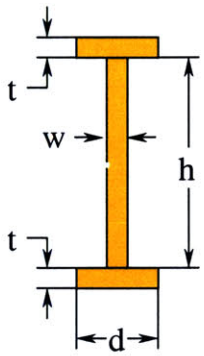

Figure 4-8. Gradient plate I-beam cross section geometry.

An obvious concern with allowing too large a cross sectional area is that of weight. Since the gradient plate has to be actuated in front of the detector, the inertia of the parts in motion limits the scanning bandwidth. However, this was not a major concern in this application as long as the cross sectional area was within reasonable limits.

Another concern regarding large cross sectional areas, specifically large thickness values for w in Figure 4-8, was two-dimensional thermal gradients in the plate. Ideally, the temperature on the front face of the plate would be the same as that on the back face. Since the heater source and sink are on the back face while the capillary is mounted in the front face, this is of notable

importance. The larger w is chosen to be, the larger the magnitude of any thermal gradient in that direction.

Another concern regarding large cross sectional area was related to controlling thermal expansion. The final design in Figure 4-7 shows the gradient plate bolted rigidly to the fixture. The thermal expansion of material in the region between the two columns of bolts induces stress in the fixture causing it to deform by yielding to axial stress or buckling under load.

Since many of these concerns are interrelated, iterative analysis was used to refine the gradient plate geometry based on all other constraints created by requirements of integrating with other system components. Through this iterative analysis, suitable values for the parameters which define the cross sectional area of the gradient plate were generated. Values for these parameters are shown in Table 4-4. With these parameters, analysis can now be conducted to find the necessary insulation thickness to achieve good temperature distribution linearity.

Table 4-4. Geometry parameters for gradient plate.

Parameter	Value (mm)
w	3.175
t	2
d	12.7
h	30

For this heat transfer analysis, several simplifying assumptions will be made. First, since temperature changes in the longitudinal direction are much larger than in the transverse direction, one-dimensional heat transfer along the length of the plate will be assumed. A solution will be sought only for the steady state conditions. Thermal conductivity will be assumed constant over the range of temperatures involved in the gradient. Radiation from the surface of the insulation

will be assumed to be negligible since, if properly designed, the temperature difference between the outer insulation surface and the environment will be small. Finally, since the back surface of the gradient plate should be easy to heavily insulate, it will be assumed to be adiabatic.

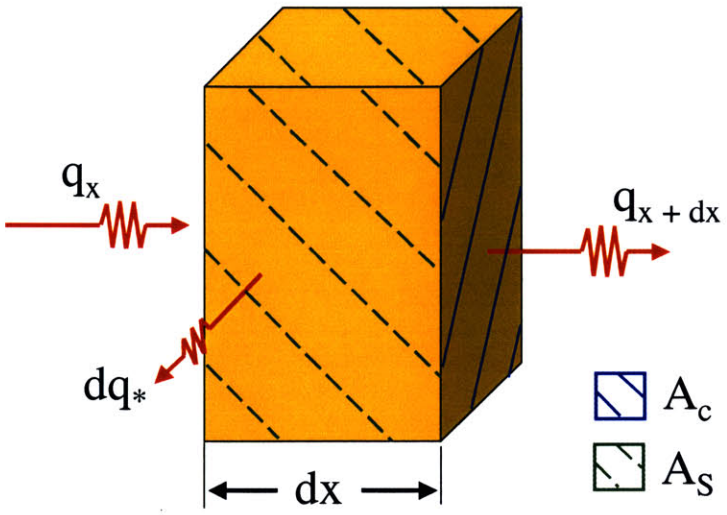

Figure 4-9. Infinitesimal section from gradient plate.

Slicing the gradient plate into strips of infinitesimal width, dx, the analysis is begun with Figure 4-9. The cross sectional area for this slice, defined by the variables in Figure 4-8, is given by

$$A_C = 2 \cdot w \cdot d + h \cdot t \,. \tag{4-1}$$

The surface area, A_S, exposed to the environment is given by

$$A_S = \left(2(d+w) + h - t\right) \cdot dx \,. \tag{4-2}$$

The variable represents The heat transferred into one side of the block via conduction, q_x, is a function of k, the thermal conductivity coefficient, dT/dx, the temperature gradient across the infinitesimal width strip, and the cross section area. The equation for q_x is given by

$$q_x = -k \cdot A_c \cdot \frac{dT}{dx} \,. \tag{4-3}$$

The heat exiting via conduction is represented by q_{x+dx}. Expanded, it can be written as

$$q_{x+dx} = q_x + \frac{dq_x}{dx}dx. \tag{4-4}$$

The term dq_* represents the heat dissipated from the block to the environment. This term is described by

$$dq_* = \frac{dA_S}{R}(T(x) - T_\infty), \tag{4-5}$$

where T(x) and T_∞ represent the temperature of the infinitesimal width block and the temperature of the environment respectively.

R is the equivalent thermal resistance created by the conduction of heat through the insulating material and the subsequent dissipation by convection and radiation. These thermal resistances act as shown in Figure 4-10. In the figure, t_I and k_I are the insulation thickness and conductivity coefficient respectively, h_c is the convection coefficient, and $1/h_R$ is the effective resistance to heat loss via radiation.

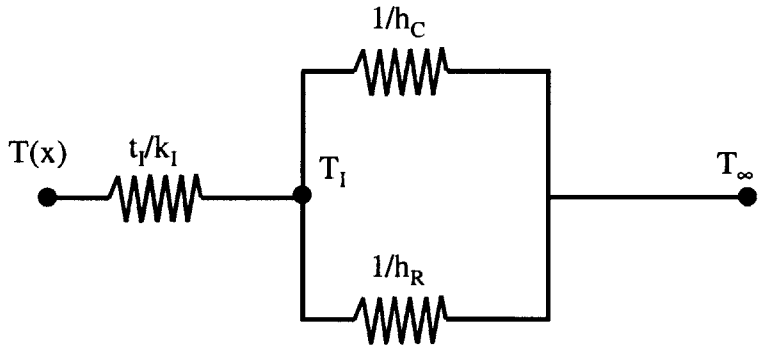

Figure 4-10. Equivalent thermal resistance circuit.

From this Figure, the equivalent thermal resistance can be written as

$$R = \frac{t_I}{k_I} + \left(\frac{1}{h_R + h_C}\right) \tag{4-6}$$

Based on the assumption that the difference in temperature on the outer surface of the insulation and the environment temperature, $(T_I - T_\infty)$, is small, it can be seen that the first term in Equation (4-6) dominates the value of R making the contribution of h_R and h_C negligible. These negligible terms can be ignored leaving the equivalent thermal resistance approximated by

$$R \approx \frac{t_I}{k_I} \tag{4-7}$$

Applying the first law of thermodynamics to the control volume of Figure 4-9 yields the conservation of energy equation given by

$$q_x - q_{x+dx} - dq_* = 0 \tag{4-8}$$

Substituting Equations (4-3), (4-4), (4-5), (4-7), this is expanded to the form given by

$$-k \cdot A_C \cdot \frac{d^2T}{dx^2} + \frac{dA_S}{dx} \cdot \frac{(T - T_\infty)}{R} = 0 \tag{4-9}$$

Now making a change of variables, let $\theta = T(x) - T_\infty$, and therefore $d\theta/dx = dT(x)/dx$. Inserting this relation into Equation (4-9) and expanding dA_S and A_C the governing second-order differential equation, is found to be

$$\frac{d^2\theta}{dx^2} - m^2\theta = 0, \text{ where } m^2 = \frac{(2(w+d)+h-t)\cdot k_I}{t_I \cdot k_p(2 \cdot w \cdot d + h \cdot t)}. \tag{4-10}$$

The solution to this differential equation is given by

$$\theta(x) = C_1 e^{mx} + C_2 e^{-mx} \tag{4-11}$$

where boundary conditions can be used to solve for the coefficients C_1 and C_2. These boundary conditions are given by prescribed temperatures at each end of the gradient plate. For our analysis example, a broad distribution will be chosen. These include $\theta(x = 0) = 40$ °C and $\theta(x = L) = 70$ °C. The actual endpoint temperatures will vary from experiment to experiment but for the purpose of analyzing deviation from linear, a large range represents worse case assumptions.

It is now necessary to select the appropriate insulation thickness and material to create a highly linear (conduction dominated) thermal gradient. The thickness of the insulation is practically limited by the focal length of the objective in the LIF system. The focal length of the objective implemented is 18 mm. Therefore, the insulating thickness will be limited to 15 mm.

The deviation from a linear temperature distribution for each insulation at this maximum allowable thickness I is now calculated. This information, when weighed with other important factors such as cost, manufacturability, and optical considerations, determines which insulation is optimal.

Table 4-5. Summary of thermal conductivity of strong candidates for insulating material [5].

Material	Thermal Conductivity @ 293 K W/m/K
Clear Polycarbonate	0.19
RF Aero-gel	0.06
Mineral Wool	0.033
Polystyrene	0.027

Plugging in the values of Table 1-1 into Equation (4-11) and solving for the coefficients using the given boundary conditions, a temperature distribution for each insulation is generated. This distribution is then subtracted from a perfectly linear distribution to develop a plot showing deviation from pure conduction. These results are shown in (4-11).

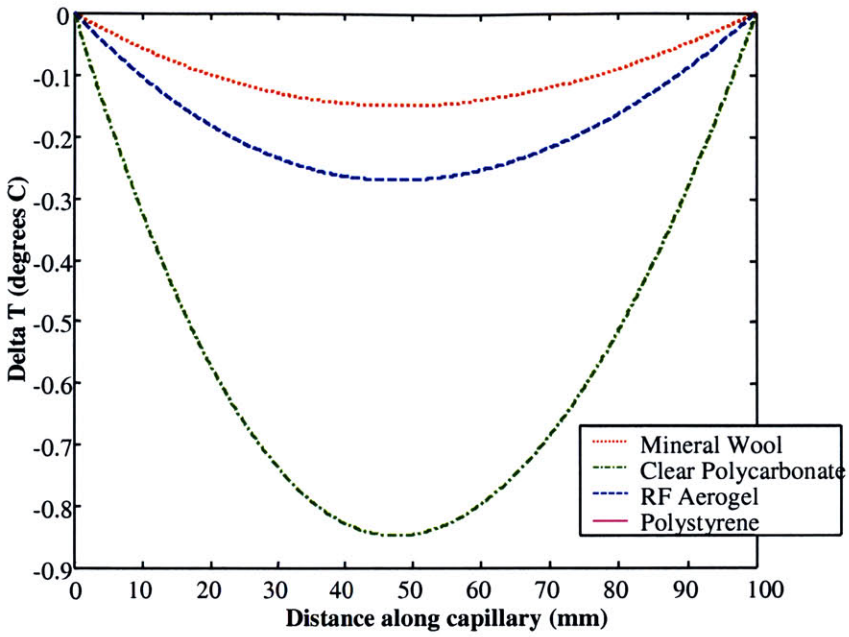

Figure 4-11. Difference between linear gradient and model for each insulation.

The deviation from linear is nearly 1 °C for the clear polycarbonate making it a poor choice. RF Aero-gel is also shown to have a rather large deviation in this idealized model. The performance of the mineral wool and polystyrene insulations are similar. Even though its maximum service temperature is marginally high enough for this application, the ease of use of the polystyrene far out weighs the fiber mat form of the mineral wool. Therefore it was chosen as the material of choice. In experiments, it was implemented successfully into the design without occurrences of the feared melting of the insulation.

4.5.3 Heater Sizing Requirements

Similar analysis was used to determine the necessary power output of the heat source. With all geometries and materials now specified, the analysis of the heater power can proceed.

In this case, we will analyze the system without breaking it into infinitesimal width strips but take a more macroscopic approach. A simple model of the system is shown in Figure 4-12.

Here T_H represents the "high side" temperature, T_C represents the "low side" temperature, and T_∞ represents the temperature of the environment. The unusual positioning of the t_I/k_I resistance is intended to reflect that it operates across a potential defined by T_{AVG} - T_∞ where T_{AVG} is the mean temperature, $(T_H + T_C) / 2$.

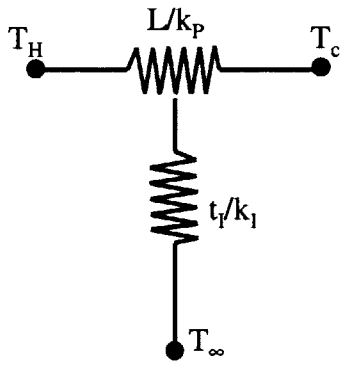

Figure 4-12. Model of heat transfer paths in system.

The first law of thermodynamics is applied to this system and is simply given by $q_{in} = q_{out}$. This is expanded based on the model to form

$$q_{in} = k_p \cdot A_C (T_H - T_C)/L + A_S \cdot k_I \cdot (T_{AVG} - T_C)/t_I . \qquad (4\text{-}12)$$

The amount of input heat required is therefore a function of geometries of the plate and insulation as well as their thermal conductivities. It is also a function of end point temperatures which might change from experiment to experiment. For a broad temperature distribution, T_H = 90 °C and T_C = 60 °C. For this case, q_{IN} = 14.4 W. Many experiments, however, will require a much tighter temperature range. For experiments shown in the results section, the temperature distribution T_H = 73.5 °C and T_C = 71.5 °C, q_{IN} = 2.0 W.

These requirements were met by TM-71-1.0-3.9M Peltier-effect thermoelectric modules from Advanced Thermoelectric Products (Nashua, NH). One was installed on each end of the

gradient plate. It was found through experimentation that one Peltier-effect thermoelectric used as the heater on end working with a simple muffin fan on the other could establish the broad temperature range. However, even with the fan off the dissipation at the "low side" end was too fast to establish the tighter temperature distribution. Rather than adding more insulation to the "low side" end (which is essentially un-insulated), an additional thermoelectric was added to the "low side" end to make the temperature there more controllable. Appropriate voltages were determined experimentally for each of the heaters to achieve desired end point temperatures.

4.5.4 Avoiding Distortion, Yielding Under Stress, and Buckling

The thermal expansion in the gradient plate could produce a number of undesirable mechanical effects if designed improperly. The three main concerns are yielding of the gradient plate under axial stress, yielding of the fixture under bending stress, and deformation of the gradient plate due to buckling. If each of these are avoided, the design should hold the capillary in the optical scannable plane despite the thermal changes.

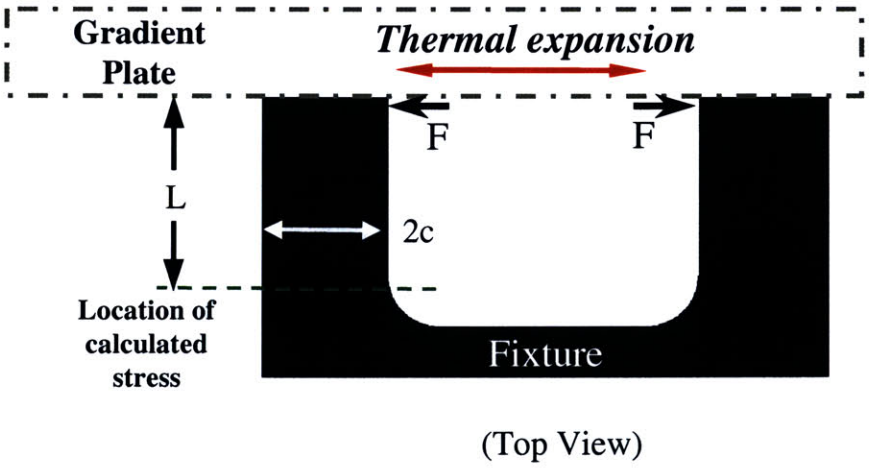

Figure 4-13. Diagram of induced force on fixture.

4.5.4.1 Axial Stress in Gradient Plate

Axial stress if the gradient plate is explored first. The stress is calculated under a worst case assumption that the arms of the fixture undergo no deflection such that all strain induced by thermal expansion builds up as internal stress in the gradient plate. In this case, the axial stress can be computed from Hooke's Law is

$$\sigma = E_{CU} \cdot \varepsilon = E_{CU} \cdot CTE \cdot \Delta T, \tag{4-13}$$

where ΔT is the average temperature difference between elevated and ambient temperatures, CTE is the coefficient of thermal expansion of the gradient plate material, and E is its modulus of elasticity. In the worst case, ΔT could be 55 °C. For C10100 copper, discussed previously as the material of choice for the gradient plate, CTE = 17 μm/m/K and E = 125 GPa [4]. These values result in a maximum thermally induced stress of σ = 117 MPa. The yield strength of this copper is 195 MPa [4]. Therefore, even in a worst case scenario, axial yielding of the gradient plate will not be a problem.

4.5.4.2 Stress Induced in Fixture

The U-shape of the fixture (see the top view depiction in Figure 4-13) was necessary to allow room for any required heat sink mechanism. When the gradient plate expands, the arms of the fixture will feel a bending moment created by the force F and distance L. The amount of force that the arm feels is based on the way it deflects in response to the force.

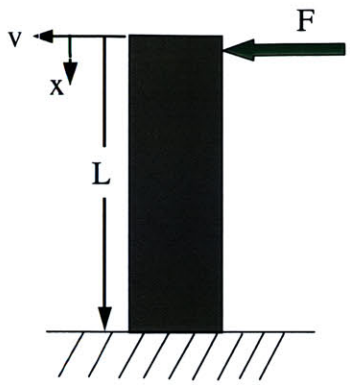

Figure 4-14. Free-body diagram of arm of fixture.

From the free-body diagram, the moment, taken positive in the clockwise direction, is given by

$$M = -F \cdot x . \tag{4-14}$$

Based on the principles of mechanics of materials, the moment can be related to the radius of curvature of the beam, $1/\rho$, its elastic modulus, E, and its moment of inertia, I, by

$$\frac{1}{\rho} = \frac{M}{E \cdot I} \tag{4-15}$$

This equation assumes that the deformation of the beam, caused by both internal shear force and bending moment, is dominated by the bending moment. This is true when the beam has length much greater than its depth. This assumption is marginally satisfied in this case.

The curvature of the beam can be estimated as $1/\rho = d^2v/dx^2$ for small deflections which yields

$$M = E \cdot I \cdot \frac{d^2 v}{dx^2} . \tag{4-16}$$

Integrating Equation (4-16) twice, an expression for the displacement, v, as a function of x can be determined. Using the boundary conditions $dv/dx = 0$ at $x = L$ and $v = 0$ at $x = L$ the

coefficients that arise in the integration can be found. Finally, recognizing that the maximum deflection occurs at x = L,

$$v_L = \frac{-F \cdot L^3}{3 \cdot E \cdot I}. \tag{4-17}$$

Rearranging to solve for the force necessary to deflect a cantilevered beam a distance v_L,

$$F = \frac{-3 \cdot E \cdot I}{L^3} v_L. \tag{4-18}$$

The moment created at the base of the cantilevered beam is the product of F and L. If it is assumed that all of the thermal expansion in the gradient plate goes into equal deformation of the two arms (a worst case assumption), then $v_L = 1/2 \cdot CTE \cdot \Delta T \cdot d_{C2C}$ where d_{C2C} is the center to center spacing of the bolts which mount the gradient plate to the fixture. This yields the expression for the bending moment at the base of the cantilever given by

$$M = \frac{3 \cdot E \cdot I}{L^2} v_L = \frac{3 \cdot E \cdot I}{2 \cdot L^2} \cdot CTE \cdot \Delta T \cdot d_{C2C} \ . \tag{4-19}$$

From this information, the summation of the bending and shear stress is calculated as

$$\sigma = \frac{M \cdot c}{I} + \frac{F}{A_f} = \left(\frac{3 \cdot E}{L^2} v_L \right) \cdot c + \frac{3 \cdot E \cdot I}{L^3 \cdot b \cdot 2 \cdot c} v_L. \tag{4-20}$$

Noting that in Equation (4-15) through Equation (4-20), the fixture geometry parameters L and c are those shown in Figure 4-13 and Figure 4-14. The inertia, I, is given by $I = 1/12 \cdot b \cdot (2c)^3$. The cross sectional area of the fixture is $A_F = b \cdot 2c$, and b is the thickness of the fixture into the plane of Figure 4-13.

The elastic modulus, E, is also for the fixture material. Invar was selected as the fixture material because of its very low coefficient of thermal expansion (1.3 μm/m/K) [4]. A low CTE and small geometry would mean minimal movement of the gradient plate due to the change in temperature of the fixture. The yield strength of Invar is 679 MPa. The fixture design must not

allow the stress induced by the expansion of the gradient plate to exceed the fixture's yield strength.

From Equation (4-20) the stress is found to be σ = 202 MPa. Since this is well below the yield strength of the fixture and given the use of worst case conditions, it can be assumed that the fixture will not yield due to the thermal expansion of the gradient plate.

4.5.4.3 Buckling Analysis of Gradient Plate

The third and final concern to be checked is buckling of the gradient plate. When a compressive load is applied to a columns that are long and slender, the loading may be large enough to cause the column to deflect laterally. This deflection is called buckling.

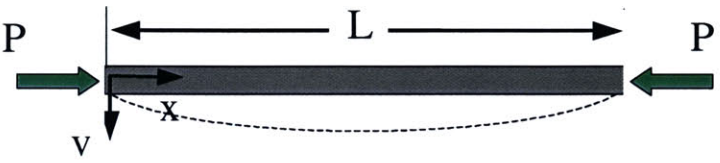

Figure 4-15. Free-body diagram of ideal column under compressive load

The critical load for the column can be developed from the same relationship as was used in the previous analysis given by Equation (4-16) where in this case the moment M = -P · v where P is the compressive load and v is the displacement of the beam from the x axis as depicted in Figure 4-15. Substituting the relation for M yields the differential equation,

$$\frac{d^2v}{dx} + \left(\frac{P}{E \cdot I}\right)v = 0. \tag{4-21}$$

This is a homogenous, second-order, linear, differential equation with constant coefficients. It has a solution given by

$$v = C_1 \sin(\sqrt{\frac{P}{EI}}x) + C_2 \cos(\sqrt{\frac{P}{EI}}x)\,. \tag{4-22}$$

Since v = 0 at x = 0, $C_2 = 0$. Since v = 0 at x = L, $(P/EI)^{0.5} \cdot L = n\Pi$. The smallest value of P is obtained when n = 1, so the critical load for the column is therefore given by

$$P_{CR} = \frac{\pi^2 \cdot E \cdot I}{L^2}\,. \tag{4-23}$$

Assuming the gradient plate behaves as an ideal column, the critical load can be found from this equation by substituting $E = E_{CU}$ (where E_{CU} is the elastic modulus of 10100 Copper) and $L = d_{C2C}$ (where d_{C2C} is as described previously). From this, the critical load to induce buckling is determined to be 700 kN.

If worst case conditions are assumed such that the fixture arms undergo no deflection and therefore all thermal expansion induces internal, compressive stress in the gradient plate, the force, P, on the gradient plate can be found from

$$P = 1/2 \cdot \sigma \cdot A_C\,, \tag{4-24}$$

where σ is given by Equation (4-13) and A_C is the cross sectional area of the gradient plate.

Based on the maximum value of σ calculated previously, $P_{max} = 8.4$ kN. Therefore, the plate is in no danger of undergoing buckling. It should remain flat during any thermal expansion allowing good optical alignment. In Chapter 7, this analysis is validated as results show good optical alignment.

4.6 Manufacturing of Gradient Plate

The last section of this chapter is used to describe the manufacturing process for the gradient plate. One of the design criteria was to minimize vertical tolerances on the capillary positioning. Holding tight tolerances on the gradient plate was critical to achieving this goal.

All the machining for the gradient plate was done on the HAAS machining center (Model #OE, HAAS Automation, Los Angeles, CA). The process of machining the I-beam shape itself was relatively straight forward. It began with a 10100 copper work piece measuring 12.7 mm × 38 mm. In removing the material to create the I shape, extreme care was taken not to over tighten the vise on the work piece which might induce internal stresses into the part. When the work piece was unclamped such internal stresses would cause the part to deform, leaving it out of tolerance. Feed speed, spindle speeds, and cutting depths were kept very conservative in order to minimize forces on the part by the tool.

The major challenge in machining the gradient plate was in cutting the groove for the capillary. Original attempts to machine the groove were based on use of the sink EDM (Electro-Discharge Machining) (Roboform 30, Charmilles Technologies, Geneva, Switzerland). Electro-discharge machining uses large pulsed voltages between the work piece and an electrode (the cutting tool) to shape the work piece. During the pulse an arc develops across the gap between the work piece and electrode. Material local to the arc reaches temperatures that transform it to a plasma state. Simultaneously, gases released during the state change of the materials create a bubble. At the end of the pulse, this bubble implodes, pulling material out of the work piece and electrode. This process is repeated at high frequency to carryout the machining process. With optimized control, these machines can cut any material that is electrically conductive to tight tolerance and a fine surface finish.

This operation used a graphite tool machined on the wire EDM (Robofil 1020SI, Charmilles Technologies, Geneva, Switzerland) which was essentially a blade of width 250 μm and length 13 mm. This tool when sunk into the copper trial work piece to a depth of 190 μm and then moved laterally down the plate making the groove. Ten passes were used. Before each pass, the bottom edge of the wearing tool was re-indicated. Though machining settings were

finally achieved that could produce a groove of constant desired width, the procedure was not ultimately implemented. As seen in Figure 4-16, the surface finish of the groove was poor. With better optimized settings on the sink EDM this problem could have been eliminated however it is uncommon to have a copper work piece in sink EDM operations. In fact, it is very common to use copper as the tool. Therefore factory optimized settings for this combination of tool and work piece materials were not available. This process of custom optimization was difficult and abandoned in favor of machining the groove via milling.

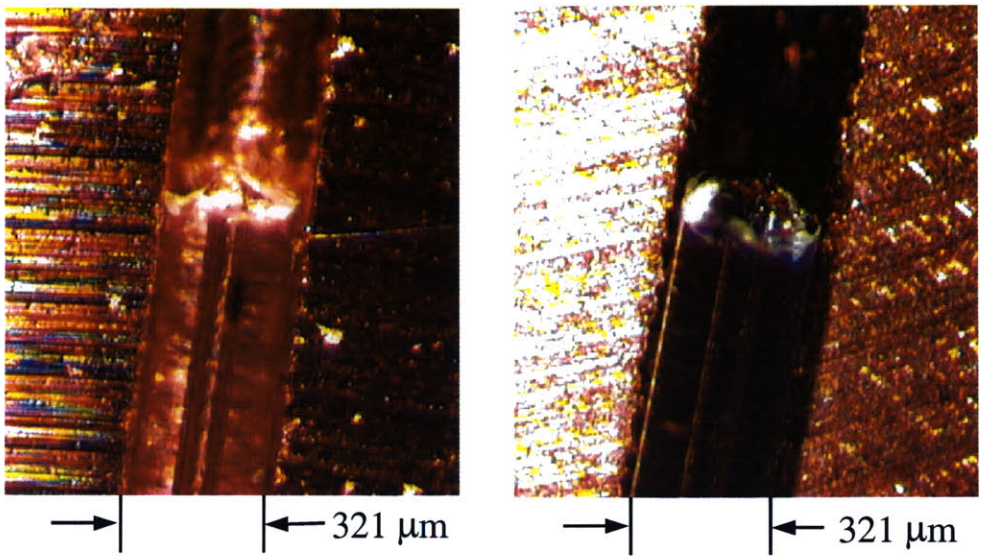

Figure 4-16. Capillary end in groove machined by milling (left) and Electrical Discharge Machining (right).

The process that produced better results for the purposes of this project was high speed milling. An end mill with two teeth and 254 μm diameter served as the cutting tool. In order to cut the desired geometry, multiple passes with a 15 μm depth of cut and 500 μm/s feed speed were made until the final depth of 210 μm was reached.

The maximum spindle speed of the HAAS machining center is only 100 rev/s. Such a spindle speed is not well suited for this diameter cutting tool. To attain higher spindle speeds, a spindle speed amplifying transmission was added (Koyo-Showa TPU60-BT40, Koyo Seiko Co.

Osaka, Japan). Cutting was done at 500 rev/s, the maximum speed with the spindle transmission. The combination of these cutting parameters was very conservative yielding little tool wear and excellent surface finish.

Due to non-concentricity of the tool axis and the axis of rotation, the 254 μm tool made a cut of width was ~345 μm. While this deviation seems large, this dimension was excellent for the groove. Therefore, no attempt was made to decrease this degree of misalignment.

The groove cut via milling is shown in Figure 4-16.

Chapter 5
Design and Integration of Optical, Electrical, Data Acquisition, and Mechanical Systems

In this chapter, the final configuration for the optical, electrical, data acquisition/software, and mechanical (thermal gradient and scanning) systems are documented. The components utilized in each system are described. Several important design issues are discussed including data acquisition sampling rate and filter cut-off frequency, as well as optimal pinhole size for the confocal optical system. Finally, diagrams and photographs are given to illustrate the instrument configuration. The complete instrument is shown in Figure 5-1. Each subsystem will be described independently.

5.1 Optical System

In this section, a description of the optical configuration is first described. Then an analysis is conducted to determine the optimal pinhole size for TGCE.

5.1.1 System Configuration

The optical system is a common confocal, on-column laser induced fluorescence (LIF) capillary electrophoresis arrangement. Variations on this arrangement have been described by many authors [7,9,11,25,30]. A schematic of the optical system is shown in Figure 5-2.

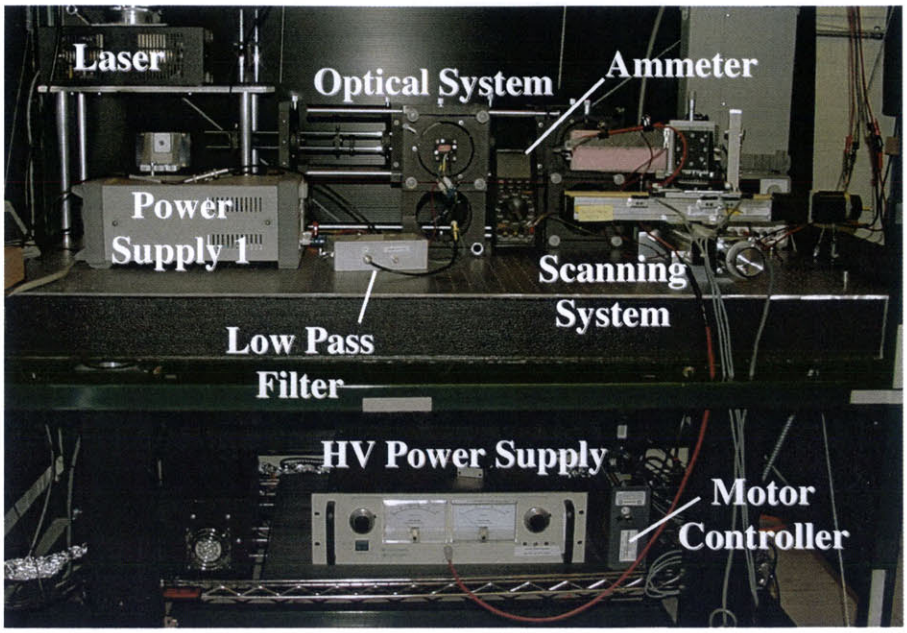

Figure 5-1. View of complete instrument system (excluding PC and two power supplies).

In TGCE, the laser beam (Uniphase air-cooled argon ion laser, 488 nm wavelength) passes through the dichromic mirror and is focused by the objective (IC10, Olympus, Melville, NY, NA = 0.25, f = 18 mm) onto the capillary. Reflected, induced fluorescence is then transmitted back through the objective. This dichromic mirror reflects all wavelengths above 488 nm. The peak fluorescence emission of the fluorescein probe used was approximately 540 nm. Therefore, the fluorescence signal was reflected into the detection arm of the optical system. This signal passed through a 488 nm notch filter (Omega Optical, Brattleboro, VT) to further attenuate any laser light still remaining. A plano-convex lens (f = 50 mm) focused the signal through the confocal pinhole. Signal passing through the 500 um diameter pinhole was detected by a HC120-01 Hamamatsu photo-sensor module (PMT). All optics were mounted in a

Spindler-Hoyer optical framework. Photographs of the system are shown in Figure 5-3 and Figure 5-4.

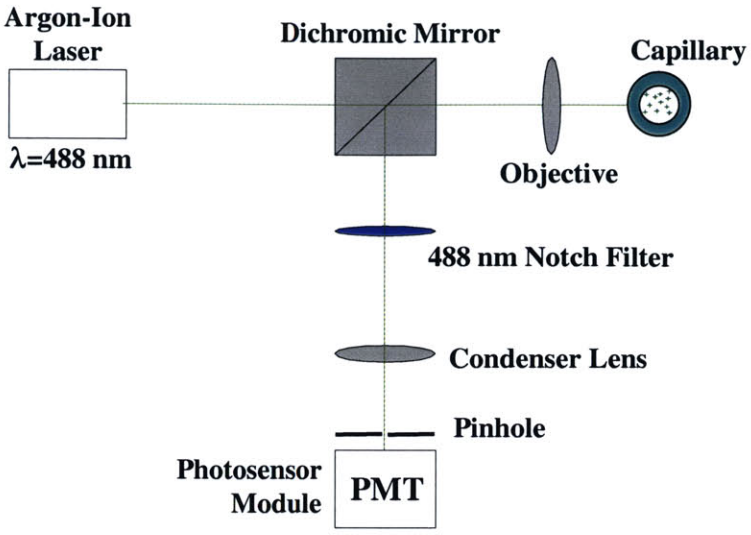

Figure 5-2. Common optical configuration to image capillary electrophoresis.

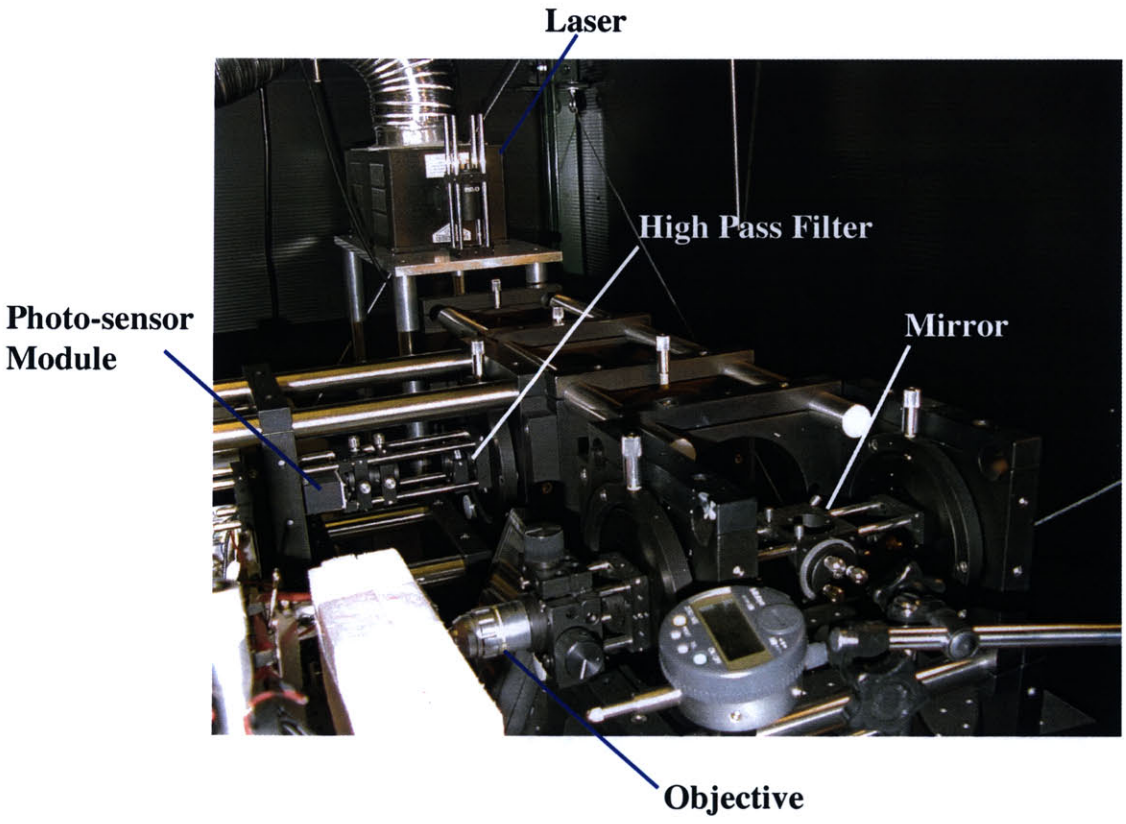

Figure 5-3. Optical system.

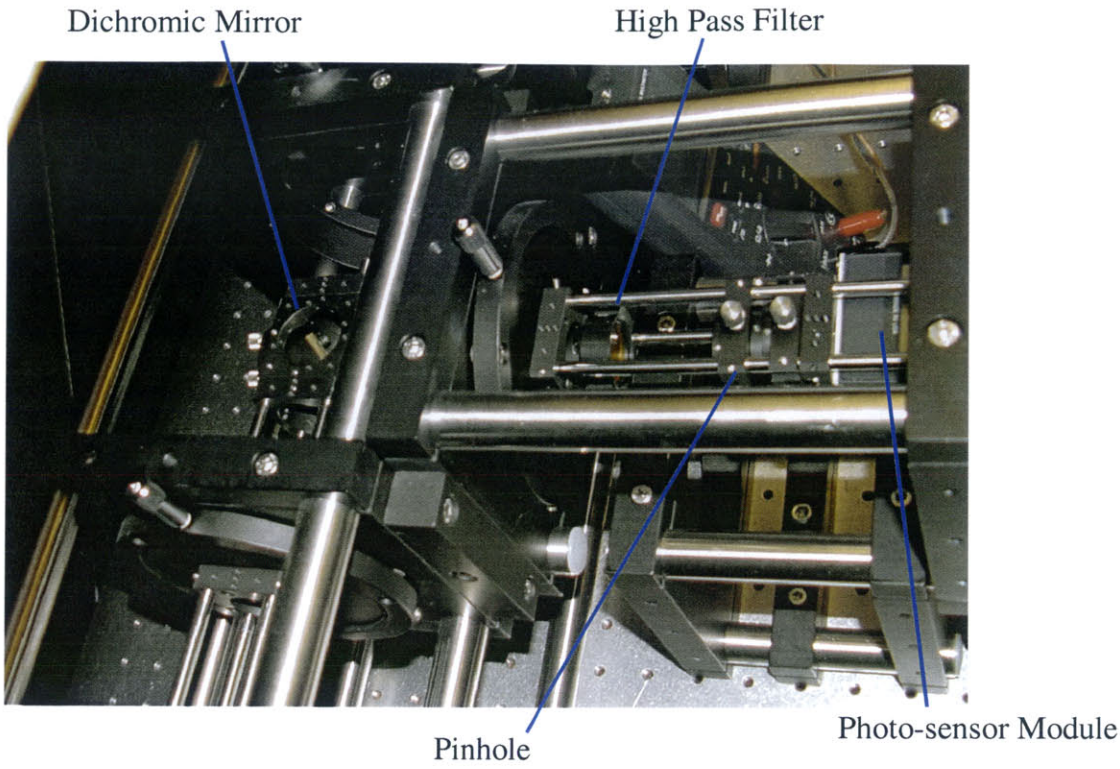

Figure 5-4. Close up of detection arm of optical system.

5.1.2 Pinhole Size Optimization

The confocal microscope provides significant optical advantage for fluorescence microscopy by discriminating against out-of-focus background. It achieves this via a pinhole aperture residing in front of the detector which rejects light that has originated outside a characteristic confocal volume. Any confocal application will have tradeoffs specific to the sample to be imaged which dictate the optimal pinhole radius for maximum signal-to-noise ratio.

In the past decade, several authors have addressed the maximization of signal-to-noise by optimization of pinhole radius [40,41,44,45]. These works have little relevance to the TGCE system, however, because of several major differences. Various assumptions regarding the source of background and sample fluorescence are made but none describe the TGCE system in which the imaged sample is uniformly distributed and encapsulated in sources of background fluorescence. Additionally, all authors conduct their analysis for static systems. The dynamic

scanning involved in TGCE requires that tolerances describing the uncertainty of the position of the imaged sample be considered in the analysis.

5.1.2.1 Approximations and Assumptions

A confocal microscope arrangement having a point source and a point detector can be shown to have a resolution volume that is ellipsoidal with minor radius r in the lateral direction and major radius R in the axial direction [40]. The minor radius is defined by the first zero of the Airy profile. The major radius is defined by the first zero of the sinc function. The aspect ratio of the ellipsoid for this idealized geometry is 0.3. To aid in approximating the pinhole size, this ellipsoidal resolution volume will be assumed applicable to the finite aperture TGCE system.

If it is assumed that auto-fluorescence of the gel matrix is not the dominant source of background photons, the background would not substantially increase until the resolution volume began to encompass the capillary wall. Figure 5-5 demonstrates the relative geometry of the ellipsoidal confocal volume and capillary for the case in which the major radius of the ellipsoid is equal to the inner radius of the capillary.

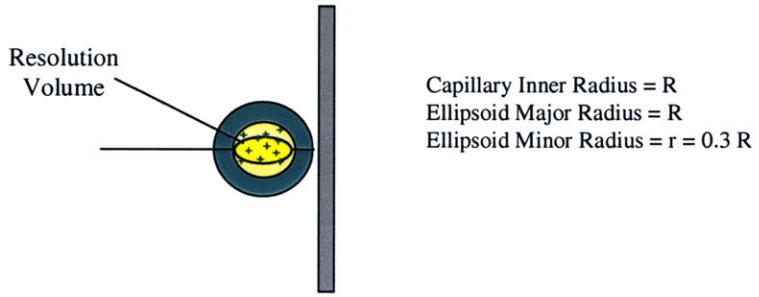

Figure 5-5. Resolution (confocal) volume within capillary.

Such a resolution volume is not optimal however, since an ellipsoid of this geometry encompasses only 20% of the total volume of the equivalent width cylinder.

$$\text{Volume of Cylinder} = \Pi R^2 h = \Pi R^2 h = \Pi R^2 2r = 2*0.3*\Pi R^3$$

$$\text{Volume of Ellipsoid} = 4 / 3\ \Pi\ r^2\ R = 4 / 3 * 0.3^2\ \Pi\ R^3$$

$$\rightarrow \quad \text{Ratio of Volumes} = 0.2$$

A larger resolution volume is needed to maximize the detected fluorescence.

5.1.2.2 Tolerance Analysis

In TGCE, there exists dynamic uncertainty in the position of the capillary with respect to the focal point of the objective. It is of primary importance that the confocal volume be of adequate size such that where ever the capillary is positioned within its tolerance range, the inner diameter is still within the confocal volume. Since the confocal volume has an ellipsoidal shape, the alignment is most sensitive to tolerances in the vertical direction. Therefore, the sources of error associated with vertical positioning must be identified and quantified. Some sources of error are easily quantified since they are given in the specifications of components of the system. Other sources of error, such as alignment errors, are more difficult to quantify. In these cases, estimated error bands are made based on experimental measurements of the system.

There are sources of error in alignment associated with each degree of freedom of the system. Since this analysis is restricted to only vertical alignment, there is angular positioning error and vertical positioning error. The vertical positioning is finely adjustable with the linear stage. Its tolerance is assumed small, ±1 μm. Zero angular error is defined as perfect alignment of the capillary with the axis of scanning motion. The vertical tolerance associated with the angular error is greatest at the limit of scanning travel farthest away from the mounted end of the gradient plate. From measurements taken during experiments, the positioning tolerance at this location is assumed to be ±15 μm.

The capillary groove also provides a source of error. Ideally, the capillary groove would be perfectly straight and exactly the same width as the outer diameter of the capillary. Since the

groove is actually larger than the capillary, it is possible for the capillary to take a wave shape inside the groove. Such error cannot be compensated for by alignment adjustments. In Chapter 4, the width of the groove was given as 345 μm. The outer diameter of the capillary with coating removed was measured as 325 μm. It is assumed that the difference between these values represents the error associate with straightness of the groove and waviness within the groove. This is justifiable since the straightness tolerances alone are likely only ±1 μm based on the method of manufacture. Therefore, the tolerance associated with this source of error is ±10 μm.

The linear stage (000-9141-01; Parker, Irwin, PA) which creates the scanning motion contributes error as well. The specification sheet for this product indicates a flatness tolerance of ±12 μm. Deviations from motion in a perfectly flat plane cannot be compensated for by alignment.

Table 5-1. Summary of tolerances.

Source of Error	**Tolerance (μm)**
Vertical Alignment	±1
Angular Alignment	±15
Capillary Groove	±10
Linear Stage Flatness	±12
Summation	**±38**

The sources of error and their associated tolerances are summarized in Table 5-1. The upper and lower limits of the inner diameter position are illustrated in Figure 5-6 by the dotted, red circles. Given this tolerance constraint, the optimal pinhole diameter is one that maximizes the detected signal by creating a confocal volume that images the capillary wherever it is within its tolerance band. This concept is also illustrated in Figure 5-6. Restricting the confocal volume to a smaller size would lead to variable sensitivity over the length of the capillary since the

volume of the inner diameter which is inside the confocal volume would change with scanning position.

5.1.2.3 Using Ray Optics to Approximate the Pinhole Size

In order to derive an approximate solution for optimal pinhole size, simple ray optics are utilized. Figure 5-6 illustrates the simple ray optics calculation. From this figure, the required pinhole radius, r_p, is calculated as

$$r_p = \frac{f_1}{f_2} \cdot r \tag{5-1}$$

based on the focal lengths, f_1 and f_2, and the minor radius of the necessary minimum resolution volume radius, r.

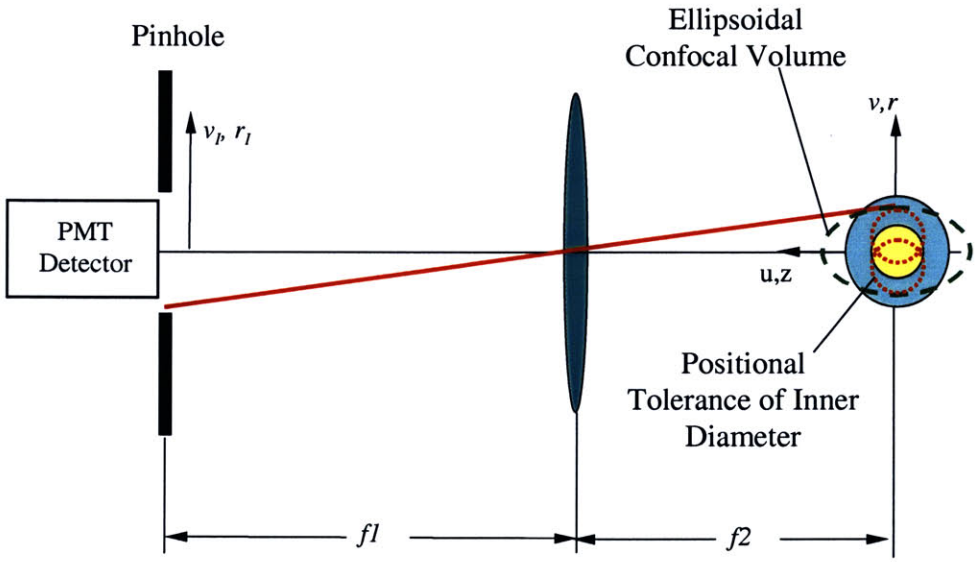

Figure 5-6. Pinhole size dependence on positional tolerance.

For the TGCE setup, f_1 = 50 mm, f_2 = 18 mm. The minimum necessary resolution volume minor radius is the inner radius of the capillary plus the tolerance magnitude, a total radius of 75.5 μm. This results in r_p = 210 μm. Therefore a pinhole of 400-500 μm diameter would be optimal for the TCGE system.

5.2 Data Acquisition/Software System

The voltage signal from the photo-sensor module passed through a custom built analog second-order Butterworth low pass filter with a cut-off frequency (-3 dB) of 715 Hz. The filter output was measured by the 18 bit Allios data acquisition board (board designed and built by Sylvain Martel, MIT Bioinstrumentation Lab) at 400 Hz. The procedure used to design this system is now discussed. A brief description of the software used to acquire data and control the system is also included.

5.2.1 Selecting Filter Cut-off and Data Measurement Frequencies

The selection of the cut-off and measurement frequencies were made carefully. A brief discussion of important considerations to define the optimal sampling rate and filter cut-off frequency is now presented. The discussion begins with a description of the physical kinetics behind a typical signal to understand how it may be modeled, then fits this model to the experimental data to describe a noise-free signal. Finally, Fourier analysis is performed on the model to show the range of important frequencies. From this, optimal filter design and sampling rate are determined.

5.2.1.1 DNA Migration in a Band

As the DNA migrates through the capillary it travels as a band. In a perfect world, DNA of the same net charge would travel as a plane, all strands moving simultaneously together through the gel. However, there are three primary reasons why this does not occur.

First, since the DNA molecules are initially uniformly, spatially distributed in the sample vial before electrophoretic injection, some molecules are closer to the entrance of the capillary

than others. Thus when the potential is applied, some molecules make it in to the capillary before others of the same length.

Radial temperature distribution which exists in the capillary is a second reason for "peak spreading." Ohmic heating occurs in the gel via its electrical impedance and the current being transmitted through it. Heat is dissipated from the gel via convection and radiation from the surface of the capillary. This heat flow pattern produces a temperature distribution in the capillary in which the center is at a higher temperature than points on the circumference. Since migration impedance is a function of temperature, DNA molecules traveling near the center of the capillary travel faster than those nearer the capillary surface.

Electroosmotic flow along the capillary wall is another reason the DNA travels in a band instead of a plane. Just as the negatively charged DNA molecules are migrating toward the positive terminal, there are positively charged ions in the solution migrating toward the negative terminal. The solid surface of the capillary wall has an excess of anionic charge resulting from the ionization of the surface functional groups (silano molecules). When the gel is injected into the capillary, counter ions to these anions move from uniform distribution in the gel solution to form a double layer on the capillary wall. The positive ions from the solution that have now concentrated at the capillary wall will be pulled toward the negative terminal during electrophoresis. Their motion disrupts the motion of the DNA molecules causing peak spreading. Steps taken to minimize electroosmotic flow are discussed in the Chapter 6.

The measured signal is a function of the distribution of the DNA molecules in the band. Data taken during a TGCE experiment in which the capillary was scanned at 50 mm/s past the detector with measurements taken at 100 Hz is shown in Figure 5-7. The width of the peak in such results is a direct function of the three "peak spreading" phenomena.

5.2.1.2 Frequency Content of Ideal Signal

The distribution of the DNA molecules in the migrating band takes on a form similar to a Gaussian density function as evidenced by the results shown in Figure 5-7 and other results [13]. In Figure 5-7, the red dots represent intensity measurements taken from a single scan across the capillary during a TGCE experiment. The equation for the Gaussian density function,

$$y = \frac{A}{\sigma\sqrt{\pi}} \cdot \exp\left(-\frac{(x-\mu)^2}{2\sigma^2} \right), \tag{5-2}$$

is non-linearly dependent on three parameters: A, the scaling factor, μ, the peak mean, and σ, the peak standard deviation. This model, represented by the blue line in Figure 5-7, was fit using a non-linear, least squares, Marquardt minimization routine discussed in Appendix B. The best fit parameters are shown in the figure.

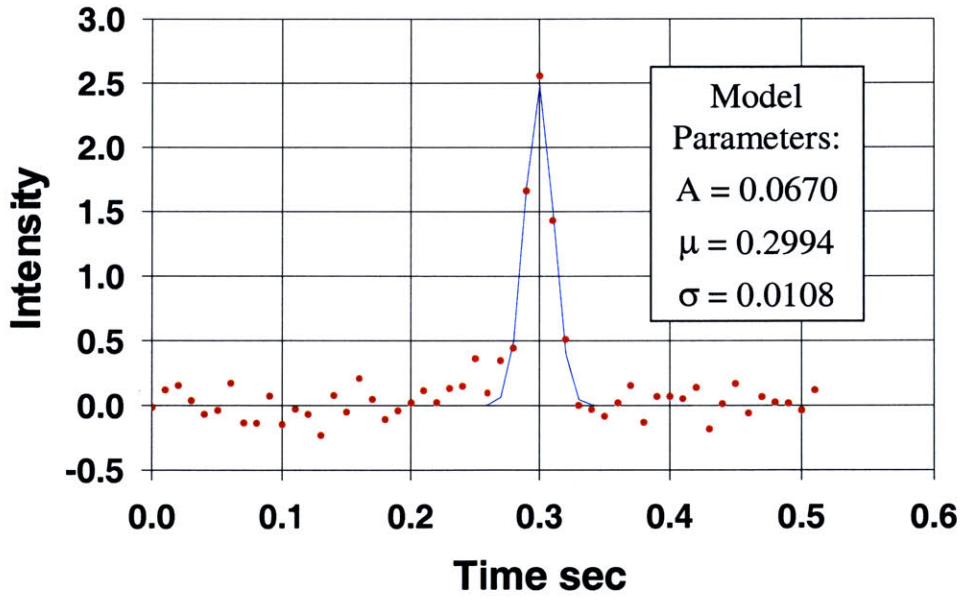

Figure 5-7. Intensity data from a single pass during a scanning experiment shown with fitted model.

With the model defined, an ideal signal, evaluated at 10,000 samples/s, was simulated in Matlab. This was essentially a reconstruction of the fitted model with a much higher sampling rate.

To determine the frequency content, the idealized signal was transformed to the Fourier domain. The results, generated in Matlab via the FFT command, are given in Figure 5-8 and shows that virtually no information is contained at frequencies above 50 Hz.

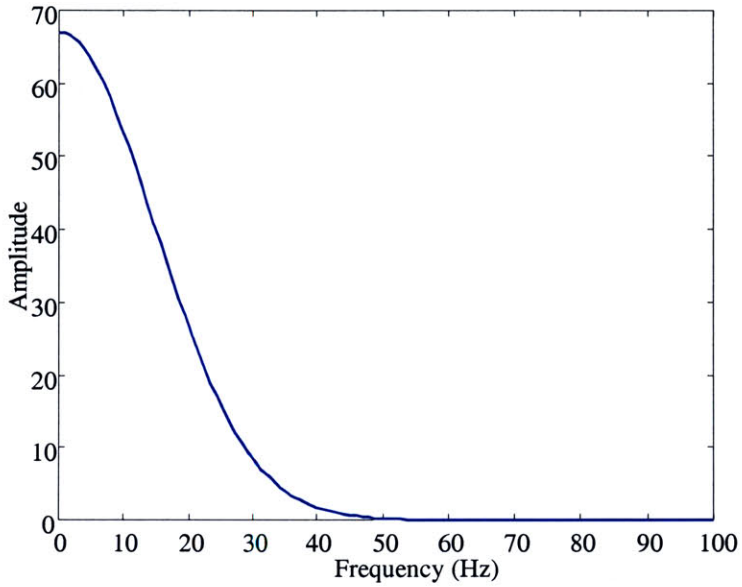

Figure 5-8. Fourier transform of 10,000 Hz idealized model

5.2.1.3 Cut-off Frequency for Filter

Based on the Fourier analysis, it can be concluded that minimal phase lag from the analog filter should be tolerated for frequencies up to 50 Hz. Through iteration with Matlab simulation of a second order filter, the cut-off frequency was adjusted until a solution was found for which the phase lag was less than 6 degrees for frequencies less than 50 Hz. The second-order Butterworth filter was built into hardware following the configuration given by Horowitz [19] where the cut-off frequency (-3 dB) is related to the resistance and capacitance values by

$$RC = \frac{1}{2\pi \cdot f_C}. \tag{5-3}$$

A gain/phase frequency response plot for the custom-built filter is shown in Figure 5-9. This plot was generated using the Hewlett-Packard Dynamic Signal Analyzer (HP3562A). The phase at 50 Hz was measured to be –5.95 degrees, as designed.

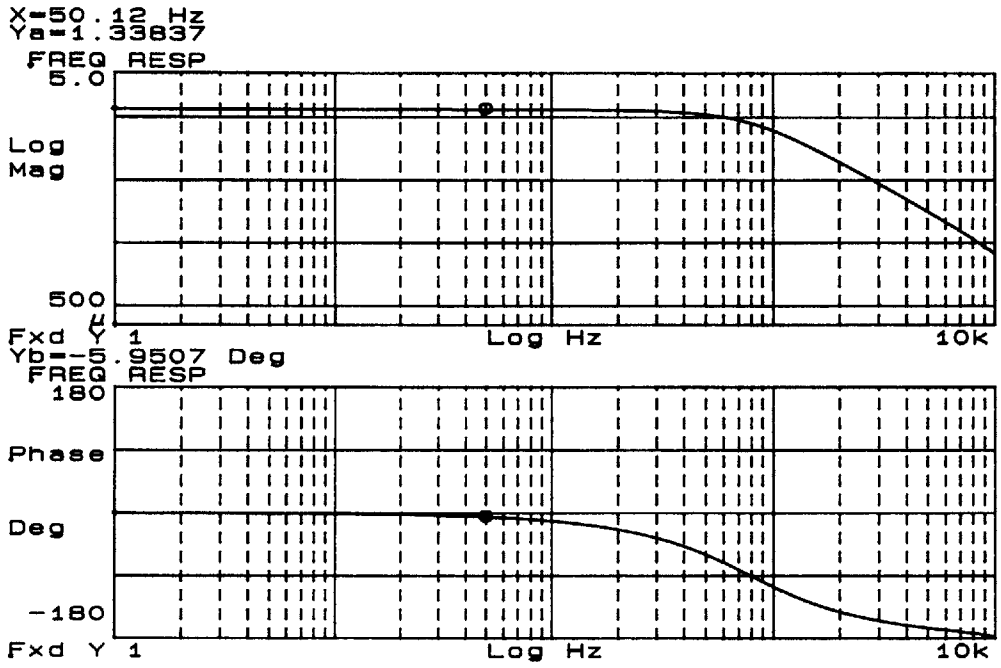

Figure 5-9. Frequency response for second-order Butterworth filter

5.2.1.4 Sampling Rate

In order to get a good representation of magnitudes at 50 Hz, a sampling rate of 400 Hz was selected. Frequencies above the Nyquist frequency (200 Hz) will be aliased to lower frequencies. It would have been desirable to lower the filter cut-off frequency to attenuate frequencies above the Nyquist, however the need to avoid introducing phase lag into the signal must take precedence.

5.2.2 Software

All software used to control the experiment and acquire data was written in Microsoft Visual Basic 6.0. This software sent commands to the motor controller for scanning. It also recorded filtered data from the photo-sensor module via the Allios data acquisition board. It contained an easy-to-use user interface with functionality that included user customized initialization of experimental parameters such as scanning speed, distance, acceleration, starting position, and PMT gain voltage. It also provided feedback to the user to confirm that all initializations were properly completed. The software plotted data after each scan to allow the user to interpret results in near real-time. This proved to be a very useful feature. Finally, the software recorded all data to a file in which each column of data represented all data from a single scan.

5.3 Scanning/Thermal Gradient System

Many design details of the thermal gradient plate, fixturing, and insulation were described in Chapter 4. In this section, the remaining details are covered. These include a description of the components for alignment and scanning. It also includes a description of the temperature measurement system.

Four stages were utilized to orient the capillary into optical alignment. These included the vertical (TB80-25, Spindler & Hoyer) and longitudinal linear stages (404140XR; Parker, Irwin, PA), and two angular positioning stages (124-0055; OptoSigma, Santa Ana, CA). A second Parker linear stage was used to scan the capillary in front of the objective. Each Parker stage had a 150 mm travel length with a 5 mm/rev thread pitch. These stages were driven by micro-stepping motors (ZETA57-83-MO; Compumotor, Rohnert Park, CA) and controllers (ZETA6104; Compumotor, Rohnert Park, CA). The Zeta stepper motor units can achieve 25000

steps/revolution. Commands were sent to the controller from a personal computer (PC) (450 MHz Pentium II, Microsoft Windows NT 4.0) via a serial connection.

Four E-type thermocouples (5TC-TT-E-36-36; Omega, Stamford, CT) were used to measure the temperature distribution along the gradient plate. Thermocouples were taped to the surface of the gradient plate, within 5 mm of the capillary. Being placed within this proximity of the capillary meant that the thermocouples were not under the insulation but exposed to the room atmosphere. This was done to get a better estimation of the actual temperature being achieved at the capillary since convection and radiation from the capillary could be not be fully impeded. An HP34970 data acquisition system was used to convert thermocouple voltages to temperatures. These measurements were recorded manually during the experiments.

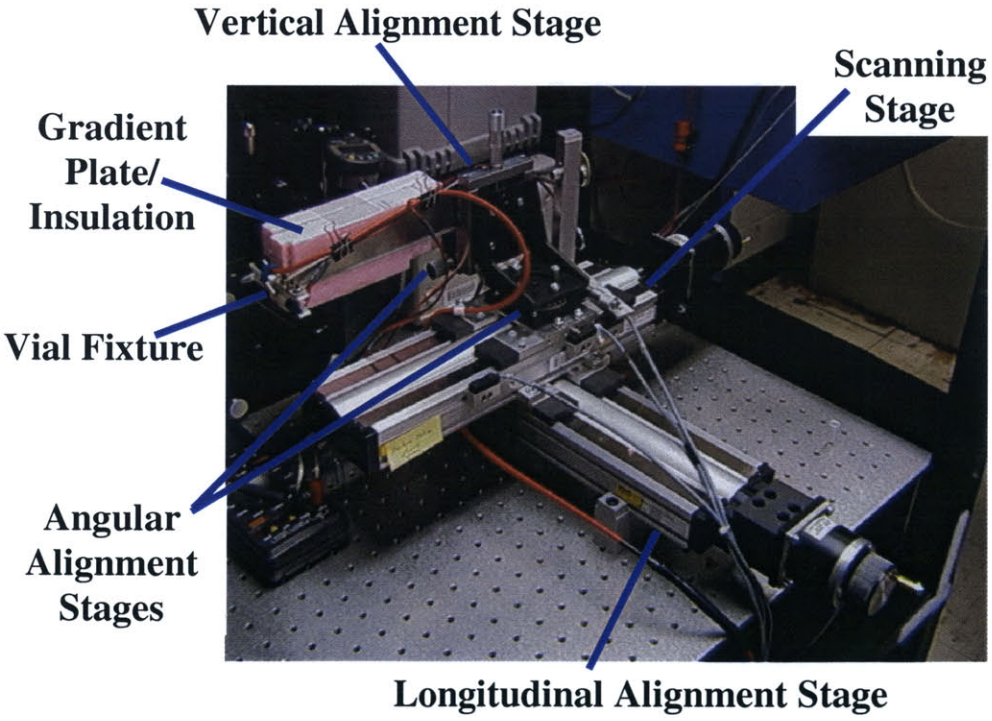

Figure 5-10. Scanning system components.

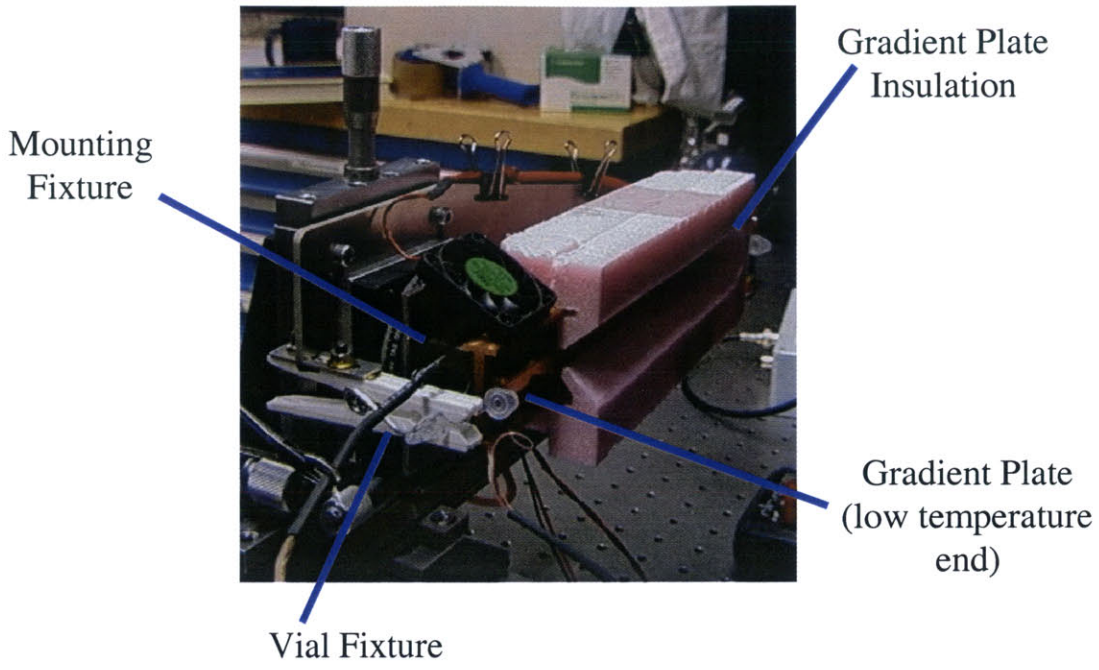

Figure 5-11. Gradient plate system in greater detail.

5.4 Electrical System

Two HP3632A DC power supplies were employed in this setup. One was dedicated to powering the photo-sensor module (± 15 V), providing the photo-sensor gain voltage (± 1 V), and powering the low pass filter (± 15 V). Another power supply was used to power the Peltier-effect thermoelectrics.

Another power supply critical to the instrument, was the CZE1000R high voltage power supply (Spellman, Hauppauge, New York). This provided the voltage across the gel for electrophoresis.

Many components in the system required 120 V AC power. These included both power supplies, the high voltage power supply, the laser, the computer, the motor controller, and the data acquisition unit used to monitor temperature.

The system was originally configured by Graham to be largely under computer control. This meant that all the systems in the previous paragraph except the laser could be adjusted from

commands sent by the PC. This bouquet of connections to the PC resulted in a network of ground loops which generated electromagnetic noise in the system. To reduce this problem, the system was simplified. The photo-sensor module, filter, power supply, and computer necessarily formed a common circuit. AC power to these systems was routed through an isolation transformer. All other electrical components were on a separate circuit. A significant reduction in noise on the measured signal resulted from this re-wiring.

In testing to minimize noise, it was determined that the electrical noise that remained in the system originated primarily from the PC. This noise had an amplitude of approximately ± 25 mV. Tests showed that using a laptop with a National Instruments data acquisition board produced lower noise. However since ± 25 mV of noise could be tolerated in the measurement, further study was not undertaken, and the PC continued to be employed for use.

Chapter 6
Fundamentals of Capillary Electrophoresis

In this chapter the biochemistry involved in capillary electrophoresis is reviewed. Specifically, these topics include fluorescent labeling of the DNA molecules, polymer coating of capillary, the polymer sieving matrix, the dynamics of electro-kinetic injection, and the principles of electrophoretic migration. Concurrently, the application of these concepts to TGCE is discussed.

6.1 Electrophoresis

Electrophoresis, in general, is the movement of a charged particle in an electric field. It is a common and very important tool in the study of DNA, being a major component of the sequencing process and several mutational analysis methods.

The most common type of electrophoresis used in the study of DNA is polyacrylamide gel electrophoresis (PAGE). It is performed by placing a small aliquot of DNA solution in contact with a column of gel. This column may be in the form of a thick sheet (slab gel electrophoresis) or the bore of a capillary (capillary electrophoresis) [46]. A potential is placed across the column to create the electric field. The net negative charge on the DNA creates a

force on the molecule in the direction of the positive terminal. As the DNA moves through the gel column, it encounters the frictional force of the viscosity of water and that created by the porous structure of the gel through which the long strands of DNA must move. The limitation of mobility depends upon the DNA molecule's size and shape. Longer DNA molecules are delayed by the complexity of finding a path through the porus structure [28]. For a constant electric field, migration velocity of the DNA will be constant and is a function of the charge to mass ratio of the molecule.

Capillary electrophoresis has been shown to hold several advantages over slab gel electrophoresis. The most significant advantage of the capillary format is the improved heat dissipation. When the electric field is applied, ohmic heating takes place within the gel. This heating can cause degradation of the polymer (altering its viscosity), create hot-spots which damage the DNA, and generally cause irreproducibility in experiments. The surface to volume ratio of capillary electrophoresis is much greater than the slab gel format. The larger ratio in the capillary format promotes effective heat dissipation from the gel. This, in turn, allows higher electric potentials to be used in capillary experiments. The time required to complete an electrophoretic analysis is inversely proportional to the electric field strength (within limits). Additional benefits include on-column detection, and the potential for full automation of the analysis. Capillary electrophoresis also eliminates the pouring of gels, a cumbersome and time consuming process [12].

6.2 Sieving Matrix

Type, composition, and quality of sieving materials greatly effect the performance of DNA electrophoresis. In the past, both cross-linked and non-cross-linked polymers have been studied. The use of cross-linked gels in capillary electrophoresis is now uncommon due to

difficulties with preparation, operation, and shelf life. Non-cross-linked gels eliminate these problems and offer the additional important feature of being replaceable after each run. As such, replaceable non-cross-linked linear polyacrylamide (LPA), introduced by Karger et al. in 1990 [16] has become one of the most widely employed separation media in DNA analysis [43].

For application to TGCE, a replaceable, high molecular mass, linear polyacrylamide gel was utilized. This polymer was kindly provided by Professor Karger's research group at Northeastern University. The polymer, delivered in the form of a powder, was created by reverse emulsion polymerization. It was well suited for this application given its high molecular mass (good separation qualities), low viscosity (promoted easy replacement of gel in capillary), and long shelf life. The powder was diluted to 8.5% w/w stock solution and refrigerated between use.

6.3 Capillary Coating

The inner wall of the capillary is commonly coated with a layer of polymeric material to eliminate absorption and prevent electroosmotic flow. Coated capillaries are typically necessary for analyses in which the resolution demands are high, especially in DNA analysis [23].

Macromolecular substances such as proteins often show greater tendencies to absorb to any surface than do low-molecular-weight compounds. This is due to the larger number of binding sites found in macromolecules. However, the problem exists to some extent for charged molecules of any size. Absorption issues can also be amplified in dilute buffers since such buffers often do not efficiently suppress the electrostatic interactions between the solute and glass wall [17].

Electroosmosis is caused by the presence of fixed charges on the capillary wall. Because fused silica contains free silano groups that will be ionized when exposed to the buffer, the inside

surface of the capillary will be negatively charged. The adjacent layer of positive ions in the solution will move upon application of the electric field dragging the liquid inside the capillary towards the negative electrode [23]. This movement does not necessarily cause distortion of the migrating DNA bands but does affect the band's rate of migration. Such an effect can lead to run-to-run irreproducibility of results.

Further complications can exist if the charged wall of the capillary is non-uniformly neutralized by ions from the solution. This leads to a non-uniform charge distribution, which, in turn, will give non-uniform migration velocities. Variations in migration velocity in the capillary will lead to distortion of the migrating DNA band [17].

These problems can be minimized by coating the capillary walls to neutralize their charge before injection of the sieving matrix. The approach used for TGCE experiments was taken from Thilly et al. [24]. This approach coats the capillary wall with a monomolecular layer of linear polyacrylamide chains.

6.4 Electro-kinetic injection

There are two main methods of injecting the DNA molecules from the initial stock solution aliquot into the capillary. These include pressure injection and electro-kinetic injection. Pressure injection is relatively uncommon because it is difficult to conduct. This can lead to irreproducible results.

Electro-kinetic injection is a simple procedure. A small quantity of DNA stock solution (usually 5 μL) is brought into contact with the open, gel filled end of the capillary. Voltage is applied briefly, pulling DNA out of the stock solution, into the capillary. For the TGCE experiments, a voltage of 5 kV/m was typically applied for 5 to 30 seconds. Specific details are given for each experiment shown in Chapter 7. The DNA solution in then replaced with a vial

containing only buffer, and the electrophoresis is begun. This process is easily automated, thus it has become the standard for automated capillary electrophoresis.

There are several problems with electro-kinetic injection of which one should be aware such that they may be minimized in an experiment. First, the injection time has to be as short as possible since the injection proceeds straight into the separation column. Excessively long injections lead to long injection plugs (broad peak widths). Second, the method is very sensitive to residual salt in the DNA solution. Even small amounts of salt can lead to severe loss in signal and/or large variations in run-to-run signal strength. Finally, the direct injection into capillaries filled with sieving matrix leads to a discrimination against larger fragments sizes [42].

6.5 Fluorescent labeling

6.5.1 Background

Fluorescent probes enable imaging of DNA molecules with exquisite sensitivity and selectivity. Fluorescence is the result of three-stage process that occurs in certain molecules called fluorophores or fluorescent dyes. The stages involved in the fluorescence process include excitation, excited-state lifetime, and fluorescence emission. The process is depicted by the Jablonski diagram in Figure 6-1. In the first stage, a photon is supplied by an external source such as a laser and absorbed by the fluorophore, creating an excited electronic singlet state (S_1'). In the second stage, the excited state exists for a finite time (typically 1 to 10×10^{-9} s). During this time, the fluorophore undergoes conformational changes and is also subject to a multitude of interactions with its environment. These processes have two important consequences. First, the energy of the excited electronic singlet state (S_1') is partially dissipated, yielding a relaxed singlet excited state (S_1) from which fluorescence emission originates. Second, not all the

molecules initially excited by absorption return to the ground state (S_o) by fluorescence emission. Other processes may depopulate the relaxed singlet state (S_1). The fluorescence quantum yield, which is the ratio of the number of fluorescence photons emitted (Stage 3) to the number of photons absorbed (Stage 1), serves as a measure of the relative extent to which these processes occur. In the third stage, a photon is emitted, returning the fluorophore to its ground state (S_o). Due to energy dissipation during the excited-state lifetime, the energy of this photon is lower. Therefore, the emitted photon has longer wavelength than the excitation photon. The difference in energy is called the Stokes shift.

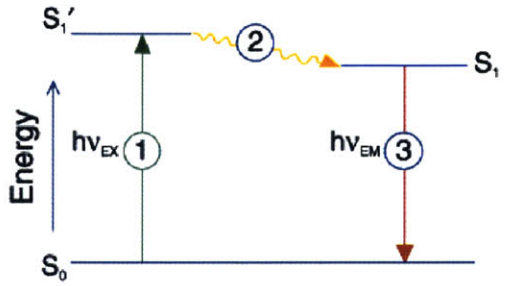

Figure 6-1. Jablonski diagram illustrating fluorescence process [21]

(encircled numbers represent stage labels).

The fluorescence process is cyclical. Unless the fluorophore is destroyed in the excited state, known as photobleaching, the same fluorophore can be repeatedly excited and detected. The relationship between the input photon energy and the output photon energy for polyatomic molecules in solution is described by the excitation/emission spectra rather than the discrete energies hv_{EX} and hv_{EM} shown in Figure 6-1. Examples of these spectra are shown in Figure 6-2, Figure 6-3, and Figure 6-4. Figure 6-2 illustrates that for a single fluorophore in dilute solution, the fluorescence emission spectrum is independent of the excitation wavelength. This is due to the partial dissipation of excitation energy during the excited-state lifetime. The figure shows

emission intensity is proportional to the amplitude of the fluorescence excitation spectrum at the excitation wavelength [21].

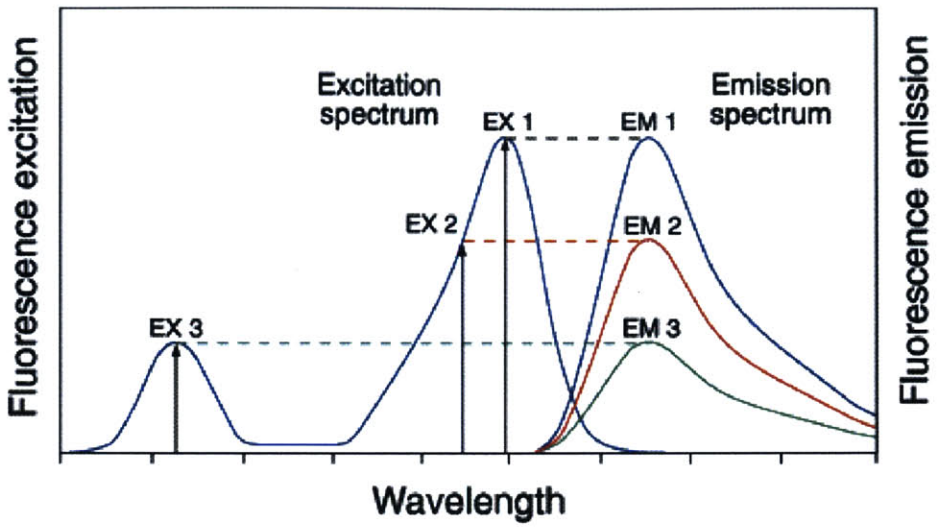

Figure 6-2. Excitation of a fluorophore at three different wavelengths (EX1, EX2, EX3) and the resultant emission (EM1, EM 2, EM3) [21].

6.5.2 End-Labeling Probe

Mutational analysis done by capillary electrophoresis commonly uses a general conjugated end-label to aid in imaging the DNA. An end-labeling probe is a moiety designed to bind covalently to the 5' or 3' end of a DNA molecule. End-labels are used in SSCP, CDCE, and HA. As discussed in Chapter 3, the original concept for this instrument called for the use of two types of fluorescent probes. These include both an end-label moiety and an intercalating dye.

The fluorescent end-label used in TGCE was 5-carboxyfluorescein (FAM). This moiety was attached to the 5' end of primers by the primer supplier, Synthetic Genetics (San Diego, CA). Among the desirable qualities of fluorescein are its relatively high absorptivity, excellent fluorescence quantum yield, and good water solubility. Fluorescein (excitation/emission maxima

~494/520 nm as shown in Figure 6-3) has an excitation maximum that closely matches the 488 nm spectral line of the argon-ion laser, making it the predominant fluorophore for confocal laser scanning microscopy [34].

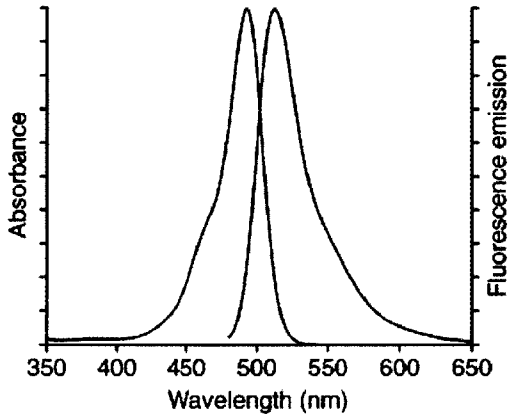

Figure 6-3. Excitation/emission spectra for 5-carboxyfluorescein in 0.1 M NaOH [34].

6.5.3 Intercalating Probe

An intercalating dye attaches itself non-covalently along the DNA strand. Many intercalating molecules can bind with a single DNA chain. This is in contrast to the end-labeling probes in which only a single probe molecule attaches to each end of the chain. Intercalating probes may have molecular bonds with the backbone structure or with the base pairs depending upon the specific intercalator used. In the case of the cyanine dyes considered below, binding patterns vary within these types as well, but all contain bonds which strengthen the connection across the two backbones structures.

6.5.3.1 Selection of YO-PRO-1

The intercalating dye selected for use was a monomeric cyanine nucleic acid stain called oxazole yellow (YO-PRO-1) from Molecular Probes, Inc. Cyanine dyes were desirable because they have a significant fluorescence enhancement upon binding varying between 400× to 1800×.

Consequently the fluorescence of unbound dye is negligible under most experimental detection conditions [33].

There are many cyanine dyes from which to choose. The selection of YO-PRO-1 was based upon it excitation/emission spectra and trade-offs between binding affinity and quantum yield. The excitation/emission spectra of YO-PRO-1 and its homodimer, YOYO-1, made them the primary candidates for this application given the use of the 488 nm Argon Ion laser. Their spectra plots are shown in Figure 6-4.

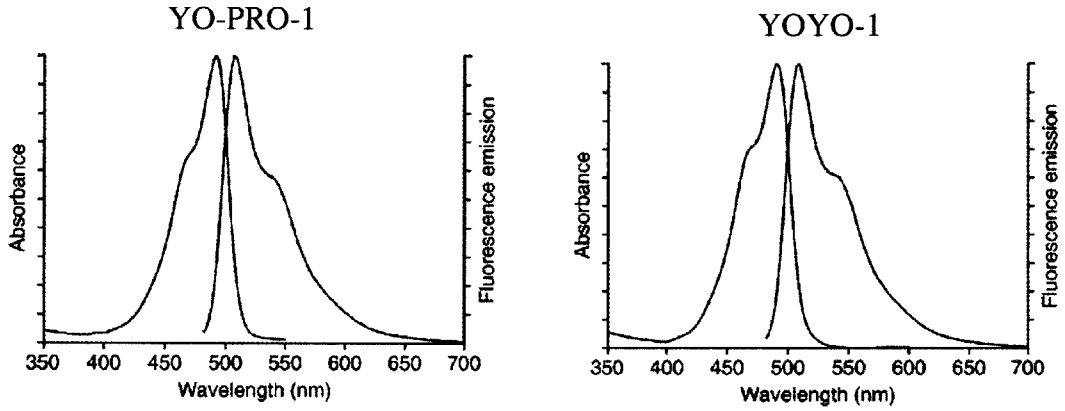

Figure 6-4. Excitation/emission spectra for YO-PRO-1 and YOYO-1.

According to Molecular Probes literature, the quantum yield of the YOYO-1 and YO-PRO-1 dyes are 0.52 and 0.44, respectively [33,35]. A higher quantum yield provides a stronger signal for the optical system to detect. On this basis, YOYO-1, with its higher quantum yield, seems like the candidate of choice. However, YOYO-1 has a binding affinity two orders of magnitude higher than YO-PRO-1 [22]. Binding affinity measures the strength of the bond between the probe and the DNA molecule. An intercalator with a high binding affinity might affect the melting kinetics by inhibiting the transition from duplex to single stranded structures. Therefore, YO-PRO-1 was selected for use in this application.

6.5.3.2 Elimination of Use of Intercalator

The approach taken by Graham [14] in initial phase of the development of this instrument was to first demonstrate the detection of melting via only the change in fluorescence associated with the intercalator. Once this was accomplished, a second phase was planned in which melting would be detected via the change in migration velocity measurable by monitoring the end-labeling probe. However, so many problems were encountered in trying to achieve the first phase, the second phase was never attempted.

There are several significant difficulties with using an intercalator for these experiments. These include problems associated with inhomogeneous binding, compromising of repeatability in electrophoretic migration, inhibition of electro-kinetic injection due to charge neutralization, and problems with background fluorescence.

When the YO-PRO-1 dye is added to a solution containing DNA, the molecules bind. The maximum base pair-to-dye ratio was determined in one study to be 5:1 [31]. If the dye is added to a sufficient concentration, the DNA molecule can be saturated with dye. Saturating the DNA chain with dye is the only way to be sure that all strands are bound to the same number of intercalators. If inhomogeneous binding occurs, strands will have different mobilities during electrophoresis since strands will have differing net charges. These mobility differences cause peak spreading and compromise reproducibility in electrophoresis [31].

When the YO-PRO-1 saturates the DNA, the mass to charge ratio of the DNA molecule is significantly changed. Since electrophoretic injection is critically dependent upon the mass to charge ratio, its effectiveness is significantly compromised. By nearly neutralizing the net charge on the molecule, the injection of the DNA is greatly slowed, and the peak width of the injected sample becomes large. This was demonstrated in experiments by Graham and other studies [14,31,48].

Adding the dye to the gel so that binding does not occur until after the DNA is injected can circumvent injection problems. However, again, sufficient quantities of dye must be added to allow saturation to occur. This means that a non-negligible quantity of dye must be added to the gel. This free dye increases the background noise, reducing the signal to noise ratio. The characteristic large fluorescence enhancement of YO-PRO-1 reduces the level of severity this problem might otherwise present, however its effects can be observed in un-optimized experiments [31].

It is worth noting that intercalators are in somewhat common use for electrophoretic DNA migration analysis. Several papers exist optimizing its use for forensics studies [6,31,32]. In these works, they show that each of these problems can be minimized with appropriate counter measures. For the TGCE application, however, it does not make sense to incorporate the additional steps to minimize (which is not the same as eliminate) errors associated with the intercalator since the intercalator measurement provides redundant information to the end-label probe measurement. The intent of incorporating the redundancy was to make it more robust. Since the use of the intercalator increases the complexity and adds additional sources of error to the measurement, that robustness was not realizable. Therefore, its use was eliminated.

Chapter 7
Experiment Procedure, Results, and Discussion

The goal of experimentation was to prove that the instrument could successfully and efficiently separate the mutant and wild type alleles. In this chapter, experimental conditions and results are presented which demonstrate the successful discrimination of mixed samples.

7.1 DNA Sample Preparation

The wild type DNA fragment used for these experiments was a 275 base pair fragment corresponding to base pairs 2228 to 2503 of the human SRY gene combined with a 30 base pair GC clamp and 75 base pairs of plasmid sequence. The same fragment with a single base T->G mutation at base pair 2283 served as the mutated sequence. The full sequence is given in Figure 7-1. Template and considerable assistance in conducting the polymerase chain reaction (PCR) amplification was kindly provided by Dr. Cathy Hogan and was greatly appreciated.

Primers were purchased from Synthetic Genetics. The 5' primer was 5'-ACG TTG TAA AAC GAC GGC with a 5' fluorescein label. The 3' primer, 5'-GCC GTC GTT TTA CAA, was not labeled.

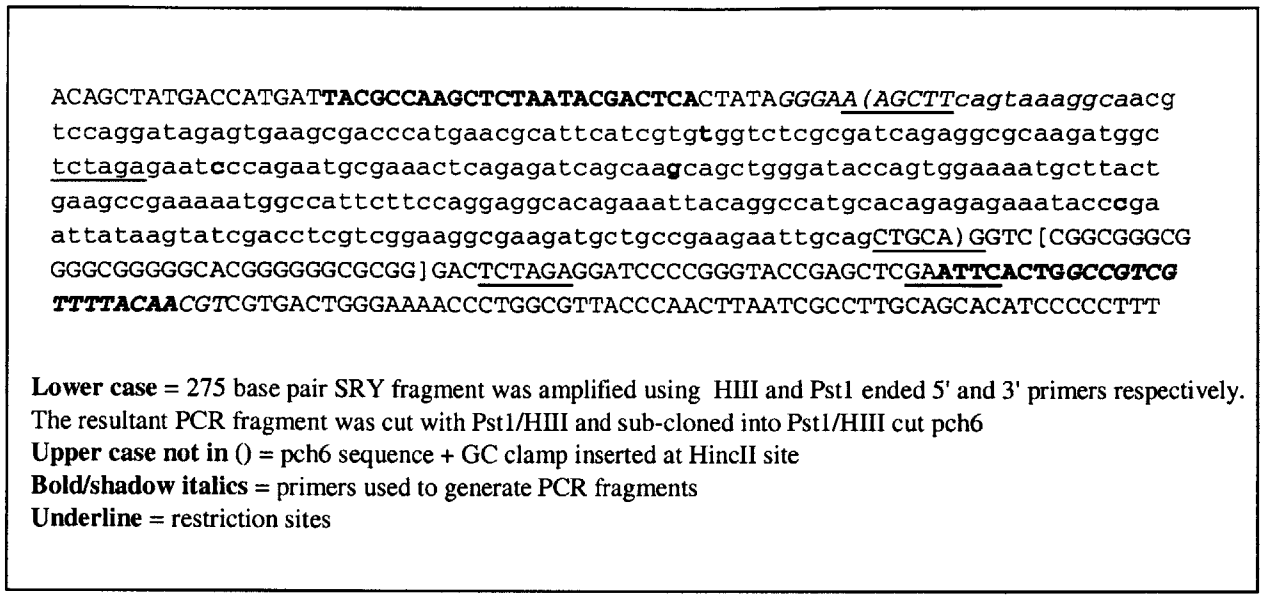

Figure 7-1. DNA fragment used in experiments.

7.2 Experiment Procedure

The first step in the experiment was the preparation of capillaries (75 μm inner diameter, Polymicro Technologies, Phoenix, AZ). Typically eight capillaries were prepared at once. Sections were first cut to lengths of 280 mm. These were then immersed in hot hydrochloric acid until the polyimide coating was removed from the entire length of each capillary. The exteriors were subsequently thoroughly rinsed with Millipore water. A short length (~ 30 mm) of Teflon tubing was attached to one end of the capillary. The tubing (Upchurch Scientific) had an inner diameter of 254 μm and an outer diameter of 1.588 mm. The tubing was attached simply by heating under a heat gun and sliding on to the capillary. Needles were used to flare the Teflon tube to make it easier to slide on to the capillary. Hamilton Gastight® Syringes (81030, 100 μL) were used in conjunction with the Hamilton 80458 needle to inject all solutions and the gel into the capillaries. As described in Chapter 6, the inner surface of the capillary was coated with a linear polymer and was allowed to polymerize for at least 8 hours.

The inner surface of the capillary that was to be mounted in the instrument to enable alignment was left untreated. This tube was filled with 100 mM fluorescein solution.

On the day of an experiment, a capillary was flushed with Tris-TAPS-EDTA buffer and then injected with 8.5% w/w linear polyacrylamide gel. This gel was also described in Chapter 6. Special care was taken to produce a little bulb of gel protruding from each end of the capillary to create good electrical contact between gel and buffer during electrophoresis. Air pockets at the ends of the capillary had a deleterious effect on electrophoretic conditions. These pockets could be observed under a microscope, or detected by monitoring pre-electrophoresis current.

Immediately before injecting the gel, the exterior of the capillary was cleaned with acetone and Millipore water using lens paper. Any dust particles or gel excess on the imaged region of the capillary surface would be measured as spikes in the data.

The fluorescein capillary was carefully removed so as not to disturb alignment and the gel-filled capillary was installed. Installation consisted of inserting the capillary into the gradient plate groove and securing it with Kapton tape at locations just beyond the scannable region.

The ends of the capillary were inserted into 0.5 mL PCR tubes filled with the Tris-TAPS-EDTA buffer. Platinum electrodes were likewise immersed in the buffer solutions. The gel was pre-electrophoresed at 4200 V (15 kV/m) for ~15 minutes before it was used in any experiment. An ammeter in the high voltage circuit was used to read current during experiments. Typically, current would initially be greater than 8 μA then trail off to less than 7.5 μA after 10 min.

The thermal gradient was activated at the beginning of pre-electrophoresis to allow the system to move toward steady state before the DNA was injected into the capillary. Since temperatures were controlled only by open loop DC power supplies adjusted by the experimenter, reaching steady state often took between 15 to 20 minutes. Faster times could be achieved in the future by implementing a closed loop temperature controller.

Once pre-electrophoresis was completed, the DNA sample was electro-injected. The experiments presented in this chapter all used the same volume and concentration of DNA however no optimization was done. Other experiments, not presented, used different quantities of DNA. Based on these earlier experiments, 5×10^{10} molecules in each resolved peak were used in the experiments presented. From results given by Khrapko [25], it was assumed that 10 percent of the DNA in a 5 μL volume would be electro-injected using a injection current of 1 μA for 30 s. Based on this, 5×10^{11} molecules per peak needed to be in the injection solution. Since heteroduplex analysis was to be used (4 resulting combinations and/or potential peaks), that meant 1×10^{12} molecules of each sample, wild type and mutant, were needed in the injection solution. The wild type and mutant stock solution concentrations that resulted after PCR and purification were measured via ultraviolet absorption. The wild type solution had a concentration of 0.184 μg/μL while the mutant solution had a concentration of 0.177 μg/μL. Given the approximation that 10^{10} molecules that are 100 base pairs in length have a mass of 1 ng, the volumes needed from each stock solution are given by

$$10^{12}\,molecules \cdot 392bp \cdot \frac{1ng}{100bp \cdot 10^{10}\,molecules} \cdot \frac{1}{184ng/uL} = 2.1uL \tag{7-1}$$

for the wild type solution and

$$10^{12}\,molecules \cdot 392bp \cdot \frac{1ng}{100bp \cdot 10^{10}\,molecules} \cdot \frac{1}{177ng/uL} = 2.2uL \tag{7-2}$$

for the mutant solution.

Therefore, volumes of 2.1 μL of the wild type, 2.2 μL of the mutant sequence, and 0.7 μL of Tris-TAPS-EDTA buffer were mixed in PCR tubes. These injection solutions were thermocycled. Denaturization took place at 95 °C for 2 minutes. The ssDNA was then annealed

for 2 hours at 40 °C to create homo- and heteroduplexes. Electro-injection was conducted from these 5 μL volumes at 1 μA for 30 s for each experiment.

After the DNA was injected, the buffer vial replaced the sample vial and electrophoresis was ready to begin. Electrophoresis settings varied slightly for each experiment and will therefore be described for each figure.

Data was collected at 400 Hz during each experiment while a 100 mm region was continuously scanned. Scanning speed was 50 mm/s for the first two experiments presented but was increased to 100 mm/s for the last experiment. This is also reflected in the figure titles.

7.3 Thermal Gradient Measurement

Temperatures measured at four positions, spaced 40 mm apart and spanning the scanned region, were recorded manually at various times during the experiment. Temperature measurement was transduced as described in Chapter 5. Following the experiment, a theoretical model of the temperature gradient, Equation (4-11), were fitted to the measured temperatures. The model was fit to the measurements using the same Marquardt non-linear minimization method described in Appendix B. These optimized coefficients were then used to generate the non-linear temperature scale that labels the left-hand y-axis of each figure.

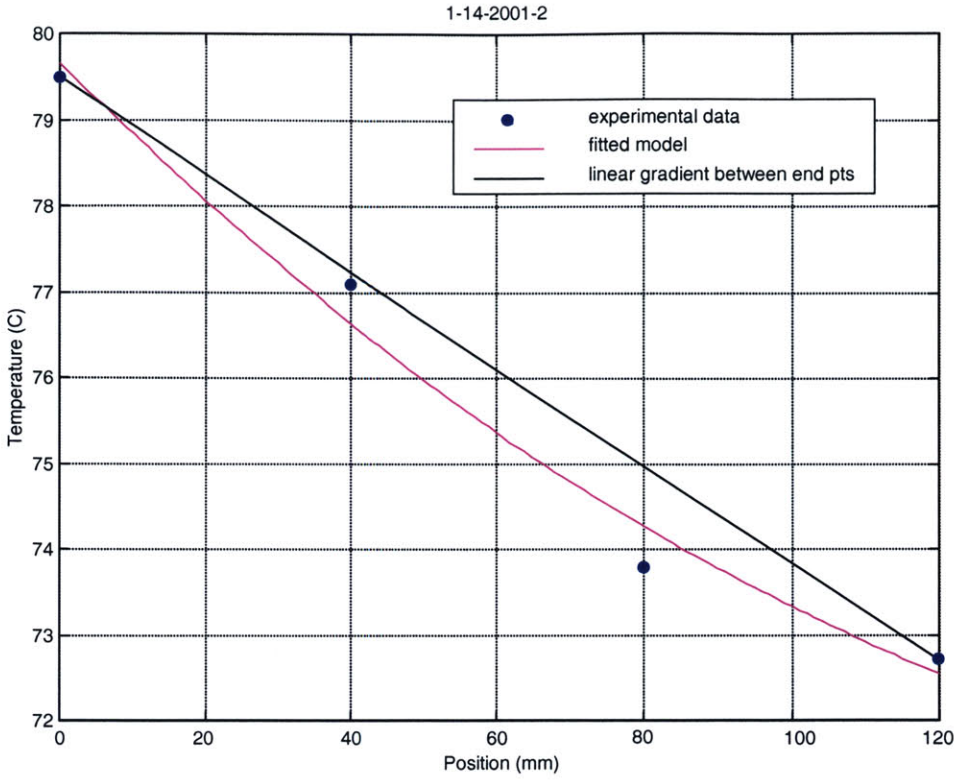

Figure 7-2. Temperature distribution for experiment 1-14-2001_2.

Figure 7-2 compares the fitted model to measured temperatures for experiment 1-14-2001_2. While the experimental data showed good repeatability of the measured pattern through various experiments, measurements show a deviation of nearly 0.75 °C from the model at some positions. This problem is the result of several factors. The largest source of measurement error is mostly likely due to differences in thermocouple mounting. Thermocouples were taped to the surface of the gradient plate. It is possible that a small air gap is present between the plate and some sensors. Variations in the amount of tape used to attach them might also provide error by insulating the sensor. Finally, sensors were not mounted at exactly the same level with respect to the edge of the insulation. Since the capillary must have no insulation over it to allow it to be imaged, there must exist a thermal gradient symmetric about the capillary in the vertical plane. The vertical position of the thermocouple would therefore effect the measured value. Inaccurate

thermocouple calibration and limited resolution of the thermocouples may have also made small contributions to the deviation from the expected measurement. The straight, solid black line in Figure 7-2 represents an ideal, perfectly linear gradient. The analysis in Chapter 4 indicated that a deviation of 0.1 °C from perfectly linear would be expected if the plate were fully covered with insulation (i.e. if the section of insulation to make the capillary visible did not have to be removed). The actual difference between the fitted model and perfect linearity is observed to be close to 1 °C.

As stated earlier, the thermal gradient was controlled open loop. As such, stability problems with the gradient were encountered. Variations during experiments of 0.3 °C measured at the outer two sensors were observed.

7.4 Results

The results of three experiments are shown in Figure 7-3, 7-4, 7-5. Experimental parameters employed are given in the figure labels.

Each figure represents the compilation of many scans taken over the length of the capillary through time. The color shade is proportional to measured intensity where red is the highest intensity and blue the lowest intensity. To interpret the results, observe in Figure 7-3 that at time = 0, a scan is made down the length of the capillary. The DNA has not migrated into the scannable region yet, therefore at all positions for time = 0, the plot is blue. Again in Figure 7-3, observe that at time = 8 minutes, a bright region occurs at position = 0. This is the DNA entering the scannable region. As time progresses, the bright region is observed to move farther down the capillary. At some position (temperature) and time, the high intensity peak splits into two peaks. This represents the melting of the first heteroduplex sample.

All three figures were generated in Matlab. The code used to generate them is included in Appendix A. The procedure was as follows. The data matrix was first trimmed. Trimming was required because data was still being collected briefly at the end of each scan after the system had stopped moving. The next step was to remove the background. Consistent noise spikes were recorded during each scan from various dust contaminants or surface irregularities. This noise could be removed from the data by subtracting the values from the first scan from all subsequent scans. Next, maximum and minimum values were imposed on the data matrix. Since z-axis values are expanded to fit over the blue to red color range, noise spikes in either the positive or negative direction can sharply decrease the contrast of the results; setting limits resolved that problem. The final step in signal processing was to apply Matlab's matrix median filter, medfilt2, to the image. Applying all these steps could extract the peak migration from data in which it was otherwise not observable.

Figure 7-3 shows the results of experiment 1-14-2001_2 conducted over a temperature range from 73.4 °C to 79.6 °C. The initial velocity of the peaks migrating together is approximately 0.24 mm/sec. The first heteroduplex branch occurs at 76.35 °C. The second heteroduplex branch appears at 76.8 °C. Finally, the mutant and wild type homoduplexes melt at 77 °C. After melting, all separated peaks migrate at approximately 0.037 mm/sec. This represents an 85% reduction in migration velocity. Significant band broadening occurs at higher temperatures such that the peaks can no longer be discriminated after 20 minutes. This is likely due to the complete dissociation of the molecules (including the dissociation of the GC clamp).

In order to improve the resolution of the melting events, the temperature range was reduced for the 1-14-2001_3 experiment running from 73.3 °C to 79.7 °C. These results are shown in Figure 7-4. The temperature dependence of the duplex molecules is now more evident as it is observed to increase as it migrates. At about 12 minutes the velocity is similar to that

from the first experiment, 0.23 mm/sec. Note that this lower velocity is likely a function of the slightly lower electrophoretic current in this experiment as compared to the first. This time, the first heteroduplex branch separates at 75.8 °C. The second heteroduplex branches off at 76.5 °C. The homoduplex molecules finally melt at 77.4 °C.

It is interesting to note that the velocity changes exhibited by the heteroduplexes when they branch off do not appear to indicate complete melting. The expected, sharp 'knee' in the velocity profile is replace by a more smoothly departing branch. The subsequent increasing and decreasing velocity of the heteroduplexes, evidenced by the 'wiggles' in their migration paths, indicate that instabilities existed in the thermal gradient. As discussed previously, the open loop temperature control allowed undesirable fluctuations in the thermal gradient temperatures. Many of the features shown in this plot are believed to be artifacts of that temperature fluctuation. Finally, each of the branches, upon reaching the position correlated with 77.4 °C, exhibit a very similar migration velocity of approximately 0.07 mm/sec.

In the final experiment, 1-14-2001_4, the temperature range was tightened still further, running from 75.2 °C to 78.8 °C. In the production of Figure 7-5, the median filter that was applied to the other figures was omitted. Important detail was blurred by the use of the filter in this case. The un-melted molecules initially migrate at ~0.22 mm/sec. This is in good agreement with both previous experiments. Three branches are observable. The first heteroduplex branches off at 77.94 °C. The second heteroduplex branch separates at 78.06 °C. Finally, the mutant and wild type homoduplexes melt at 78.44 °C. Each melted branch exhibits a migration velocity of approximately 0.028 mm/sec.

The results from each experiment are summarized in Table 7-1. Note that all values for velocity and temperature given in the table and in the discussion were derived manually from the

graphic results and as such are approximate. This results demonstrate the problems that exist in the instrument regarding reproducibility of the melting temperature.

Table 7-1. Observed Results from Each Experiment

Experiment	Initial Velocity	Heteroduplex 1		Heteroduplex 2		Homoduplexes	
	(mm/sec)	**velocity** (mm/s)	**melting temp.** (°C)	**velocity** (mm/s)	**melting temp.** (°C)	**velocity** (mm/s)	**melting temp.** (°C)
1-14-2001_2	0.24	0.037	76.35	0.037	76.80	0.037	77.0
1-14-2001_3	0.23	0.070*	75.75	0.070*	76.45	0.070*	77.4
1-14-2001_4	0.22	0.028	77.94	0.028	78.06	0.028	78.44

*final velocity after melting

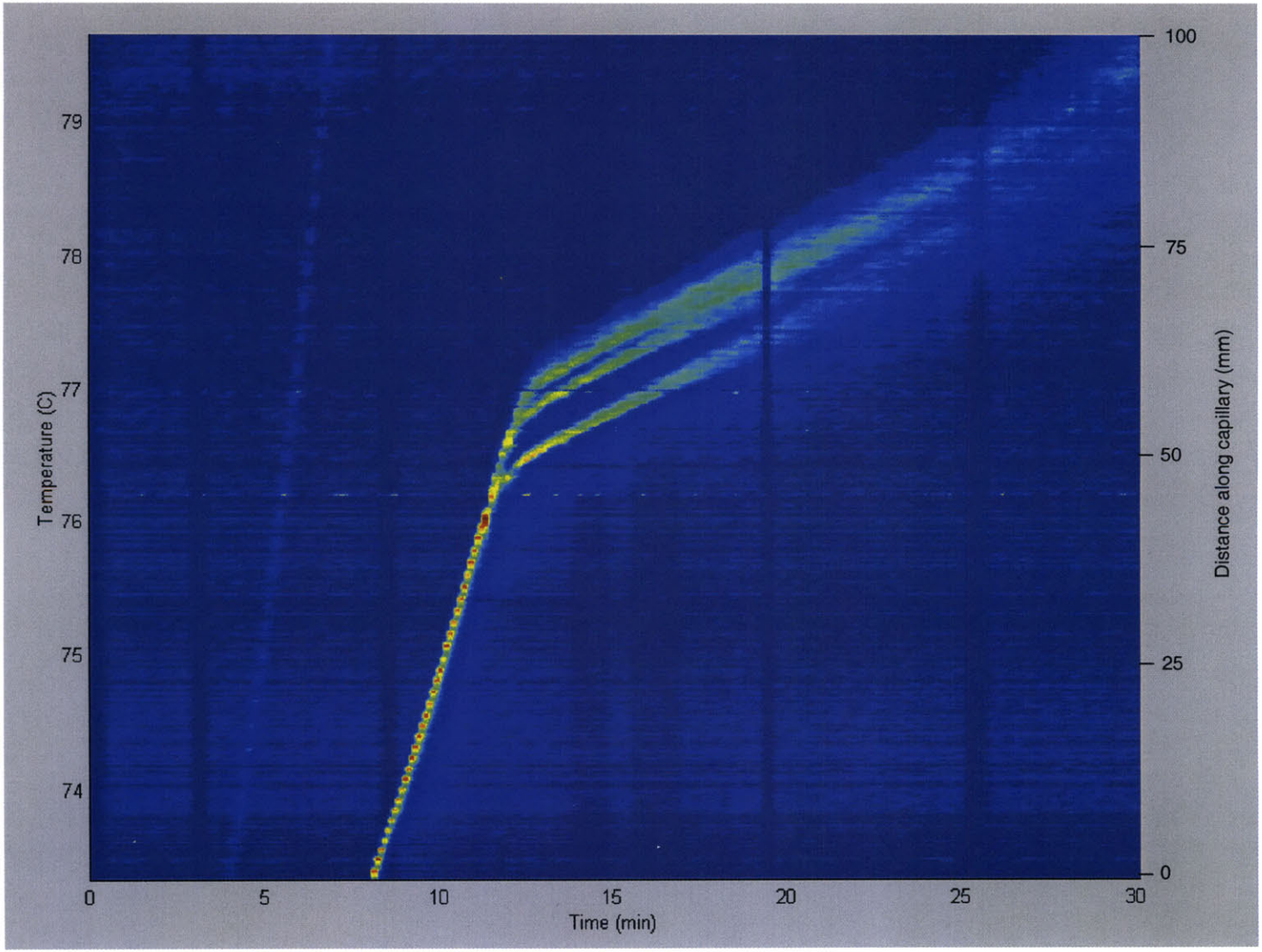

Figure 7-3. Experiment 1-14-2000_2; electrophoresed at 4500 V (13 μA), PMT gain = 0.39 V, data acquired at 400 Hz, scanning velocity = 50 mm/s.

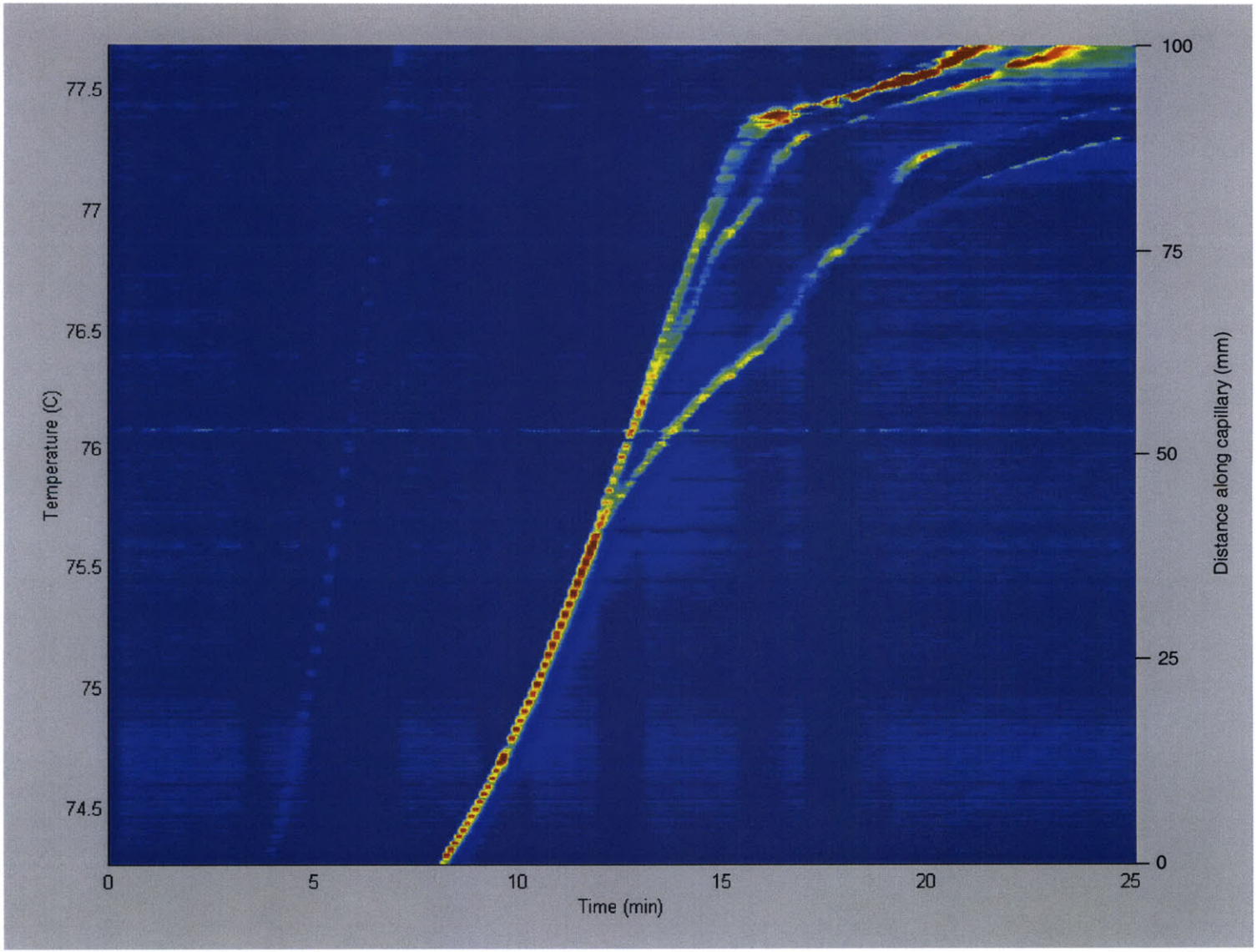

Figure 7-4. Experiment 1-14-2000_3; electrophoresed at 4500 V (12.7 μA), PMT gain = 0.39 V, data acquired at 400 Hz, scanning velocity = 50 mm/s.

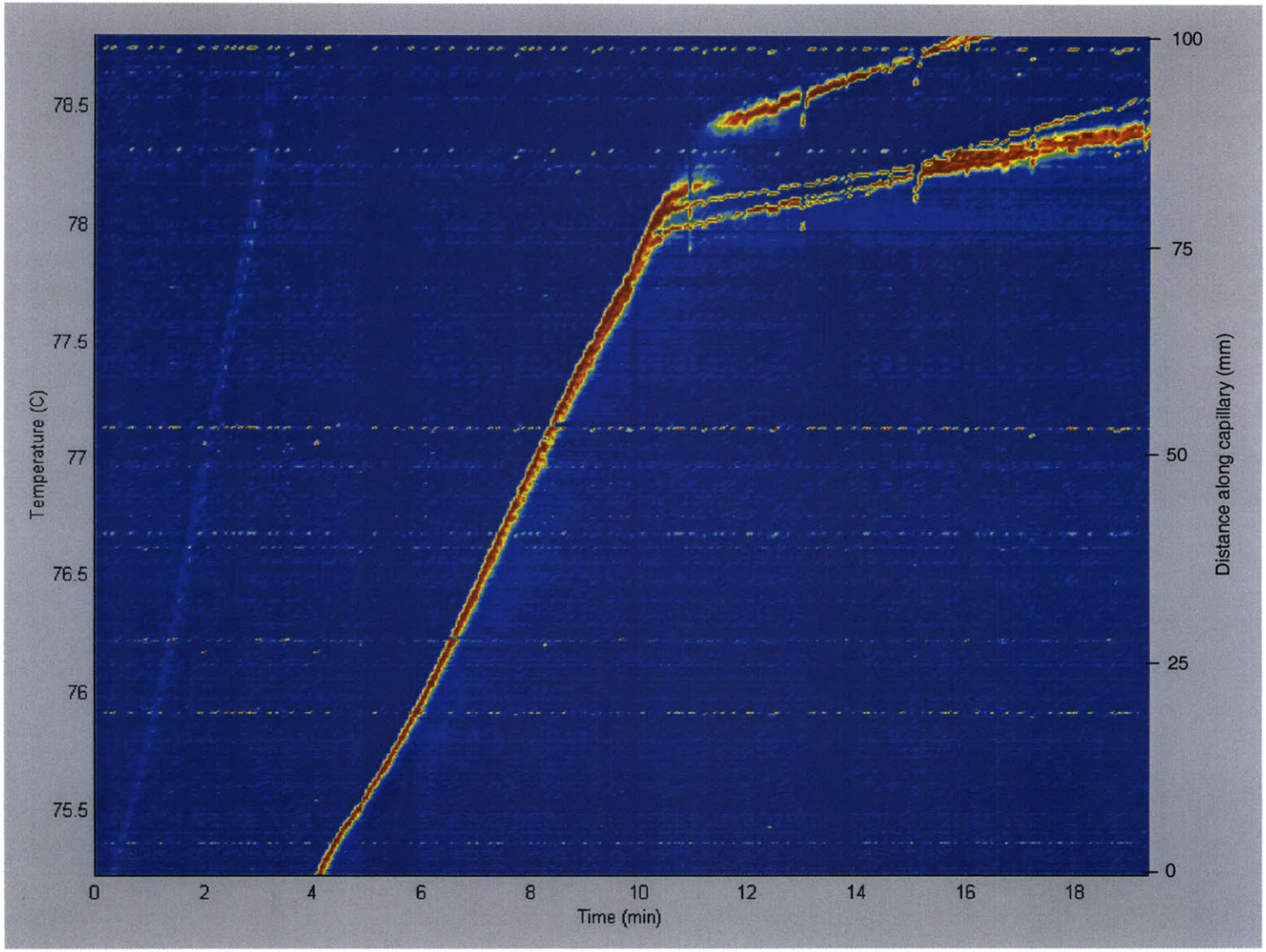

Figure 7-5. Experiment 1-14-2000_4; electrophoresed at 5000 V (14 μA), PMT gain = 0.39 V, data acquired at 400 Hz, scanning velocity = 50 mm/s.

Chapter 8 Conclusion

In this thesis, a novel concept for mutation and single nucleotide polymorphism detection has been described. A thorough design process was presented focusing on several key points. These included maintaining optical alignment by controlling thermal expansion and creating a predictable, stable thermal gradient by maximizing the role of conduction in the heat transfer of the system. Optimization of the pinhole radius for the confocal optical system was evaluated along with a careful analysis of the appropriate sampling rate and filter cut-off frequency. The concept and design were shown to be effective through a series of experiments which compared a wild type sequence nearly four hundred base pairs in length against a mutant sequence which differed from the wild type by a single point mutation. The presence of the mutation was successfully measured as the results clearly showed heteroduplexes melting at a lower temperature than homoduplexes.

8.1 Future Work

While this work has yielded successful results, there are many things to improve before this instrument reaches its full potential. Among issues most important to be addressed are temperature control, gel injection, optical alignment, and scale-up.

8.1.1 Temperature Control

As noted in the Chapter 7, temperature control in this instrument was controlled open loop. This led to variations in the temperature of ±0.3 °C. Closed loop control is sorely needed. Note, however, that this system is a multi-input, multi-output system (MIMO) consisting of at least two inputs and two outputs.

8.1.2 Gel Injection

In the present set-up, the capillary must be removed from the gradient plate in order to inject new gel. The original intent was to be able to inject fresh gel without removing it, however the difficulty involved in coupling the syringe to the capillary, the steady, slow pressure required to inject the gel, and the brittleness of the capillary with removed coating, all conspire to make this unachievable. When attempted, the capillary usually broke.

Several solutions are possible. A new arrangement for the capillary mount could be designed so that it provide more robust support for the task. Another means would be to develop a more integrated system in which the capillaries were replaced by micro-channels in a silicon chip. Such devices have been developed and tested by Matsudaira for sequencing [42].

8.1.3 Optical Alignment

The optical alignment system used in this instrument was marginally acceptable. Extreme care was required in the experiments not to disturb the gradient plate from optical alignment. Further, the process of re-aligning the instrument was cumbersome and slow. A more robust design is needed.

One solution that can be imagined is again based upon the integrated micro-channel approach. By having a dedicated micro-channel in the horizontal and vertical directions that

could be filled with fluorescein, one could conduct the alignment process more efficiently without the need to swap capillaries after the plate was aligned.

8.1.4 Scale-up

In order to meet the goals of fast analysis, several changes are necessary. First, the dead space in the capillary must be minimized. This includes the length from the injection end to the beginning of the imaged region of the capillary. This can be minimized by redesigning the "low side" temperature control unit. The use of the Peltier-effect thermoelectric provided constraints on the dead space that could be avoided with an alternate configuration or heat source.

Second, tests should be conducted to determine how many analyses can be effectively carried out in a single capillary. In the experiments presented in this thesis, one test sequence was compared against a known wild type. It may be possible to do multiple comparisons in the same tube in which test samples from several patients labeled with different probes are run simultaneously.

Finally, the instrument could be redesigned to incorporate multiple capillaries in parallel. This could also be done with the micro-channels in a silicon chip. With a faster scanning actuator, it seems likely that the photosensor might be effective in scanning up to ten capillaries. However, to increase to more than ten capillaries, a CCD array would have to replace the photosensor. While the CCD array is markedly less sensitive than the photosensor, its use could potentially negate any need to physically move the capillary system for scanning its length. This would significantly simplify the instrument, reduce its cost, and make it easier to optically align.

As an example demonstrating the value of the potential throughput capacity of this instrument, imagine that in an association study a scientist was evaluating 2 disequilibrium regions, 2000 base pairs in length, in 1000 individuals essentially requiring the comparison of

4,000,000 base pairs against the wild type. TGCE, comparing two 500-mer sequences against a wild type in each capillary in experiments which take 15 minutes each to conduct, would complete 96,000 base pairs per capillary in 24 hours. With ten capillaries, this is nearly 1 million base pairs per day. With 100 capillaries, this is nearly 10 million base pairs per day. Thus assuming that all PCR reactions can keep up, the 4,000,000 base pairs could be completed in a period of 1 to 5 days depending on the number of capillaries in the system.

Appendix A Matlab Code to Plot Results

Included in this appendix are the three m-files used in Matlab to generate the plots found in Chapter 7.

A.1 Code to create Figure 7-2

```
%This program plots 1-14-2000_2.txt.  Load it
%with datafix2 before calling this program.

%data matrix b must be loaded from datafix2.m
%before running the program.

b2=b(:,20:840);

%subtract background
imax=length(b2(:,1));

for i = 1:imax
   b3(i,:)=b2(i,:)-b2(1,:);
end

%set maximum value from data
max=0.35
c=length(b3(1,:));

r=length(b3(:,1));

for i=1 :c
   for n = 1:r
      if b3(n,i)>max;
         b3(n,i)=max;
      end
   end
end

%set minimum value in data
minimum=0.00
for i=1 :c
   for n = 1:r
      if b3(n,i)<minimum;
         b3(n,i)=minimum;
      end
   end
end
```

```
%digital filter
b4=medfilt2(b3);

%b4=b4(140:180,500:700);
scantime=3; %seconds
distance = 100; %mm

time=0:(scantime*2):(scantime*2)*length(b4(:,1))-1;
time=time/60;
distance = 0:distance/(length(b4(1,:))-1):distance;

%In order to generate temperature vector, use model.
%Model parameters optimized with Marquardt Minimization
   %Ambient Temperature
      Tinf = 25;
   %input parameters resulting from Marquardt
      C1=42.2161;
      C2=12.4361;
      m=-2.8200;
   %input the model
      x=distance/1000;
      temp=C1*exp(m*x)+C2*exp(-m*x)+Tinf;
      for i=1:length(temp)
         temperatures(i)=temp((length(temp))-i+1);
      end

surf(time,temperatures,b4'); shading interp; view(0,90); axis tight;

ylabel('Temperature (C)');
xlabel('Time (min)')
%title('DNA migration through Spatial Thermal Gradient')
```

A.2 Code to create Figure 7-3

```
%This program plots 1-14-2000_3.txt.  Load it
%with datafix2 before calling this program.

b2=b(:,20:840);

%subtract background
imax=length(b2(:,1));

for i = 1:imax
   b3(i,:)=b2(i,:)-b2(1,:);
end

%set maximum value from data
max=0.45

c=length(b3(1,:));

r=length(b3(:,1));

for i=1 :c
```

```
   for n = 1:r
      if b3(n,i)>max;
         b3(n,i)=max;
      end
   end
end

%set minimum value in data
minimum=0.00
for i=1 :c
   for n = 1:r
      if b3(n,i)<minimum;
         b3(n,i)=minimum;
      end
   end
end

%digital filter
%b4=medfilt2(b3);
b4=b3;


%b4=b4(140:180,500:700);
scantime=3; %seconds
distance = 100; %mm

time=0:(scantime*2):(scantime*2)*length(b4(:,1))-1;
time=time/60;
distance = 0:distance/(length(b4(1,:))-1):distance;

%In order to generate temperature vector, use model.
%Model parameters optimized with Marquardt Minimization
   %Ambient Temperature
      Tinf = 25;
   %input parameters resulting from Marquardt
      C1=38.1503;
      C2=15.6781;
      m=-2.7028;
   %input the model
      x=distance/1000;
      temp=C1*exp(m*x)+C2*exp(-m*x)+Tinf;
      for i=1:length(temp)
         temperatures(i)=temp((length(temp))-i+1);
      end

surf(time,temperatures,b4'); shading interp; view(0,90); axis tight;

ylabel('Temperature (C)');
xlabel('Time (min)')
%title('DNA migration through Spatial Thermal Gradient, 1-14-2001_3.txt')
```

A.3 Code to create Figure 7-4

```
%This program plots 1-14-2000_4.txt.  Load it
%with datafix2 before calling this program.
```

```
%data matrix b must be loaded from datafix2.m
%before running the program.

b2=b(:,40:450);

%subtract background
imax=length(b2(:,1));

for i = 1:imax
   b3(i,:)=b2(i,:)-b2(1,:);
end

%set maximum value from data
max=0.4

c=length(b3(1,:));

r=length(b3(:,1));

for i=1 :c
   for n = 1:r
      if b3(n,i)>max;
         b3(n,i)=max;
      end
   end
end

%set minimum value in data
minimum=0.005
for i=1 :c
   for n = 1:r
      if b3(n,i)<minimum;
         b3(n,i)=minimum;
      end
   end
end

%digital filter
b4=medfilt2(b3);

%b4=b4(140:180,500:700);
scantime=2; %seconds
distance = 100; %mm

time=0:(scantime*2):(scantime*2)*length(b4(:,1))-1;
time=time/60;
distance = 0:distance/(length(b4(1,:))-1):distance;

%In order to generate temperature vector, use model.
%Model parameters optimized with Marquardt Minimization
   %Ambient Temperature
      Tinf = 25;
   %input parameters resulting from Marquardt
      C1=36.9410;
      C2=16.8631;
      m=-2.8083;
   %input the model
```

```
        x=distance/1000;
        temp=C1*exp(m*x)+C2*exp(-m*x)+Tinf;
        for i=1:length(temp)
            temperatures(i)=temp((length(temp))-i+1);
        end


surf(time,temperatures,b4'); shading interp; view(0,90); axis tight;

ylabel('Temperature (C)');
xlabel('Time (min)')
%title('DNA migration through Spatial Thermal Gradient')
```

Appendix B Dynamic Tracking

As described in Chapter 3, the TGCE system must track the position of the DNA as it migrates down the capillary. The method of tracking described was simply to scan the capillary over the entire gradient length, over and over. By recording both position and intensity, a plot could subsequently be developed indicating the position of the fluorescent peak for each scan.

The actual width of the peak compared to the length of the scan is small. Typically, the scan width was 100 mm while the peak width of the migrating band would be no more than 5 mm (See results in Chapter 7). Therefore, only 5% of the time involved in each scan was actually used to image the DNA.

Dynamic tracking of the DNA peak was developed as a method of maximize the time spent recording relevant information. This method uses a highly non-linear feedback loop to control the motor scanning. A much shorter scan width could then be used to image the DNA's progress. As the DNA band migrated down the length of gradient, the center of the scan width moved with it.

In this chapter, the software developed for dynamic tracking is described. The software consisted of three basic parts: initialization, detection of the DNA band moving into imaging region, and peak tracking.

B.1 Initialization

This component of the code initialized variables and all hardware devices involved in dynamic tracking. This included the Allios data acquisition board (described in Chapter 5), the Zeta motor controller (described in Chapter 5), and the PCI-6601 Counter/Timer Board (National Instruments, Austin, TX). This board was used to read the step count from an linear encoder mounted on the scanning stage.

B.2 Detecting of Peak Entrance to Scanning Region

Tracking the peak cannot logically begin until the DNA is within the image-able region of the capillary. The image-able region begins approximately 100 mm from the low temperature end of the capillary. The first 100 mm cannot be imaged since this portion is not in the section of the plate which maintains a nearly linear thermal gradient. Images and diagrams of the gradient plate and capillary can be found in Chapter 4.

The tracking software is designed to wait, imaging a static position, until the migrating peak passes. A robust discrimination between variable noise and the passage of the actual peak was important. To make the peak detection more robust, its passage was detected in three steps.

First, the algorithm monitored the signal for a consistent rise in intensity. If a short running mean of the intensity increased more than a set amount over a set period of time, a Boolean variable was triggered which allowed the next criterion to be evaluated.

The second event monitored was the detection of a maximum in the signal. In this case, as the short running mean began to decrease in value, a second Boolean variable became true which advanced the peak detection to the final criterion.

The third criterion was the detection of a consistent decline in the intensity. Similar to the first criterion, If a short running mean of the intensity decreased more than a set amount over

a set period of time, a Boolean variable was triggered. The Boolean variable signaled that the peak had passed the detector. Tracking then began immediately.

Note that the rate of change of the intensity in criterion one and three was set to be six times as high as that in criterion two. This detail was characteristic of the shape of the Gaussian intensity profile.

B.3 Tracking the Peak

Once the peak has entered the scanning region, the system must track its migration down the gradient. The means by which this was achieved is described by the block diagram in Figure B-1. The open loop control described in Chapter 3 consisted of only the Motor Move command block, the Scan Data Recording block, and the Permanent Data Record block.

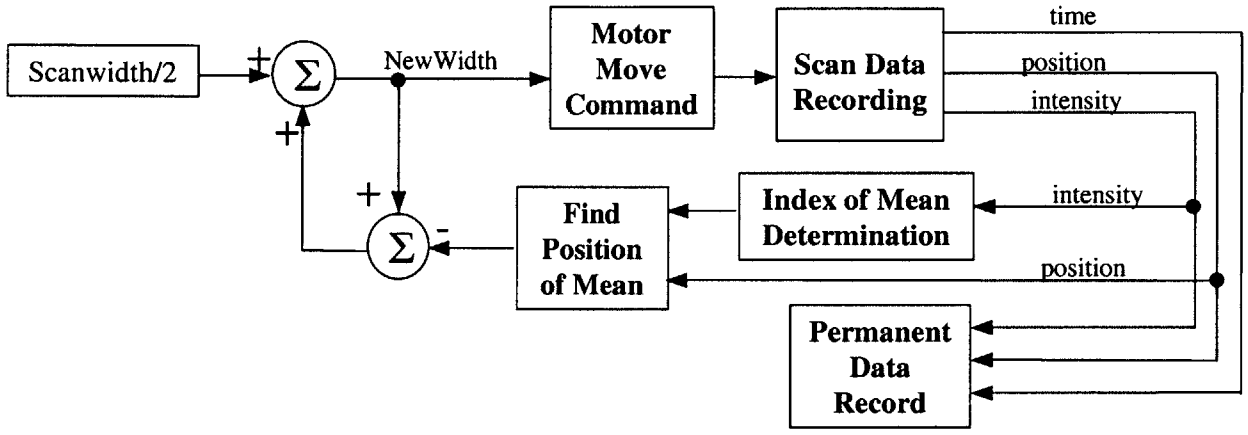

Figure B-1. Block diagram for closed loop dynamic tracking.

Tracking begins with the first Motor Move Command which uses an initialized value of NewWidth which is equal to the program constant, ScanWidth. The Zeta stepper motor has its own controller as described previously. To initiate a scan, a command is sent from the PC to the Zeta controller to move a certain distance with a prescribed speed and acceleration. The Zeta controller then takes over, sending the appropriate pulses to the stepper motor.

The next block is Scan Data Recording. This block contains a while loop which records data until the recorded position values stop changing. Monitoring the end of the scan in this way is necessary because there was no good way of receiving the same feedback from the Zeta controller. This information can, in principle, be read from the controller by reading its internal position record, however since this communication must occur over a serial connection it was found to be too slow. During the while loop, the PC recorded three arrays. One was a time array recorded from the Allios board clock. The second was position data recorded from the PCI-6601 counter board, and the third was the intensity voltage transduced by the photosensor module and recorded by the Allios board. This data was recorded at a user defined rate.

At the end of the scan, the while loop was exited. The three temporary data arrays were re-written to three larger permanent arrays which stored cumulative data from all scans. This is represented by the Permanent Data Record Block.

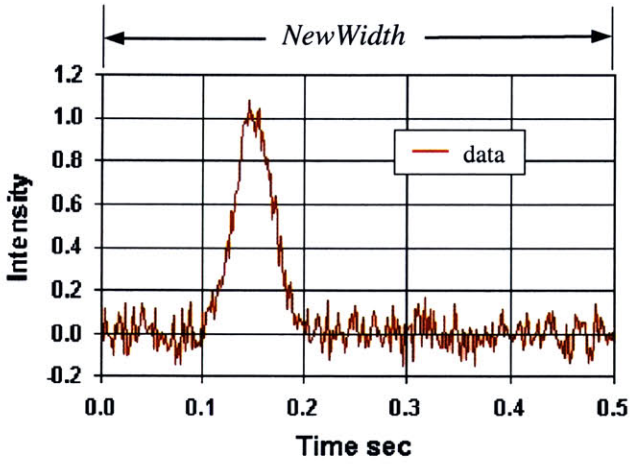

Figure B-2. Typical intensity data for single pass during dynamic tracking.

The feedback loop proceeds by feeding the temporary intensity array into the Index of Mean Determination block. An example plot of a typical intensity record is shown in Figure B-2. The x-axis is described by time in this figure but is also a function of position. The

distance over which this scan was recorded is defined by the variable NewWidth as is labeled in the figure.

The purpose of the block, Index of Mean Determination, is to determine the mean of the Gaussian peak so that this information can be used to modify the next NewWidth value. Index of Mean Determination takes an elegant approach to finding the center of the peak. A simple method would be to read the index of the maximum value in the array. However, this method would not be robust to low signal-to-noise ratios or occasional large noise spikes. The method used was first develop by Dr. Ian Hunter for this application and then modified by the author. It uses Marquardt minimization to fit a Gaussian function to the data.

The Marquardt method is a commonly used non-linear, least-squares routine to fit a model which depends non-linearly on a set of unknown parameters. Like general least squares analysis, it defines a merit function (χ^2) and determines best-fit parameters by its minimization. With nonlinear dependences, however, the minimization must proceed iteratively. With assumed initial trial values for the parameters, the Marquardt method improves the trial solution iteratively until χ^2 (effectively) stops decreasing. Additional information regarding Marquardt minimization can be found in *Numerical Recipes in C* [37] or in the Plexus source code [20].

The Marquardt method requires a model function and its first derivative be user-defined. The pre-requisite leads to quick convergence to a solution. The distribution of the fluorescing DNA molecules in their migrating band appears to be approximately Gaussian, giving rise to the bell-shaped curve seen in Figure B-2. Therefore, the fitted model was defined as a Gaussian distribution given by

$$y = \frac{A}{\sigma\sqrt{\pi}} \cdot \exp\left(-\frac{(x-\mu)^2}{2\sigma^2} \right). \qquad \text{(B-1)}$$

It contains three parameters for optimization. These include the scaling factor, A, the mean, μ, and the standard deviation, σ.

An example of the fitted results is shown in Figure B-3. This fitting was easily completed in under 100 ms if initial parameter values were within one order of magnitude of the correct value. For the very first scan, an initial value for the standard deviation was input from data based on previous experiments. After the scan was done, the temporary intensity data was digitally filtered with a finite impulse response (FIR) filter. The 25-point FIR filter had a pass frequency of 15 Hz and a stop frequency of 150 Hz and was designed using the REMEZ algorithm in Matlab. The maximum value in the filtered data was used to define an initial value for μ. This maximum value along with the initial values for μ and σ were then used to estimate A. The optimal value determined for σ via Marquardt minimization was subsequently used in the next scan as the initial value for fitting. This worked well since the σ of the DNA intensity did not vary much over time. The initial values of μ and A for the minimization were computed after each scan via the digitally filtered data and the previous optimal value of σ. Minimization was always carried out on the raw data, not the digitally filtered data.

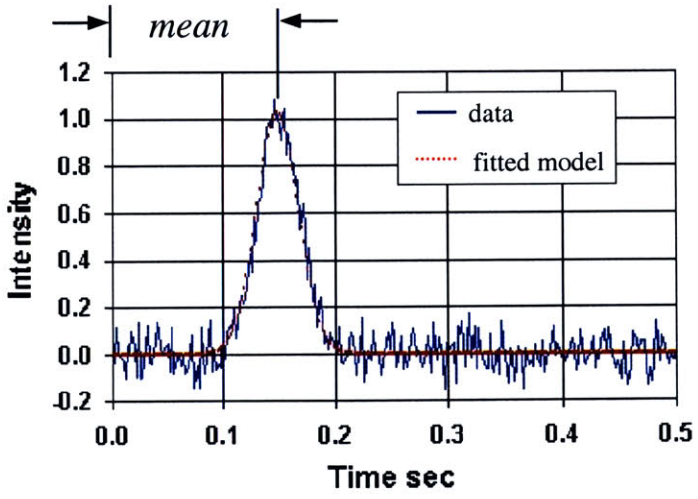

Figure B-3. Fitted Gaussian function to scan pass data to determine the mean.

In this way, the array index of the mean of the Gaussian peak was elucidated from the data. This information along with the temporary position array were fed into the next block, Find Position of Mean. Since intensity and position were recorded (nearly) simultaneously in the while loop, determining the position of the peak simply involved extracting the position value from the array corresponding to the mean intensity index. Note that the temporary position array was not an absolute position but a relative position based on the starting point of each scan.

Comparing Figure B-2 and Figure B-3, it can be seen that the quantity (NewWidth – mean) is the length of the scan to the right of the Gaussian peak. If the detector had moved in the right-hand direction relative to the peak, in the next scan it would need to move (NewWidth – mean) in the left-hand direction to get back to the center of the peak. Adding the constant value, ScanWidth/2, to this difference keeps the total scanning distance fairly constant. (If the DNA were not moving and the mean determination was exact, (NewWidth – mean) = ScanWidth/2.) The sum (ScanWidth/2 + (NewWidth – mean)), which is approximately equal to ScanWidth plus the increment the DNA has moved forward, is fed back into the motor move command, and the cycle begins again.

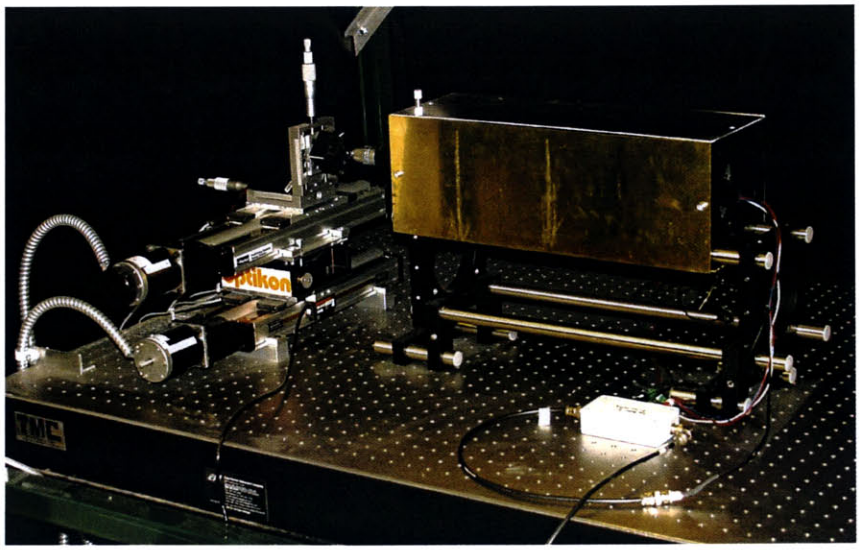

Figure B-4. Dynamic tracking testing set-up.

The tracking algorithm was tested on a set-up designed to simulate the motion of the DNA. This set-up, shown in Figure B-4, included two linear stages mounted in series. A light-emitted diode (LED) (HLMP-CM15, Hewlett Packard) was mounted behind a 500 μm pinhole on the upper stage (404140XR; Parker, Irwin, PA). The upper stage was commanded to move at constant velocity to simulate the motion of the DNA in the capillary. The motion of the Parker lower stage was controlled by the tracking software, keeping the center of short scans on the intensity peak of the measured light source. The linear encoder (RGH22 X30F00, Renishaw, 1 um resolution) on the lower stage provided the position input necessary for the tracking algorithm. No fluorescence was involved in these simulated experiments, therefore the optical system was simplified and no laser was needed. The light from the LED was collected by an infinity corrected objective (MA50, Olympus, NA = 0.7) focused by a plano-convex lens (f = 50 mm) through a pinhole. It then passed through a second plano-convex lens (f = 50 mm) and was measured by the same photosensor module used in the TGCE set-up.

Tracking results are shown in Figure B-5. These results were generated by applying the tracking algorithm in the test set-up. In this demonstration, the upper stage is commanded to move at 0.125 mm/s for a distance of 15 mm. The lower stage scans over the peak at 10 mm/sec. Data was acquired at 100 Hz. Tracking continues for several minutes after the upper stage has stopped moving. This figure was generated using Visual Basic. The color is proportional to measured intensity where darker is brighter. Notice from the figure that the scan width converges to a nearly constant value as the Marquardt minimization settles on a accurate estimation for the initial value of the standard deviation of the measured signal.

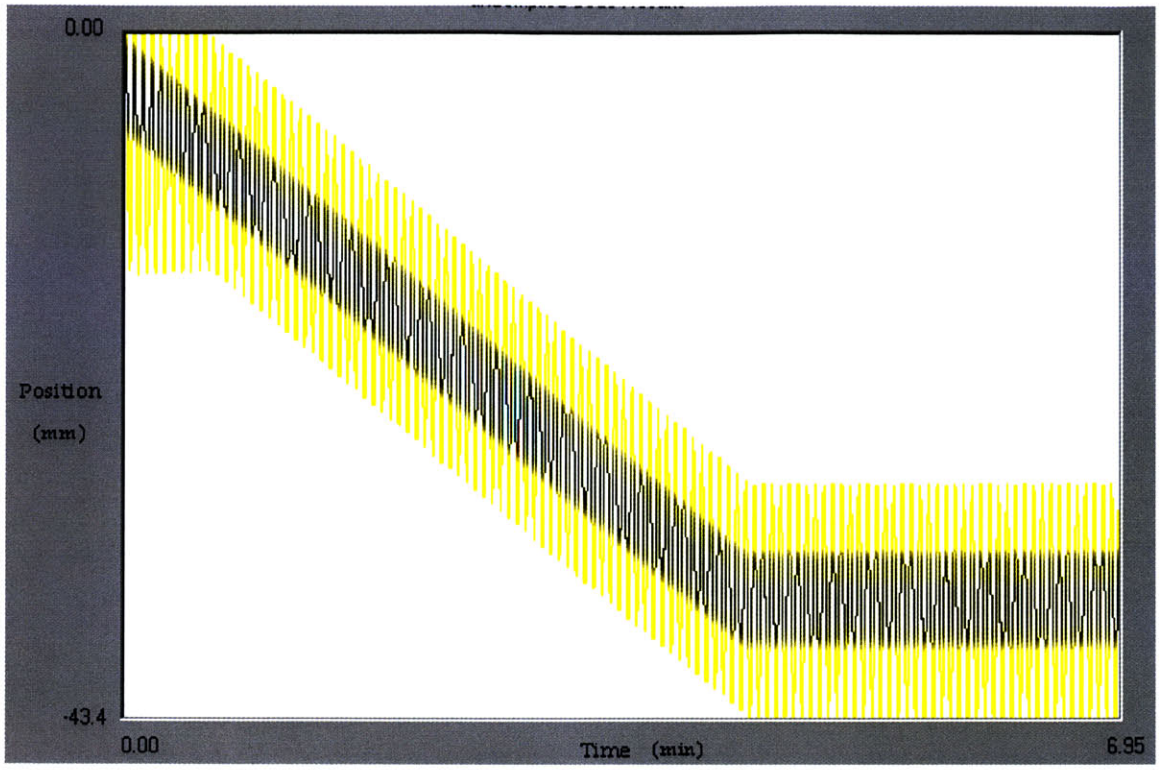

Figure B-5. Tracking data of moving LED to demonstrate tracking algorithm effectiveness.

B.4 Implementation

While this tracking software was shown to work effectively in the simulated set-up, it has not been implemented into the actual TGCE instrument. This has largely been due to time constraints.

All results presented in Chapter 7 were recorded with from scans which transverse the entire imaging region of the capillary for every scan.

Bibliography

1. Screening Methods for Detection of Unknown Point Mutations [Web Page]. Accessed 2000 Nov. www-users.med.cornell.edu/~jawagne/screening_for_mutations.html.

2. Altshuler, D., Daly, M., Kruglyak, L. Guilt by Association. Nature Genetics. 2000 Oct; 26:135-137.

3. Angel, A. DNA Detection: Thermal Gradient Development [Undergraduate Thesis]: MIT; 2000 Jun.

4. Automation Creations, Inc. Online Materials Database [Web Page]. Accessed 2000. www.matweb.com.

5. Brookes, A. J. The essence of SNPs. Gene. 1999; 234:177-186.

6. Butler, J. M., Wilson, M. R., Reeder, D. J. Rapid mitochnodrial DNA typing using restriction enzyme digestion of polymerase chain reaction amplicons followed by capillary electrophoresis separation with laser-induced fluorescence detection. Electrophoresis. 1998; 19:119-124.

7. Chen, D. Y., Swerdlow, H. P., Harke, H. R., Zhang, J. Z., Dovichi, N. J. Low-cost, high-sensitivity laser-induced fluorescence detection for DNA sequencing by capillary gel electrophoresis. Journal of Chromatography. 1991; 559:237-246.

8. Coghlan, A. Land of opportunity. Reed Business Information; 2000 Nov 4: 30-36.

9. Cohen, A. S., Najarian, D., Smith, J. A., Karger, B. L. Rapid Separation of DNA Restriction Fragments Using Capillary Electrophoresis. Journal of Chromatography. 1998; 458:323-333.

10. Cotton, R. G. H. Mutation Detection. New York: Oxford University Pres; 1997.

11. Dovichi, N. J. Laser-based microchemical analysis. Rev. Sci. Instrum. 1990 Dec; 61(12):3653-3667.

12. Goetzinger, W., Kotler, L., Carrilho, E., Ruiz-Martinez, M.C., Salas-Solano, O., and Karger, B. L. Characterization of high molecular mass linear polyacrylamide powder prepared by emulsion polymerization as a replaceable polymer matrix for DNA sequencing by capillary electrophoresis. Electrophoresis. 1998 Feb; 19(2):242-8.

13. Graham, M. R. Research Lab Book 6. MIT: 2000 May.

14. Graham, M. R. Detection of DNA Polymorphisms in Thermal Gradients via a Scanning Laser Confocal System [Master of Science Thesis]. Cambridge MA: MIT; 2000 Jun; c2000.

15. Gupta, K. Deviations from the Norm: Systems for mutation detection reveal hidden potentials. The Scientist. 1999 Jul 19; 13(25).

16. Heiger, D. N., Cohen, A. S., and Karger, B. L. Separation of DNA restriction fragments by high performance capillary electrophoresis with low and zero crosslinked polyacrylamide using continuous and pulsed electric fields. J Chromatogr. 1990 Sep 7; 516(1):33-48.

17. Hjerten, S. High-Performance Electrophoresis, Elimination of electroendosmosis and Solute Adsorption. Journal of Chromatography. 1985; 347:191-198.

18. Horikawa, Y., Oda, N., Cox, N. J., Li, X., Orho-Melander, M., Hara, M., Hinokio, Y., Lindner, T. H., Mashima, H., Schwarz, P. E., del Bosque-Plata, L., Horikawa, Y., Oda, Y., Yoshiuchi, I., Colilla, S., Polonsky, K. S., Wei, S., Concannon, P., Iwasaki, N., Schulze, J., Baier, L. J., Bogardus, C., Groop, L., Boerwinkle, E., Hanis, C. L., and Bell, G. I. Genetic variation in the gene encoding calpain-10 is associated with type 2 diabetes mellitus. Nat Genet. 2000 Oct; 26(2):163-75.

19. Horowitz, P. Hill. W. The Art of Electronics. New York, NY: Cambridge University Press;

1993.

20. Hunter, I. W. Plexus: Functions for Signal Analysis and System Identification [Visual Basic 6.0]. Cambridge MA: Bioinstrumentation Lab, MIT; 2000 Jan.

21. Johnson, I. D. Introduction to Fluorescence Techniques [Web Page]. 1999 Dec. http://www.probes.com/handbook/sections/0069.html.

22. Joseph, M. J. Taylor J. C. Mcgown L. B. Pintern J. B. Linn C. P. Spectroscopic Studies of YO and YOYO Fluorescent Dyes in a Thrombin-Binding DNA Ligand. Biospectroscopy. 1996; 2:173-183.

23. Karger, B. L., Chu, Y. H., and Foret, F. Capillary electrophoresis of proteins and nucleic acids. Annu Rev Biophys Biomol Struct. 1995; 24:579-610.

24. Khrapko, K., Coller, H., and Thilly, W. Efficiency of separation of DNA mutations by constant denaturant capillary electrophoresis is controlled by the kinetics of DNA melting equilibrium. Electrophoresis. 1996 Dec; 17(12):1867-74.

25. Khrapko, K., Hanekamp, J. S., Thilly, W. G.; Belenkii, A., Foret, F., and Karger, B. L. Constant Denaturant Capillary Electrophoresis (CDCE) - a High- Resolution Approach to Mutational Analysis. Nucleic Acids Research. 1994 Feb 11; 22(3):364-369.

26. Lerman, L. S., Senior Lecturer. 1995; Accessed 2000 Dec. web.mit.edu/biology/dna/.

27. Lerman, L. S. MIT; 2000. Personal Communication.

28. Lerman, L. S. and Frisch, H. L. Why does the electrophoretic mobility of DNA in gels vary with the length of the molecule? Biopolymers. 1982 May; 21(5):995-7.

29. Losekoot, M., Fodde R. Mutation Detection by Denaturing Gradient Gel Electrophoresis (DGGE). Human Mutation. 1994; 3:83-94.

30. Luckey, J. A., Drossman, H., Kostichka, A. J., Mead, D. A., D'Cunha, J., Norris, T. B., Smith, L.M. High Speed DNA Sequencing by Capillary Electrophoresis. Nucleic

Acids Research. 18(15):4417-4421.

31. Marino, M. A., Devaney, J. M., Davis, P. A., and Girard, J. E. Optimization of intercalation dye concentration for short tandem repeat allele genotyping using capillary electrophoresis with laser-induced fluorescence detection. J Chromatogr B Biomed Sci Appl. 1999 Sep 24; 732(2):365-74.

32. McCord, B. R., McClure, D. L., and Jung, J. M. Capillary electrophoresis of polymerase chain reaction-amplified DNA using fluorescence detection with an intercalating dye. Journal of Chromatography A. 1993; 654:75-82.

33. Molecular Probes, Inc. Product Information Sheet: YO-PRO-1. MP03602. 1999 Jun.

34. Molecular Probes, Inc. Product Handbook: 1.3 Fluorescein: The Predominant Green Fluorophore [Web Page]. 2000 Nov; Accessed 2000 Dec. http://www.probes.com/handbook/sections/0103.html.

35. Molecular Probes, Inc. Product Information Sheet: YOYO-1. MP03600. 2000 Nov.

36. Owens Corning. Commercial and Industrial Insulating Systems [Web Page]. 2000; Accessed 2000 Nov 20.

37. Press, W. H., Flanner B. P., Teukolsky, S. A., Vetterling, W. T. Numerical Recipes in C. New York, NY: Cambridge University Press; 1988.

38. Ren, J. High-Throughput Screening of Genetic Mutations/Polymorphisms by Capillary Electrophoresis. Combinatorial Chemistry and High Throughput Screening. 2000; 3:11-25.

39. Roses, A. D. Pharmacogenetics and the practice of medicine. Nature. 2000 Jun; 405:857-865.

40. Sandison, D. R., Webb W. W. Background rejection and signal-to-noise optimization in confocal and alternative fluorescence microscopes. Applied Optics. 1994; 33603-615.

41. Sandison, D. R., Williams, R. M., Wells, S. K., Strickler, J., Webb, W. W., Quantities Fluorescence Confocal Laser Scanning Microscopy (CLSM). *Handbook of Biological Confocal Microscopy* (J.B. Pawley, Ed.). 1995; 39-53.

42. Schmalzing, D., Adourian, A., Koutny, L., Ziaugra, L., Matsudaira, P., and Ehrlich, D. DNA sequencing on microfabricated electrophoretic devices. Anal Chem. 1998 Jun 1; 70(11):2303-10.

43. Schmalzing, D., Piggee, C. A., Foret, F., Carrilho, E., and Karger, B. L. Characterization and performance of a neutral hydrophilic coating for the capillary electrophoretic separation of biopolymers. J Chromatogr A. 1993 Oct 15; 652(1):149-59.

44. Sheppard, C. J. R., Gan, X., Gu, M., Roy, M. Signal-to-Noise in Confocal Microscopes. *Handbook of Biological Confocal Microscopy* (J.B. Pawley, Ed.). 363-365.

45. Sheppard, C. J. R, Gauderon, R. Effect of finite-size pinhole on noise performance in single-, two-, and three-photon confocal fluorescence microscopy. Applied Optics. 1999; 38:3562-3565.

46. Stenesh, J. Biochemistry. New York: Plenum Publishing Corporation; 1998; ISBN: 0-306-45732-6.

47. Tyagi, S., Kramer, F. R. Molecular Beacons: Probes the Fluoresce upon Hybridization. Nature Biotechnology. 1996 Mar; 14:303-308.

48. Zhu, H., Clark, S. M., Benson, S. C., Rye, H. S., Glazer, A. N., and Mathies, R. A. High-sensitivity capillary electrophoresis of double-stranded DNA fragments using monomeric and dimeric fluorescent intercalating dyes. Anal Chem. 1994 Jul 1; 66(13):1941-8.